# Electrochemical High Temperature Membrane Reactor for the Processing of Hydrogen - Carbon Monoxide Gas Mixtures

**Dissertation**
zur Erlangung des akademischen Grades

**Doktoringenieur**
**(Dr.-Ing.)**


| | |
|---|---|
| von: | Dipl.-Ing.(FH) Christian Oettel, MEng |
| geb. am: | 15. Mai 1982 |
| in: | Gera, Freistaat Thüringen |


genehmigt durch die Fakultät für Verfahrens- und Systemtechnik
der Otto-von-Guericke-Universität Magdeburg.

| | | |
|---|---|---|
| Gutachter: | Prof. Dr.-Ing. habil. Kai Sundmacher | (OvGU Magdeburg) |
| | Prof. Dr.-Ing. habil. Karel Bouzek | (VŠCHT Praha) |
| | Prof. Dr.-Ing. habil. Ulrich Kunz | (TU Clausthal) |


eingereicht am: 05. Februar 2013
Promotionskolloquium am: 27. August 2013

# Danksagung

”Es ist ein lobenswerter Brauch,
Wer was Gutes bekommt,
Der bedankt sich auch.”

*Wilhelm Busch*

An dieser Stelle möchte ich meinen Dank an all diejenigen Menschen zu richten, die mich auf dem Weg zur Promotion unterstützt, motiviert, geleitet, herausgefordert, angeschoben und begleitet haben. Nur das vollständige Puzzle, bestehend aus den kleinen und größeren Taten Vieler, hat es mir ermöglicht den Weg zur Promotion vom Anfang bis zum Ende zu gehen.

Als Mitglied der Arbeitsgruppe von Prof. Kai Sundmacher am Max-Planck-Institut für Dynamik komplexer technischer Systeme in den Jahren 2007-2012 kam ich in den nicht selbstverständlichen Genuss eines spannenden Tätigkeitsfeldes mit viel fachlicher Bewegungsfreiheit, gepaart mit wissenschaftlicher Begleitung und einer nicht zu unterschätzenden Planungssicherheit. Für die Schaffung dieser Rahmenbedingungen und den stets fairen und verständnisvollen Umgang bedanke ich mich ganz herzlich bei Prof. Kai Sundmacher.

Als ”Türöffner” zum MPI-Magdeburg, sowie als freundschaftlicher Kollege in allen Lagen, hat mich Richard Hanke-Rauschenbach während meiner gesamten ”Magdeburger Zeit” mit Rat und Tat begleitet. Für seine stets ehrliche Meinung, für den geführten fachlich wie freundschaftlichen Austausch, sowie für seine Hilfsbereitschaft bin ich Ihm sehr dankbar.

Ein weiterer wichtiger Ansprechpartner, fachlich wie menschlicher Natur, war für mich Liisa Rihko-Struckmann. Ihre pragmatische Sicht auf das wissenschaftliche Arbeiten möchte ich zurückblickend in vieler Hinsicht als ”heilsam” bezeichnen. Mit Ihrer Hilfe war es mir möglich den Fokus auf das Wesentliche zu richten, um so die Ergebnisse meiner Arbeit besser ordnen und bewerten zu können. Hab vielen Dank dafür Liisa!

Der Einfluss von Peter Heidebrecht auf meine Arbeit ist schwer zu fassen, doch waren und sind die geführten Gespräche sehr wertvoll für mich. Egal wie voll seine ”To-Do Liste” auch war, er fand immer Zeit für eine Einheit ”White-Board-Einzelunterricht”, und war höchst ausdauernd beim Problem-knobeln bis zum ”bitteren” Ende. Trotz seiner fachlichen Brillianz war bei Ihm vom ”akademischen Elfenbeinturm” nichts zu spüren. Ich habe Ihn, fachlich wie privat, als Menschen mit hohen moralischen Werten sehr zu schätzen gelernt.

Bianka Stein wird es mir hoffentlich verzeihen wenn ich Sie hier mit viel Sympathie als ”Mutter” unserer Arbeitsgruppe beschreibe. Mit viel persönlichem Engagement, fachlichem Wissen und Interesse hatte Sie stets ein offenes Ohr für der Doktoranden kleinen und größeren Probleme. Bei meiner Arbeit im Labor war sie mir oft der ”Retter in der Not”. Egal welches Hilfsmittel ich dachte zu brauchen, Sie fand immer Etwas das mich weiter brachte.

Für die tatkräftige Unterstützung beim ingenieurtechnischen Aufbau und Anpassung meines Versuchsstandes möchte ich mich ganz herzlich bei Torsten Schröder bedanken. Ein weiteres großes ”Danke Schön!” gebührt Markus Ikert und den Mitarbeitern der mechanischen und elektrischen Werkstatt am MPI Magdeburg, welche mit viel Motivation, Interesse und Einsatz so mancher experimentellen Idee zu Verwirklichung verholfen haben.

Des weiteren möchte ich ”meinen” Studenten Sebastian Schulz, Quang Tran, Daniel Schröder und Tobias Weber für die angenehme und erfolgreiche Zusammenarbeit im Rahmen ihrer Diplom-& Studienarbeitsprojekte danken. Namentlich erwähnen möchte ich ebenfalls meine Weggefährten Thomas Kadyk, Christoph Hertel, Maik Kraus, Matthias Pfafferodt und Sebastian Kirsch. Nicht selten haben wir über fachlichen Fragen gebrütet bis eine Lösung gefunden war und gemeinsam so einige erholsame Stunden verbracht.

Am Schluss möchte ich noch meinen Wegbereitern danken. Fachlich hat mir Prof. Karel Bouzek den Weg in die Wissenschaft geöffnet, indem er mir ermöglichte meine ersten elektrochemischen Gehversuche in seiner Forschungsgruppe am ICT Prag zu unternehmen. Deswegen freut es mich sehr, dass er als ein Gutachter dieser Dissertation ebenfalls an meiner Promotion beteiligt war. Děkuju vam mnohokrát!
Ohne solides Fundament lassen sich keine Häuser bauen! Mein Fundament auf dem Weg zur Promotion war meine Familie. Meine Eltern Bärbel und Helmut Oettel haben mir viel Nützliches für diesen Weg mitgegeben und mich stets unterstützt. Sie haben mir die nötige Bildung ermöglicht, zur rechten Zeit den nötigen ”Stups” gegeben und mir den Blick geschärft für Dinge außerhalb des ”Tellerrandes”. Für all das bin ich ihnen sehr dankbar!
Eine der schwierigsten Aufgaben während meiner Promotion hatte meine liebe Frau Linda zu tragen. Sie hielt mir stehts den Rücken frei, hielt meinen Launen bei fachlichen Rückschlägen stand, und schenkte mir während der Promotionszeit zwei wundervolle Töchter, die mir sowohl Konzentrations- als auch Entspannungshilfe waren. Für das hierfür notwendige Vertrauen in mich und mein ”Projekt” und für ihre Geduld bin Ihr zutiefst dankbar.

# Table of Contents

# List of Symbols

Symbols which are only of local interest are declared at the place of use and are not listed here.

## Latin Symbols

| | | |
|---|---|---|
| $E_{i=0}$ | open circuit potential | (V) |
| $E$ | molar exergy | $(\mathrm{J \cdot mol^{-1}})$ |
| $F$ | Faraday constant | $(\mathrm{A \cdot s \cdot mol^{-1}})$ |
| $G$ | molar flow rate | $(\mathrm{mol \cdot s^{-1}})$ |
| $I$ | exergy irreversibility loss | $(\mathrm{J \cdot mol^{-1}})$ |
| $U_{cell}$ | fuel cell voltage | (V) |
| $P_{el}$ | electrical power density | $(\mathrm{W \cdot cm^{-2}})$ |
| $R$ | universal gas constant | $(\mathrm{J \cdot K^{-1} \cdot mol^{-1}})$ |
| $R_{cell}$ | ohmic cell resistance | $(\Omega)$ |
| $RI$ | recovery index | (/) |
| $T$ | temperature | (K) |
| $T_{dew}$ | dew point temperature | (K) |
| $U$ | EWGSR cell voltage | (V) |
| $U_{cell,H_2}$ | fuel cell voltage, hydrogen operation | (V) |
| $U_{cell,H_2/CO}$ | fuel cell voltage, $H_2$/CO operation | (V) |
| $\Delta U_{cell,CO}$ | fuel cell voltage loss due to CO | (V) |
| $Z_{feed}$ | feed gas utilisation degree | (/) |
| | | |
| $\tilde{c}_p$ | molar heat capacity under const. pressure | $(\mathrm{J \cdot mol^{-1} \cdot K^{-1}})$ |
| $h$ | enthalpy | (J) |
| $i$ | current density | $(\mathrm{A \cdot cm^{-2}})$ |
| $k_{CO}^{ox}$ | CO oxidation reaction constant | $(\mathrm{mol \cdot s^{-1}})$ |
| $p_{H_2O}$ | partial pressure of water | (Pa) |
| $p_{gas}$ | gas pressure | (Pa) |
| $q$ | molar heat | $(\mathrm{J \cdot mol^{-1}})$ |
| $q_{rev}$ | reversible heat transfer | (J) |
| $r_{CO}^{ox}$ | CO oxidation reaction rate | $(\mathrm{mol \cdot s^{-1}})$ |
| $s$ | molar entropy | $(\mathrm{J \cdot K^{-1} \cdot mol^{-1}})$ |
| $\tilde{v}$ | molar volume | $(\mathrm{m^{-3} \cdot mol^{-1}})$ |
| $w_{rev}$ | reversible work | (J) |
| $x$ | molar fraction | (/) |
| $z$ | transferred electrons | (/) |

## Greek Symbols

| | | |
|---|---|---|
| $\beta_{CO}$ | CO current fraction | (/) |
| $\Phi_{H_2}$ | specific energy consumption | $(\mathrm{J} \cdot \mathrm{mol}^{-1})$ |
| $\eta_A$ | anode overpotential | (V) |
| $\eta_{A,H_2}$ | anode overpotential, $H_2$ operation | (V) |
| $\eta_{A,H_2/CO}$ | anode overpotential, $H_2$/CO operation | (V) |
| $\eta_C$ | cathode overpotential | (V) |
| $\eta_{carnot}$ | carnot efficiency | (/) |
| $\epsilon$ | exergy | (J) |
| $\Theta_{CO}$ | CO surface coverage | (/) |
| $\chi$ | product to feed gas ratio | (/) |

## List of Superscripts

| | |
|---|---|
| 1 | process heat surplus |
| 2 | process heat demand |
| *CWGSR* | cyclic water gas shift reactor |
| *PSA* | pressure swing adsorption |
| *exp* | experimental |
| *max* | theoretic maximum |
| $^\circ$ | reference state |
| $\tilde{}$ | indicator of molar unit |

## List of Subscripts

| | |
|---|---|
| *cath* | cathodic |
| *chem* | chemical fraction |
| *comp* | compression |
| *dry* | dry stream, without water |
| *ed.* | educt |
| *i* | species i |
| *in* | inlet gas stream |
| *max* | stoichiometric maximum |
| *mix* | mixture indicator |
| *out* | outlet gas stream |
| *ox* | oxidation |
| *phys* | physical fraction |

## List of Subscripts (continuation)

| | |
|---|---|
| *prod* | product |
| *q* | heat transfer |
| *R* | reaction indicator |
| *tot* | total |
| *w* | work |
| *wgsr* | water gas shift reactor |
| | |
| $^\circ$ | initial state |

## Abbreviations and Acronyms

| | |
|---|---|
| ABPBI | poly(2,5-benzimidazole) |
| CWGSR | cyclic water gas shift reactor |
| ECDL | electrochemical double layer |
| ECHP | electrochemical $H_2$ pump |
| ECHPR | electrochemical $H_2$ pump reaction |
| ECPrOx | electrochemical preferential oxidation reactor |
| el.chem. | electrochemical |
| EMR | electrochemical membrane reactor |
| EWGSR | electrochemical water gas shift reactor |
| GC | gas chromatograph |
| GDE | gas diffusion electrode |
| GDL | gas diffusion layer |
| HT | high temperature |
| HT-PEMFC | high temperature polymer electrolyte membrane fuel cell |
| LT | low temperature |
| MEA | membrane electrode assembly |
| MemSep | membrane separation |
| NIST | National Institute of Standards and Technology |
| OCV | open circuit voltage |
| PBI | poly[2,2'-(*m*-phenylene)-5,5'-bibenzimidazole] |
| PEM | polymer electrolyte membrane |
| PEMFC | polymer electrolyte membrane fuel cell |
| PrOx | preferential oxidation |
| PSA | pressure swing adsorption |
| PTFE | polytetrafluoroethylene |

## Abbreviations and Acronyms (continuation)

| | |
|---|---|
| RI | recovery index |
| RH | relative humidity |
| WGSR | water gas shift reaction |

# Kurzfassung

Trotz großer wissenschaftlicher Anstrengungen auf dem Gebiet der Kohlenstoff freien Wasserstofferzeugung werden Kohlenwasserstoffe auch mittelfristig ein wichtiger Rohstoff für die industrielle Wasserstofferzeugung bleiben. Um den energetischen und umwelttechnischen Herausforderungen des 21. Jahrhunderts erfolgreich zu begegnen, ist es notwendig die Prozesskette der Kohlenwasserstoff basierten $H_2$-Herstellung so effektiv wie möglich zu gestalten.
Wasserstoff reiches Gas, hergestellt durch Reformierung oder Biomassevergasung, enthält eine signifikante Menge an CO. Es findet Verwendung in chemischen Syntheseprozessen und in der Energieerzeugung. In aller Regel wird dieses Reformatgas in mehreren Reinigungs- und Separationsschritten aufbereitet, bevor es in dem jeweiligen finalen Prozess eingesetzt wird. Jede technisch sinnvolle Vereinfachung dieser Gasaufbereitung erhöht die Effizienz, reduziert die Komplexität und verringert die Zahl der benötigten Prozesseinheiten der gesamten Prozesskette.

In der hier vorgestellten Arbeit werden zwei Ansätze verfolgt um die oben erwähnte Kohlenwasserstoff basierte $H_2$-Prozesskette zu verbessern. Zum einen wurde ein finaler $H_2$ konsumierender Prozess adressiert, indem die CO-Verträglichkeit eines autonom arbeitenden Reaktors zur Erzeugung von elektrischem Strom erhöht wurde. Zum anderen wurde ein neues Reaktorkonzept, welches die Wassergas-Shift-Reaktion und die Wasserstoffseparation in einem Prozessschritt vereint, für die Aufbereitung von Reformatgas entwickelt und charakterisiert. Beide Ansätze wurden mit Hilfe eines elektrochemischen Membranreaktors realisiert, welcher in einem Temperaturbereich zwischen 383 K und 473 K betrieben werden kann.
Während des autonomen Betriebs als Energieerzeuger wurde der Reaktor als Hochtemperatur - Polymerelektrolytmembran - Brennstoffzelle (HT-PEMFC) betrieben. Hierbei wurde in der HT-PEMFC eine Platin-Ruthenium Legierung als Anodenkatalysator eingesetzt, anstelle des gewöhnlich verwendeten reinen Platins. Die CO-Verträglichkeitserhöhung der HT-PEMFC als Folge des veränderten Anodenkatalysators wurde untersucht. Die Experimente wurden im Temperaturbereich zwischen 403 K und 443 K mit CO Konzentrationen von 0 bis 6.5% im $H_2$ Eduktgas durchgeführt. Die eingesetzte Anodenkatalysatorlegierung reduzierte deutlich den negativen Einfluss von CO auf die Zellspannung, wobei die bekannte temper-

aturabhängige Verringerung des CO-Einflusses in HT-PEMFCs übertroffen wurde. Es wurde gezeigt, das der Spannungsverlust auf Grund von CO in HT-PEMFCs mit PtRu als Anodenkatalysator kleiner ausfiel als bei gleichartig angefertigten HT-PEMFCs mit Pt als Anodenkatalysator. Weiterhin führte die PtRu Anode, im Vergleich zur konventionellen Pt Anode, zu einem geringeren Spannungsüberschwingen nach einer Lasterhöhung.

Das neuartige Reaktorkonzept, welches elektrische Energie für die Reformataufbereitung benötigt, kann, bezugnehmend auf die ablaufende Reaktion, als elektrochemischer Wassergas-Shift-Reaktor (EWGSR) bezeichnet werden. Im EWGSR wird die Wassergas-Shift-Reaktion und die Abtrennung von Wasserstoff auf elektrochemischen Weg mit Hilfe von elektrischer Energie in einem Prozessschritt vereint. Der EWGSR verwendet die gleiche Membran - Elektroden - Anordnung wie die HT-PEMFC. Der Reaktor wurde bei 403 K und 423 K mit befeuchtetem CO und $N_2$, und bei 393 K und 403 K mit befeuchteten Gasgemischen aus $H_2$, CO und $N_2$ betrieben. Die experimentellen Ergebnisse zeigen, dass die $H_2$-Erzeugung an der Kathode nach dem Faradayschen Gesetz abläuft und bewiesen die Anwendbarkeit des EWGSR - Konzeptes. Anodisches PtRu führte zu einem geringeren elektrischen Leistungsbedarf als Pt. Der $H_2$ freie Betrieb bei tieferen Temperaturen führte zu einer Verringerung des elektrischen Leistungsbedarfs, während die Menge an kathodenseitig generiertem $H_2$ nicht beeinflusst wurde. Die experimentellen Ergebnisse zeigen den Einfluss von verschiedenen Betriebsparametern auf die EWGSR Charakteristika, wie Zellspannung, elektrochemische CO Oxidation, oder den elektrischen Energieverbrauch des Reaktors.

Mit Hilfe einer Exergieanalyse wurde die Anwendbarkeit des EWGSRs bewertet und das Konzept mit Alternativprozessen verglichen. Die gesammelten Ergebnisse weisen darauf hin, dass die Betriebsbedingungen des EWGSRs sorgfältig gewählt werden müssen, um seinen Wirkungsgrad über den der ausgewählten, den Stand der Technik repräsentierenden, Prozessrouten zu heben. Zusätzlich zeigte die Exergieanalyse vielversprechende Verbesserungspotentiale des EWGSRs auf und identifizierte Ansätze für eine Optimierung des Reaktorbetriebs, um hohe Wirkungsgrade zu erzielen.

# Abstract

Despite the enormous research efforts concerning the generation of hydrogen outside the carbon cycle, hydrocarbons will remain to be most likely a major feedstock for hydrogen generation processes in our midterm future. In order tackle the energetic and environmental challenges of the $21^{st}$ century, the improvement potential within this process chain, from the generation to the utilisation of this hydrocarbon based hydrogen, needs to be utilised effectively.
Hydrogen rich gas, originating from reforming processes or biomass gasification contains a significant amount of CO and is used within chemical synthesis processes and electrical energy generation processes. Generally, this reformat gas undergoes several purification and cleaning steps before it is used within the aimed for final processes. Every technical feasible simplification of this gas processing increases the efficiency, decreases the complexity and lowers the process unit count of the whole process chain.

Two basic principles were followed within the here presented thesis to improve the above mentioned hydrocarbon based process chain. On the one hand, the final hydrogen rich gas utilisation step was addressed by improving the CO tolerance of an autonomous operating electrical power generating reactor. On the other hand, a novel reformat gas processing reactor concept, combining the water gas shift reaction & hydrogen separation step into one process unit, was developed and characterised. Both approaches were realised with one electrochemical membrane reactor, able to operate in a temperature range between 383 K and 473 K .
While operating autonomously as electrical power generating unit, the reactor functioned as a high temperature polymer electrolyte membrane fuel cell (HT-PEMFC). Here, the HT-PEMFC was equipped with a carbon supported platinum-ruthenium alloy as anode catalyst, instead of the generally used pure platinum on carbon catalysts. The CO tolerance improvement of the HT-PEMFC due to different anode catalysts was investigated. The experiments were carried out at temperatures between 403 K and 443 K with a CO concentration in the $H_2$ feed gas between 0 and 6.5 vol%. The alloy anode catalyst lowered significantly the negative influence of CO upon the cell voltage, exceeding the known temperature dependent CO influence reduction in HT-PEMFCs. It was found that the CO induced voltage loss

of the HT-PEMFC with PtRu anode catalyst was lower than similarly prepared HT-PEMFCs equipped with Pt anode. Furthermore, the PtRu bimetallic anode electrode was found to lower the voltage overshoot after a load increase, if compared to conventional Pt anode.

The novel reformat gas processing reactor was operated in driven mode and was called, according to the occurring reaction, electrochemical water gas shift reactor (EWGSR). Within the EWGSR, the water gas shift reaction and the separation of hydrogen is realised electrochemically in one process step by using electrical energy. The EWGSR utilises the similar membrane electrode assembly as was used for the HT-PEMFC operation. The reactor was operated at 403 K and 423 K with humidified CO and $N_2$ and at 393 K and 403 K with humidified $H_2$,CO and $N_2$ gas mixtures. The experimental results show that $H_2$ was generated at the cathode according to Faraday's Law and proved the concept's feasibility. Anodic PtRu led to lower electrical power demands than Pt. The $H_2$ free operation at a lower temperature resulted in a lower electrical power demand, while an equal amount of cathodic $H_2$ was generated. The experimental results show the influence of several operation parameters upon the EWGSR characteristics, like the cell voltage, the electrochemical CO oxidation, or the electrical energy demand of the reactor.

The feasibility of the EWGSR was assessed and compared to alternative processes using exergy efficiency analysis. The collected results indicate that the operation conditions of the EWGSR need to be carefully selected to realise higher efficiencies than the selected state - of - the - art process routes. The exergy analysis revealed, additionally, a promising improvement potential of the EWGSR and pointed to optimisation pathways of its operation to reach the strived for high efficiencies.

# Chapter 1

# Introduction

In the $21^{st}$ century, humanity awaits major challenges concerning the preservation and improvement of living conditions. Keywords like climate change, peak oil, water shortage and Fukoshima/Tschernobyl stand for some of the major tasks of humankind, and illustrate the necessity of determined research and development in every field of science and technology.
The presence of the global warming was generally accepted in the 1970s [1–3]. However, not until 2010 a first international consents to limit the global temperature increase to 2 K (with respect to the pre-industrial level) was negotiated at the UN climate conference in Cancum [4]. In order to succeed, significant reductions of the green house gas $CO_2$ emissions in the industrial and energy sectors world wide are necessary. Furthermore, the main precursors of $CO_2$ and simultaneously major feed-stocks of current energetic and industrial processes, the fossil resources, are limited [5], which dictates a highly efficient and sustainable consumption of these substances.

In the course of these enormous challenges and the Fukoshima catastrophe, the federal government of Germany defined in the summer of 2011 a strategy roadmap for the transition of the energy generation sector from carbon and nuclear based power generation to power generation from renewable sources [6]. However, the realisation of this ambitious goal requires an energy carrier and energy storage alternative to fossil fuels, which can be generated from renewable sources.
Hydrogen is up to date the most promising candidate to enable this energy transition, as it can be generated from renewable sources [7–9], as well as from fossil fuels [10–12]. The possibility of hydrogen generation from fossil fuels is, with respect to the required flexible transition to the carbon neutral energy economy, highly important. It enables the temporary compensation of missing sustainable hydrogen generation facilities and, thus, supports the marked introduction of hydrogen based energy systems, independent from the respective hydrogen generation technology. The European Hydrogen Roadmap follows this flexible transition approach, as it

defines time related milestones for a stepwise reduction of fossil fuels within the hydrogen generation until 2050 [13].

Within the framework of the upcoming industrial and energetic transition process, the here presented project aims to contribute to the development of highly efficient technologies for the utilisation and generation of hydrogen from carbohydrates. Such technologies reduce the environmental footprint of the current fossil fuel based hydrogen generation processes and enable the utilisation of carbon neutral hydrogen from biomass in the future.
The project examined a dual electrochemical reactor concept which allows for either (i) the electrical power generation from highly carbon monoxide contaminated hydrogen gas, or for (ii) the generation of pure hydrogen from hydrogen and carbon monoxide containing gas mixtures within one process step. The goal was (i) to demonstrate the reactor concept feasibility, (ii) to characterise the processes dominating the reactor operation behaviour, and (iii) to identify possibilities to enhance the operation efficiency. This was realised (i) by the development of a feasible reactor design, (ii) by alternating design- and operation parameter of the reactor within various experiments, and (iii) by the application of an exergy based analysis using experimentally obtained data and literature resources.

The following chapters introduce briefly the fundamentals and related processes of this project, the reactors concept and its operation characteristics during both operation modes. Furthermore, the reactor operation is experimentally evaluated and compared to alternative processes.

> "The fact remains that, if the supply of energy failed, modern civilization would come to an end as abruptly as does the music of an organ deprived of wind. [But] ... the still unrecognized 'energy problem' ... awaits the future."
> *Frederick Soddy - Matter and Energy (**1912**), p 251.*

# Chapter 2

# Hydrogen and Electrochemical Membrane Reactors

Within the ongoing debate about the future of sustainable energy generation (Solar, Wind, Biomass etc.), large scale storage of energy constitutes a major issue which needs to be solved. In this context, $H_2$ is the most prominent substance to enable the renunciation from the $CO_2$ generating energy conversion process chains. Furthermore, $H_2$ is an important feedstock for the chemical industries. It is required among others in high purity for hydrogenation reactions or for the ammonia synthesis [14, 15]. On the other hand, as part of synthesis gas ($H_2$ + CO) $H_2$ is required for the production of organic compounds like methanol, methane or long-chain hydrocarbons via the Fischer-Tropsch process [16–19].

The generation of $H_2$ and its conversion into electrical energy requires highly efficient processes to allow for a feasible chain of technical and economical value within the prospect of a future $H_2$ economy. New reactor concepts, which integrate two or more process steps into one process, are sought after with the goal to increase the efficiency of processes and possibly to reduce the capital investment costs. In comparison to common tubular or batch reactors with fixed of fluidised beds, electrochemical membrane reactors provide different reaction conditions and properties, which might have the potential to enhance the efficiency of the $H_2$ generation and utilisation process chain.

In the following chapters, state of the art $H_2$ generation processes are briefly introduced (chapter 2.1), followed by an overview about the basic properties of electrochemical membrane reactors (chapter 2.2). Furthermore, a brief overview about the application concepts of electrochemical membrane reactors for the processing and utilisation of $H_2$ + CO gas mixtures is presented (chapter 2.3).

## 2.1 State of the Art $H_2$ Generation

Many different pathways are available today to obtain molecular $H_2$ [7]. All $H_2$ generation methods can be classified based upon the utilised $H_2$ source into two groups. Conventional technologies are based on reforming processes which convert hydrocarbons (methane, biomass, oil, coal, etc.) into gas mixtures of $H_2$, CO, $CO_2$, and others [10, 20, 21]. Subsequent to the reforming process, $H_2$ is extracted and purified from these reformat gas mixtures by means of several downstream process units.

On the other hand, $H_2$ can be generated by splitting $H_2O$, without generating CO or $CO_2$ as side products. The electrolysis is technically well developed and utilises electrical energy to split $H_2O$ in an electrochemical reaction [22]. Here, systems with different electrolytes are available, employing alkaline electrolytes [23], polymer membrane electrolytes [24], or solid oxide electrolytes [25]. Depending upon the type of electrolyte, different catalysts and operation temperatures are required, which make the systems suitable for different applications.

Technically feasible alternatives to $H_2O$ splitting via electrolysis are thermochemical cycles, which enable the splitting of $H_2O$ by utilising cyclic reaction pathways driven by heat energy [26–28]. Here, solar heat sources as well as nuclear heat sources are under investigation.

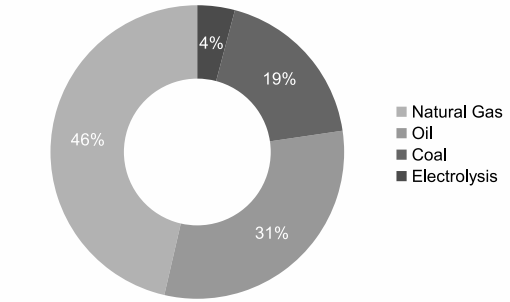


**Figure 2.1.:** Main $H_2$ sources with respect to their share of the worlds $H_2$ production [29].

As shown in figure 2.1, the major $H_2$ fraction produced world wide originates from carbohydrate reforming processes. The steam reforming of natural gas contributes the largest share of about 46% to the world's hydrogen production. On the other hand, the electrolysis of $H_2O$ provides only about 4% of the annual generated $H_2$. The main reactions of the hydrocarbon steam reforming are presented in the equations 2.1-2.3 [10]. Here, equation 2.1 represents the steam reforming reaction of

methane, which is highly endothermic and is carried out at temperatures of about 970-1100 K [29]. The reforming reaction of long-chain hydrocarbons is also highly endothermic (equation 2.2), whereas the conversion of CO to $CO_2$ (water gas shift reaction), shown in equation 2.3, is slightly exothermic.

$$CH_4 + H_2O \longrightarrow CO + 3\,H_2 \qquad \Delta_R H \gg 0 \tag{2.1}$$

$$C_nH_m + n\,H_2O \longrightarrow n\,CO + {}^{(m+2n)}/_2\,H_2 \qquad \Delta_R H \gg 0 \tag{2.2}$$

$$CO + H_2O \longrightarrow CO_2 + H_2 \qquad \Delta_R H < 0 \tag{2.3}$$

Carbon monoxide is only partially converted into $CO_2$ within a steam reforming reactor (equation 2.3), as, according to the thermodynamics of the reaction (principle of Le Chatelier), its high operation temperatures only allow for a partial turnover within this exothermic reaction. The product gas of methane steam reforming contains about 10-13 mol% CO [15].
Consequently, several downstream process units (e.g. water gas shift reactors, PrOx reactors, membrane separators, etc.) are required after the reforming reactor to generate pure $H_2$ from the reformat gas [30]. The water gas shift reaction (equation 2.3) is usually conducted subsequently at two temperature levels, the high temperature (HT) shift reaction and low temperature (LT) shift reaction. The HT shift reaction is typically conducted within the temperature range of 623-773 K and the exit gas contains about 3-4% CO. Subsequently, the gas is cooled down and fed to the LT shift reactor, which operates at about 473 K and enables effluent CO concentrations of about 0.2-0.5 % [31]. More information about the characteristics of the water gas shift reaction, the applied catalysts and reactor setup can be found within the available literature, e.g. [32–36].

In order to achieve a high purity level, $H_2$ is separated from the remaining gas components (e.g. $CO_2$, CO, etc.) after the water gas shift units. Here, pressure swing adsorption (PSA) and membrane separation (MemSep) are the most prominent separation methods [15, 37].
The PSA is currently the state of the art process to separate large quantities of $H_2$ from process gas [14]. The separation method is based on the adsorption behaviour deviations of species on specific substrates. Substances with a high volatility and low polarity (e.g. $H_2$) exhibit, in dependence upon the applied adsorbent, a lower adsorption tendency than polar molecules (e.g. hydrocarbons, CO, $CO_2$, $H_2O$) [38]. The adsorption step is carried out at pressures of several bars, to support the species adsorption. The process is conducted within several columns (minimal 4 columns) which are filled with the respective adsorbent. These columns are operated in an alternating manner, where the single operation steps are (i) ad-

sorption, (ii) pressure release, (iii) regeneration and (iv) pressurisation. Pure $H_2$ is gained during the adsorption step as it flows through the separation unit without adsorbent interaction. The whole process is operated auto-thermally, since the exothermic adsorption balances the endothermic desorption [14, 38, 39].
A further well established separation method for gas mixtures is the MemSep [14, 40]. Here, a gas mixture is fed under high pressure into a gas compartment, which is separated from a low pressure compartment by a membrane. This membrane possesses a permselectivity for one of the gas components (e.g. $H_2$). Consequently, the respective gas component, driven by the pressure difference, penetrates the membrane to the low pressure side of the separation unit. Possible transport mechanism through the membranes are Knudsen diffusion, molecular sieving, solution-diffusion, and surface diffusion. Four types of membrane materials are employed within $H_2$ separation units, being metallic, polymer, carbon, and ceramic based materials [40–42]. Metallic thin film Pd based membranes are mostly employed for $H_2$ MemSep. Here, $H_2$ is transported via the solution-diffusion mechanism (atomic H diffusion) through the membrane.

Independent from the $H_2$ purification pathway, all introduced options based on hydrocarbons require several downstream process units after the reforming step. This is accompanied by significant complexity of the $H_2$ plant. This influences not only the process efficiency, but also the investment and maintenance costs of the process.
Consequently, new reactor concepts are required to decrease the system's complexity and increase the system's flexibility, while at best improving the product quality.

## 2.2 Electrochemical Membrane Reactors

Electrochemical membrane reactors (EMR) possess an ion conducting membrane, which is usually conductive for only one ionic specie. This electrolyte membrane is most of the times impermeable for non-charged species and separates the reactor into two compartments. Electrodes, attached to both sides of the membrane enable locally separated oxidation and reduction reactions. These electrodes are, in most of the cases, connected to an external electrical circuit, which enables an electron transfer from the reactor anode to the reactor cathode. Consequently, EMRs are electrochemical cells with immobilised electrolytes. The two compartment setup of the EMR results in non-mixed educt feed streams, as anode and cathode are supplied with educts separately. The principle setup of a EMR is shown in figure 2.2, where AB and $C_2$ represent educt species. The exchangeable charged specie $A^{n*}$

is displayed with a universal charge, where "n" accounts for charge number and "*" is a wildcard symbol for the either positive or negative charge. The electrical circuit is the pathway for the electron transfer between the electrodes, whereas the transfer direction depends upon the charge nature of $A^{n*}$.

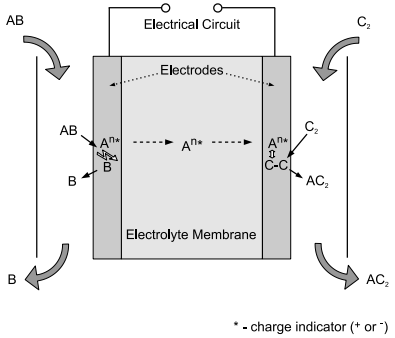


**Figure 2.2.:** Principle setup of an electrochemical membrane reactor.

The operation of EMRs is always connected with an electron flow between the anode and cathode electrodes and a characteristic polarisation curve (i.e. current-voltage dependence). Electrons are generated and consumed by the desired electrochemical reactions at the respective electrodes. The driving force of the desired electrochemical reactions within EMRs are electrochemical potential differences between the anode and cathode electrode. These can occur autonomously if the system is not in electrochemical equilibrium. This appears if the surface species/electrolyte potential difference (electrochemical double layer potential) at both electrodes differ from each other. This difference can either be caused by the redox potential of the anodic and cathodic species (i.e. galvanic cell) or by different surface concentrations of the same specie at the anode and cathode (i.e. concentration cell).
In the case that the desired electrochemical reaction exhibits a negative free Gibbs enthalpy and the resulting potential difference between the electrodes is not high enough to overcome its activation losses, an external power source can be used to polarise the electrodes beyond the equilibrium between the electrodes. This drives the respective reactions by "pumping" the participating species from the anode to the cathode. Reactions which exhibit a positive Gibbs free energy (e.g. $H_2O$ splitting), i.e. reactions which are driven contrary to the spontaneous reaction direction of the involved species, are named electrolysis reactions and require the imposition of the required electrode potential difference with the help of an external electrical power source. Generally, the autonomous EMR operation generates electrical power (e.g. fuel cell), whereas the driven EMR operation consumes electrical power.

The current voltage behaviour during all three operation modes (electrolysis, ion pump, autonomous) is shown in figure 2.3. It shows the qualitative polarisation curve of an electrochemical cell, separated into sections which characterise the three discussed operation modes.

The majority of electrolytes of EMRs, applied in the area of hydrogen processing,

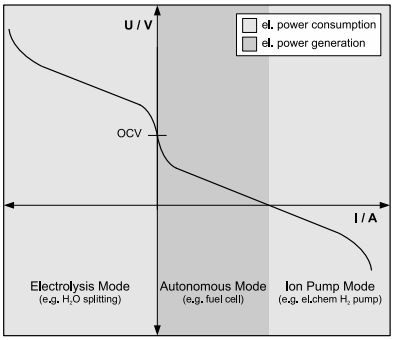


**Figure 2.3.:** Exemplary current-voltage dependence of a electrochemical cell with indicated operation modes.

conduct either $H^+$, $O^{2-}$ or $OH^-$ ions. These charge carrier often define the application field of the EMRs, if used for the production of chemicals. For instance, electrochemically controlled oxidation reactions are conducted with $O^{2-}$ conductors, i.e. solid oxide electrolytes [43, 44], whereas hydrogenations are carried out with $H^+$ conducting electrolytes [45, 46].

Electrochemical $H_2O$ splitting, an electrolysis process, is carried out mainly in alkaline environment to avoid expensive Pt catalysts [23, 47], as well as the conversion of $CO_2$ to formate [48]. However, $H_2O$ electrolysis development activities are also conducted with $H^+$ [22, 24] and $O^{2-}$ conducting electrolytes [22, 25, 49].

All three discussed charge carriers can be also found within the field of fuel cells, i.e. autonomous operating EMRs for power generation. Alkaline fuel cells utilise $OH^-$ conducting membranes or gels [50–52], polymer electrolyte membrane fuel cells (PEMFC) apply $H^+$ conducting membranes [53–55], and solid oxide fuel cells utilise $O^{2-}$ conducting ceramic solid electrolytes [56–58].

Further details regarding the characteristics and technical applications of different types of EMRs are available in several review articles [59–61]. Concepts for the processing of $H_2$ rich gas using EMRs are introduced in the following chapter.

## 2.3 $H_2$-CO Gas Mixtures in Electrochemical Membrane Reactors

The following paragraphs summarize the operation of EMRs with $H_2$ and CO containing gas mixtures. The content resembles the introductory comments of journal contributions by Oettel et al. [62, 63].

### Electrical Power Generation

Electrochemical membrane reactors generating electrical power (i.e. fuel cells) utilise mainly $H_2$ rich feed gas as fuel. As discussed in chapter 2.1, CO is an important by-product of the state of the art $H_2$ generation process. Carbon monoxide contaminations of $H_2$ gas lead, even in low concentrations as 100 ppm, to severe power losses during the operation of PEMFCs [64–66].
The performance loss in PEMFCs results from the adsorption of CO on the active surface sites of the anode catalyst [67, 68]. Thereby, the number of active sites available for the dissociative electro-sorption of hydrogen is reduced. This results, at a constant hydrogen oxidation rate, in an increase of the anodic overvoltage and thus in a lower electrical power output [66, 69]. Three different approaches prevailed within the numerous efforts to minimize the CO contamination problems: (i) the utilization of metal alloys such as Pt-Ru, Pt-Mo, Pt-Sn as the anode catalyst material to promote the electrochemical oxidation of CO by $H_2O$ [66, 70–75] and to lower the equilibrium surface coverage of CO by lowering the CO adsorption energy of CO on Pt [76–78], (ii) the operation at elevated temperatures [66, 79–84] to lower the CO adsorption onto the catalyst, and (iii) the injection of small amounts of $O_2$ into the anode feed stream, known as air or $O_2$ bleeding, decreasing the CO poisoning effect, resulting from a direct CO oxidation by $O_2$ [64, 85, 86].

The decrease of the CO poisoning of PEMFCs with increasing operation temperature is related to the temperature dependency of the standard free Gibbs adsorption energy of CO for its adsorption on Pt ($\Delta G^{\circ}_{CO_{ad}Pt}$). At low temperatures, $\Delta G^{\circ}_{CO_{ad}Pt}$ is highly negative, and its absolute value is decreasing with increasing temperature [87]. Consequently, efforts are being undertaken to increase the operation temperature of PEMFCs by overcoming temperature limitations of the electrolyte membranes [82, 83, 88, 89]. Savinell et al. developed a phosphoric acid ($H_3PO_4$) doped polymer electrolyte, which allows operation temperatures of up to 200°C [89, 90]. At these elevated temperature, the high temperature PEMFC (HT-PEMFC) can operate with CO concentrations up to 3 %, while exhibiting no significant performance losses [91].

**Gas Processing**

The potential of electrochemical membrane reactors in the field of syngas processing was in the focus of several research activities. Various concepts were investigated and developed. Generally, these concepts can be classified into two main applications, being (i) the extraction of $H_2$ from a $H_2$ containing feed gas mixture and (ii) the removal of contaminants, like CO, from $H_2$ containing gas mixture by converting them into inert compounds. In the following, selected examples of research projects related to syngas processing with EMRs are briefly introduced. Details of this works reactor concept are presented in chapter 3.

The electrochemical $H_2$ pumping, where $H_2$ is extracted selectively from the other gas components, is a classical application of EMRs in syngas processing. This process is carried out at operation temperatures ranging from 80 °C up to 900 °C, using different electrode/electrolyte systems [92–95]. Gardner and Ternan investigated the performance of a classical electrochemical proton exchange membrane (PEM) cell for the separation of hydrogen from a $H_2$-$CO_2$ and $H_2$-$CO_2$-CO gas mixture at room temperature. For binary $H_2$-$CO_2$ gas mixtures the $H_2$ extraction efficiency was found to be high. Including CO into the feed gas mixture led to a clear efficiency decrease of the $H_2$ extraction. This result was attributed to a significant reduction of the free electrode active surface sites, being the result of CO surface adsorption [92]. Lee et al. investigated the influence of the current density, temperature and pressure upon the required voltage and $H_2$ product purity of the $H_2$ pumping process with a conventional Nafion-115 PEM electrolyte at temperatures below 70 °C [93]. Matsumoto et al. applied a high temperature proton conductor for the $H_2$ pumping at the considerable higher temperature of 900 °C [95]. Comparable to this work, a polybenzimidazole (PBI) based $H_3PO_4$-doped high temperature proton conducting membrane was used as electrolyte in an electrochemical $H_2$ pump by Perry et al. [94]. Furthermore, a process operating at 200 °C, utilising two single reactors, one for the non-electrochemical WGSR and one for subsequent electrochemical $H_2$ pumping, was presented by Muroyama et al. [96].

Carbon monoxide is one of the most critical contaminants in $H_2$ gas, as it leads to significant performance losses in PEMFCs [64–66, 91]. The removal of CO from $H_2$ rich gas is therefore of high interest and can be conducted with EMR concepts. Similarly to the non-electrochemical PrOx reactor, the electrochemical preferential oxidation reactor (ECPrOx) removes CO in low concentrations by converting it to $CO_2$ via electrochemical CO oxidation [97–100]. The EMR is based on the LT-PEMFC design and operates in the fuel cell mode when removing CO from $H_2$ rich gas. The ECPrOx generates electrical energy, as a fraction of the fed $H_2$ is oxidised

and reacts with cathodic $O_2$ to $H_2O$, while maintaining the driving force of the CO oxidation from the anode gas.

# Chapter 3

# The Electrochemical High Temperature Membrane Reactor

This chapter introduces the setup, properties and the application concepts of the developed electrochemical membrane reactor. At first, the reactor setup is presented in chapter 3.1, including technical parameters and geometrical details. Furthermore, the preparation procedure of the membrane electrode assembly (MEA) and the membrane doping is explained.
Chapter 3.2 introduces the utilisation of the reactor as high temperature polymer electrolyte fuel cell (HT-PEMFC), i.e as reactor which converts the chemical energy of educts into desired electrical energy. This includes the presentation of the operation regime along with the proceeding reactions.
The concept to apply the reactor as a $H_2$ generation and purification unit, the electrochemical water gas shift reactor (EWGSR), is described in chapter 3.3. The EWGSR allows for $H_2$ generation and separation from reformat gas via electrochemical processes. The operation regimes as well as the proceeding reactions are presented.

## 3.1 Reactor Setup

The basic design of the employed electrochemical membrane reactor is similar to PEMFC single cell designs. A schematic illustration of the reactor is shown in figure 3.1. In general, it involves two gas compartments, which are separated from each other by the membrane electrode assembly (MEA). The MEA is a composite element, which consists of a proton conducting polymer electrolyte membrane (PEM) embedded in-between two gas diffusion electrodes (GDE). The GDEs are composed of two layers. The first layer is the gas diffusion layer (GDL), which is in contact with the gas phase present in the gas compartment. The second layer is the reaction active layer of the electrode. It consists of catalyst particles (e.g. noble metal alloy) which are usually intermixed with carbon particles to increase

their active surface area. Furthermore, other functional additives are used within the active electrode layer, which for example, form necessary proton conductive pathways from the active catalyst particles to the proton conductive membrane.

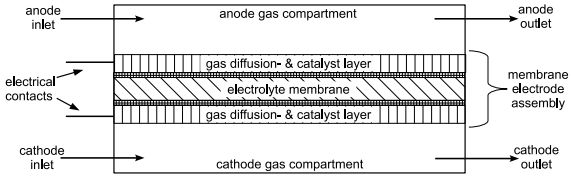


**Figure 3.1.:** Schematic setup of the electrochemical membrane reactor, with indicated inlet and outlet streams, gas diffusion electrodes and the proton conducting polymer electrolyte membrane.

### Flow Field and MEA Frame

The two gas compartments of the reactor were constructed using two similar flow field plates (anode and cathode plate), which possessed parallel gas flow channels. The technical design of the flow field plates is shown in figure 3.2. They were manufactured from carbon composite plates (Sigracet - BBP 4, Eisenhuth, Germany), and served as electrical contact between the MEA and the outer electrical circuit. In contrast to conventional designs, the here employed plate design involved flow field bars which were higher than the outer plate sealing surface (see sectional view in figure 3.2). This arrangement allowed a MEA incorporation by using a custom designed frame structure, along with a gas compartment hight of 1.5 mm.

The employed MEA frame, shown in figure 3.3, was designed to fulfil two functions: (i) to enable a reproducible, repeatable, and easy assembly of the MEA without hot-pressing, and (ii) to serve as sealing between the two gas compartments and the environment. It is designed as a "frame in frame" structure, whereas the inner frame, fastening the PEM, is placed within the outer frame, which anchors the GDEs on both sides of the PEM. A close contact between the GDEs and the PEM was achieved by pressing the flow field plates and the MEA tightly together during the final assembly of the reactor. The MEA frame was made from a poly(tetrafluoroethylene) PTFE composite material (NU 1036, PTFE Nünchritz, Germany), containing additives which increased the deformation resistance at elevated temperatures $\leq$473 K without lowering the required high chemical stability of the frame material.

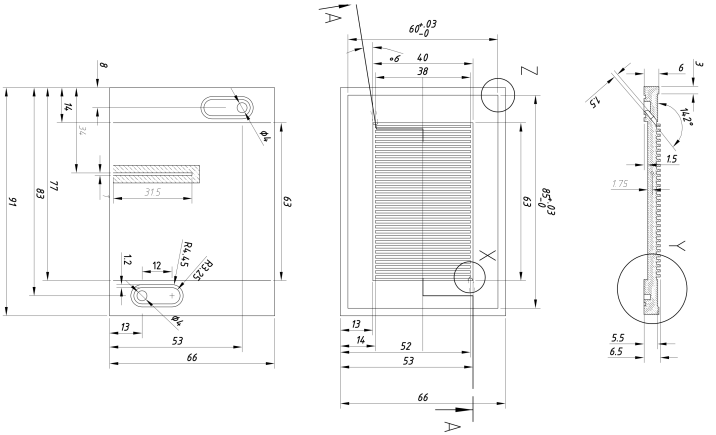


**Figure 3.2.:** Detailed drawing of the reactor flow field plate, with size labels and sectional views.

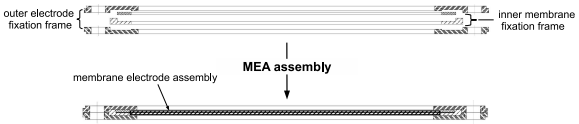


**Figure 3.3.:** MEA frame in open and in assembled state with inserted MEA.

### MEA Components and Preparation

The reactor was designed to operate at temperatures of about $373\,\mathrm{K} < \mathrm{T} \leq 453\,\mathrm{K}$. The motivation for this temperature range is discussed in chapter 3.2 and 3.3, respectively. The operation temperature of an electrochemical PEM reactor depends mainly upon the employed membrane material, which needs to exhibit a high proton conductivity throughout the operational temperature range.

Phosphoric acid doped PEMs were found to exhibit a technical applicable proton conductivity at temperatures above 373 K [88–90, 101, 102]. The developed electrochemical high temperature membrane reactor utilises $H_3PO_4$ doped proton conducting PEMs, which are based on the poly(2,5-benzimidazole)(ABPBI) polymer [103–105]. This polymer has a shorter monomer unit than the more commonly used poly[2,2'-(*m*-phenylene)-5,5'-bibenzimidazole] (PBI) [101, 106–112]. It was supplied as undoped membrane sheets by Fumatech (Germany). The chemical structure of both polymers is shown in figure 3.4.

The doping level of an electrolyte membrane describes the number of $H_3PO_4$

molecules per repeating monomer unit of the polymer. The proton conductivity of $H_3PO_4$ doped PEMs depends highly upon the doping level, as $H_3PO_4$ is the main proton conducting species within these electrolytes [101, 104, 113, 114]. Generally, higher doping levels increase the proton conductivity of the membrane. The control of the membrane doping level during the MEA preparation is therefore of high importance to achieve a reproducible behaviour of the reactor.

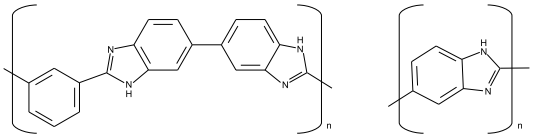


**Figure 3.4.:** Structural formulas of non acid doped poly[2,2'-(*m*-phenylene)-5,5'-bibenzimidazole] (PBI) and poly(2,5-benzimidazole) (ABPBI).

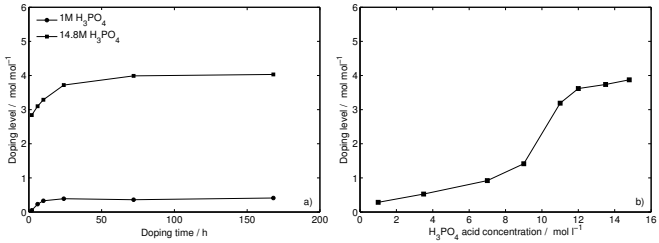


**Figure 3.5.:** a) ABPBI doping level as a function of doping time at two different $H_3PO_4$ doping concentrations (doping temperature: 298 K). b) Membrane doping level as a function of $H_3PO_4$ doping concentration (doping temperature: 298 K, doping time: 72 h).

The ABPBI doping level is a function of the doping time and $H_3PO_4$ doping concentration, as shown in figure 3.5 a and b. It is visible that the doping level is highly dependent upon acid concentration and acid exposure time. Doping levels of up to 4 $^{\mathrm{mol}}/_{\mathrm{mol}}$ were achieved at ambient temperatures. The doping level converges to a maximal value with increasing doping time (figure 3.5 a), whereas the maximal doping level of the polymer increases with increasing acid doping concentrations. Figure 3.5 b displays the doping level as a function of the acid bath concentration, at otherwise unchanged conditions. As visible, the curve exhibits low doping levels at $H_3PO_4$ doping concentrations below 10 M, and a section of high doping levels at $H_3PO_4$ doping concentrations above 10 M. The low doping level section does not significantly exceed the doping level of 1 $^{\mathrm{mol}}/_{\mathrm{mol}}$, which is equivalent to the protonation of the one nitrogen present within the imino group of each ABPBI repeating

unit [101, 115].
Higher doping levels are achieved when additional $H_3PO_4$ is incorporated in-between the polymer chains without possessing a chemical bond to the polymer backbone. The data shown in figure 3.5 b suggest that a rather small concentration interval of $H_3PO_4$ separates the low and high doping level sections of ABPBI, as the doping level increases strongly from 1.4 to 3.2 $^{mol}/_{mol}$ by increasing the $H_3PO_4$ concentration from 9 M to 11 M. The uptake of $H_3PO_4$ in-between the polymer chains leads to a swelling of the membrane and to a lower mechanical membrane stability [116]. The ABPBI membranes used within the final application were doped with either 13 M (fuel cell application) or 12 M (EWGSR application) of $H_3PO_4$ at 353 K for 24 h. The temperature increase allowed to shorten the doping time, while doping levels of about 4.6 and 4 $^{mol}/_{mol}$ were achieved, respectively. During the EWGSR application of the membrane (chapter 3.3), the membrane was exposed to a significant amount of water. The hydrophilic $H_3PO_4$, present within the membrane, caused a water uptake of the electrolyte membrane, which lowered the mechanical stability of the membrane (higher risk of membrane failure). Therefore, a lower doping level (4 instead of 4.6 $^{mol}/_{mol}$) was selected for the EWGSR application, which resulted in a good compromise between reactor durability and reactor performance.

The gas diffusion electrodes, constituting the outer layer of the MEA, were prepared with commercially available gas diffusion layers (HT2500W, E-Tek, Germany). These carbon cloth based GDLs were coated with the respective catalyst to form the electrodes by using the airbrush method. Table 3.1 lists the composition of the prepared catalyst layers with respect to the electrodes. Two types of metal based catalysts, Pt and PtRu, on carbon support were used for the anode. Furthermore, PTFE was incorporated into the catalyst layer to serve as a catalyst binder and as component protecting against $H_3PO_4$ flooding. The active geometric surface area of the electrodes applied in the prepared EMR was 26 $cm^2$.
After the deposition of the catalyst, the electrodes were sintered at 453 K for 2 h and, subsequently, immersed in a 6 M $H_3PO_4$ bath for 24 h at 353 K. The acid bath led to a partial penetration of $H_3PO_4$ into the catalyst layer, which was necessary to ensure a good proton conductive contact between the GDE and the $H_3PO_4$ doped electrolyte membrane.

| property | anode | | cathode |
|---|---|---|---|
| | Pt | PtRu | Pt |
| catalyst | 50 wt% Pt, 50 wt% C | 40 wt% Pt, 20 wt% Ru, 40 wt% C | 50 wt% Pt, 50 wt% C |
| metal loading | 1 mg cm$^2$ | 1 mg cm$^2$ | 1 mg cm$^2$ |
| PTFE loading | 0.8 mg cm$^2$ | 0.8 mg cm$^2$ | 0.8 mg cm$^2$ |

**Table 3.1.:** The catalyst composition, total metal loading, and the PTFE content of the prepared gas diffusion electrodes.

## 3.2 The Reactor as High Temperature PEMFC

This section describes the application of the developed electrochemical high temperature membrane reactor as high temperature polymer electrolyte fuel cell (HT-PEMFC), which was introduced already in chapter 2.3. Information about material durability issues [117, 118] and operation characteristics at various temperatures and CO feed concentrations [82, 91, 108] of the HT-PEMFC technology can be found within literature [53, 88, 102, 119].

Figure 3.6 illustrates the application of the reactor as HT-PEMFC. Similar to

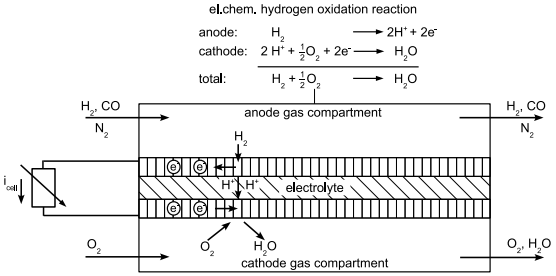


**Figure 3.6.:** Schematic setup of the electrochemical membrane reactor in fuel cell operation mode. All employed inlet and outlet species are indicated, as well as the reactions at anode and cathode, respectively.

the LT-PEMFC operation, $H_2$ is oxidised at the anode to protons and electrons. The protons are transported through the electrolyte membrane to the cathode, where they recombine with oxygen and electrons to $H_2O$. The operation of the HT-PEMFC with CO containing $H_2$ rich gas (product gas of reformat gas processing) was simulated in this study by using different compositions of the $H_2$, CO and $N_2$ containing anode feed gas. The inert $N_2$ balanced different CO inlet concentrations in order to realise a constant molar inlet flow rate during all experiments (see chap-

ter 4.1).

At high operation temperatures (453 K≤T≤473 K), it is generally agreed that the HT-PEMFC performance is unaffected, no severe performance loss due to CO catalyst poisoning, by a anode feed gas CO content of up to 3 mol-% [91]. However, an increase of the temperature above 473 K is not feasible to improve the CO tolerance further. At temperatures above about 403 K, intermolecular condensation starts to influence the stability of $H_3PO_4$, where it is partially converted to diphosphoric acid ($H_4P_2O_7$). The equilibrium of the dehydration is completely shifted to $H_4P_2O_7$ above 473 K [120]. This significantly decreases the number molecules participating in the proton conduction within the membrane and, consequently, lowers the membrane conductivity significantly [117]. Furthermore, the elevated temperature accelerates the degradation of the catalyst layer [118].

Nevertheless, an increased CO tolerance of the HT-PEMFC beyond 3% CO in the feed gas would be highly advantageous. The necessary feed gas processing (i.e. CO removal) in reformat based processes could be significantly simplified [121]. Figure 3.7 displays the influence of the HT-PEMFC CO tolerance upon the complexity of a fuel cell power plant operated with biomass, as proposed by Heidebrecht et al. [122]. It visualises different plant configurations with different CO concentrations at the HT-PEMFC inlet. As shown, a reduction of the feed gas processing steps (e.g. elimination of the PrOx unit) increases the HT-PEMFC CO feed gas concentration, which in turn requires an improved tolerance of the HT-PEMFC against CO poisoning. The possibility to operate the HT-PEMFC with CO feed gas concentrations above 3 mol-% would open further options to e.g. reduce the effort and complexity of the high temperature water gas shift reaction step.

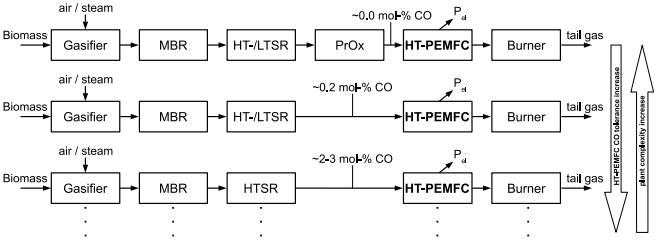


**Figure 3.7.:** HT-PEMFC based fuel cell power plant scheme at different complexity levels in dependence upon the HT-PEMFC CO tolerance (MBR: moving bed reactor, HT-/LTSR: high temperature & low temperature water gas shift reactor, PrOx: preferential oxidation).

As discussed in chapter 2.3, Pt-Ru has been largely applied within LT-PEMFCs to increase the CO tolerance. However, to the author's best knowledge, only the research group of Modestov et al. investigated the application of the Pt-Ru cata-

lyst in HT-PEMFCs [123, 124]. In this study, the possibility to increase the CO tolerance of HT-PEMFCs above the stated limit of about 3 mol-% at $T \leq 453$ K was investigated by using a Pt/Ru anode catalyst. Therefore, the HT-PEMFC was equipped with either a Ru free or Ru containing anode electrode (see table 3.1). The results of these investigations are presented in chapter 4.1.

## 3.3 The Reactor as Electrochemical Water Gas Shift Reactor

This chapter introduces the concept of the electrochemical water gas shift reactor (EWGSR). It summarises descriptions, which were published in advance in two peer reviewed journal articles by Oettel et al. [63, 125].
As discussed in chapter 2.1, state - of - the - art $H_2$ generation routes consist of many different subsequent process units, which are required to conduct the $H_2$ formation reactions and to separate $H_2$ from the remaining components.
Currently, many approaches are investigated which quest to reduce the system complexity of $H_2$ plants. The combination of the non-electrochemical WGSR and a subsequent electrochemical $H_2$ pumping showed to be conceivable option for complexity reduction [96]. Furthermore, the integration of the WGSR and $H_2$ separation into one process unit by refining the stream iron process was shown by Heidebrecht et al. [126, 127]. Electrochemical membrane reactors are applied to conduct electrochemical $H_2$ pumping as $H_2$ separation method [92–95] (see chapter 2.3).

Here, the EWGSR concept is a contribution to these efforts, which aim to improve the $H_2$ production. It aims to simplify the rather complex process routes of state of the art $H_2$ generation processes by merging the secondary $H_2$ forming step (i.e. water gas shift reaction) and the $H_2$ separation step into one process unit.
A possible application of the EWGSR within a $H_2$ plant is illustrated in figure 3.8. It shows two conceptional process charts. The upper one constitutes a state - of - the - art process utilising a pressure swing adsorption unit [14, 38], whereas the lower one visualises the incorporation of the EWGSR into the process. As visible, the EWGSR application makes the water gas shift reactor unit obsolete, as it operates with the high CO concentrations of the reformer effluent. Furthermore, the process charts indicate downstream utilisation options of the process products. The tail gas of the EWGSR is expected to contain besides $CO_2$ still significant amounts of CO and $H_2$ (see chapter 4.3), which can be used in subsequent processes.

The EWGSR generates pure $H_2$ from reformat type gas mixtures. Its operation regime has similarities with the electrochemical $H_2$ pump (ECHP), which has been extensively investigated [92–95]. Similar to the ECHP, the EWGSR is operated with an external electrical power source and during its operation protons are continuously generated at the anode, transported through the electrolyte to the cathode, and reduced at the cathode to gaseous $H_2$.

In contrast to the ECHP operation, the EWGSR is designed to operate with a feed gas containing $H_2$, CO, $H_2O$, and others (a typical steam reformer effluent

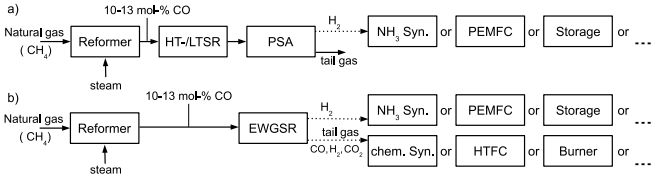


**Figure 3.8.:** Conceptual designs of two $H_2$ plants. a) PSA based (state - of - the - art), b) EWGSR based. (HT-/LTSR: high temperature & low temperature water gas shift reactor, PSA: pressure swing adsorption, HTFC: high temperature fuel cell).

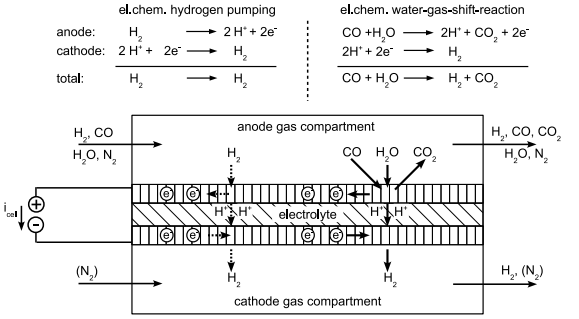


**Figure 3.9.:** Schematic setup of the electrochemical membrane reactor in EWGSR operation mode. All employed inlet and outlet species are indicated, as well as the netto reactions at anode and cathode, respectively.

composition) to generate pure $H_2$ at the cathode side. Thereby, pure $H_2$ is not only extracted from the $H_2$ containing feed gas (see ECHP), but also generated within the reactor via the electrochemical CO oxidation. As indicated in figure 3.9, two reactions proceed during the EWGSR operation: (i) the electrochemical $H_2$ pumping of the $H_2$ feed to the cathode and (ii) the electrochemical water gas shift reaction. Furthermore, figure 3.9 displays the schematic setup of the electrochemical water gas shift reactor (EWGSR) and the inlet and outlet gas components. Details about the single EWGSR components are presented in chapter 3.1.

The EWGSR was equipped with Pt/Ru containing anodes to enhance the CO electro-oxidation (see table 3.1), except for one comparative experiment. The electrochemical oxidation of CO with $H_2O$ on PtRu in electrochemical cells has been the focus of numerous studies and is generally understood [69–72, 98, 128, 129]. Bimetallic anodes play an important role to increase the CO tolerance of LT-PEMFCs [66, 70–72, 128, 130]. However, the electrochemical CO oxidation is only

a minor side reaction in LT-PEMFCs and does not contribute significantly to the cell current. It takes place if the cell is operated in galvanostatic mode and the anode overpotential rises beyond a threshold due to a lack of required active surface sites for the $H_2$ oxidation [69, 129].

In contrast to the fuel cell operation mode, the electrochemical CO oxidation (i.e. electrochemical water gas shift reaction) is within the EWGSR not a side reaction, but one of two main reactions. It is essential for the reactor concept as it unlocks, in the presence of $H_2O$, the CO within the feed gas as source for the generation of pure $H_2$.

In order to generate $H_2$ by electrochemical CO oxidation in a EWGSR, two main conditions have to be fulfilled. Both reactants, CO and $H_2O$, have to be supplied to the electrode surface. However, $H_2O$ should not block the gas distribution channels and the anodic gas diffusion layer for other species. Therefore, operation temperatures above 373 K are advantageous to avoid any blockage of gas transport paths due to condensed $H_2O$. Additionally, the driving force of the reaction needs to be sustained. The driving force is the imposed potential difference between anode and cathode, and can be realised in potentiostatic or galvanostatic operation mode using an external power source. The galvanostatic mode enables a direct control of the cathodic $H_2$ generation rate.

All considered reactions steps, proceeding during the EWGSR operation, are described by the equations 3.1-3.6. They can be summarised into two main reactions. The first reaction is the electrochemical hydrogen pump reaction (ECHPR), which consists of an anodic $H_2$ oxidation to protons and electrons (Eq. 3.1-3.2) and a cathodic $H_2$ evolution where electrons and protons recombine to molecular $H_2$ (Eq. 3.6). The second proceeding reaction is the electrochemical water gas shift reaction (electrochemical WGSR), i.e. electrochemical CO oxidation, where CO is oxidized with $H_2O$ to $CO_2$ at the anode (Eq. 3.3-3.5) [63, 123, 124]. The generated anodic protons and electrons recombine as well at the cathode to molecular $H_2$ (Eq. 3.6), similar to the cathodic reaction of the ECHPR. Within Eq. 3.1-3.6, the $*$ symbol represents a free active surface site on the electrode.

$$\text{Anode:} \quad H_2 + 2* \longrightarrow 2H_{ad} \tag{3.1}$$

$$2H_{ad} \longrightarrow 2H^+ + 2e^- + 2* \tag{3.2}$$

$$CO + * \longrightarrow CO_{ad} \tag{3.3}$$

$$H_2O + * \longrightarrow OH_{ad} + H^+ + e^- \tag{3.4}$$

$$CO_{ad} + OH_{ad} \longrightarrow CO_2 + H^+ + e^- + 2* \tag{3.5}$$

$$\text{Cathode:} \quad 4H^+ + 4e^- \longrightarrow 2H_2 \tag{3.6}$$

During the EWGSR operation, both reactions (ECHPR and electrochemical WGSR) proceed simultaneously at the anode. However, the rate of the reactions can differ significantly under constant operation conditions. In the following, the term anode overvoltage is used to address the total voltage loss in the anode, with respect to open circuit conditions. The electrochemical WGSR requires a higher anode overvoltage than the electrochemical $H_2$ pumping (ECHPR). This is expected to lead to different reaction ratios at different cell voltages. The strong adsorption of CO on Pt influences the ECHPR, as it lowers the number of available active surface sites for $H_2$ adsorption when both CO and $H_2$ are present [69–72, 92, 98, 128, 129].

The study of the EWGSR focused on the experimental characterisation of the reactor, whereas the influence of temperature, feed concentration and cathodic $H_2$ evolution rate (i.e. current density) was investigated. The experimental study is partitioned into two parts. Part one addresses the individual characterisation of the electrochemical WGSR (see chapter 4.2). The results of this study aim at improving the understanding of the interplay of the ECHPR and the electrochemical WGSR, which proceed simultaneously during the EWGSR operation with reformat gas.
In the second part the EWGSR operation with reformat type feed gas was investigated (chapter 4.3). Here, the interdependencies of both proceeding reactions and their influence upon the operation behaviour were analysed. Furthermore, the efficiency of the EWGSR concept was determined based on experimental results, and compared to alternative $H_2$ process routes in chapter 5.

## 3.4 Experimental Test Stand

The EMR was operated within an in-house designed test stand. Figure 3.10 shows its schematic design including important single components. The feed gas control was realised with mass flow controllers (Bronkhorst Mättig GmbH, Germany) for $H_2$, CO, $N_2$, $O_2$, and Air. The required feed gas streams with different composition were achieved by mixing the pure gas streams with the respective flow rates and using $N_2$ as balancing component within the mixture.
Both inlet gas streams (anode and cathode side) were heated to the respective EMR operation temperature before entering the reactor. The reactor temperature was adjusted with the help of a temperature controlled heating sleeve, whereas the temperature sensor was placed within the graphite flow field plates of the reactor.

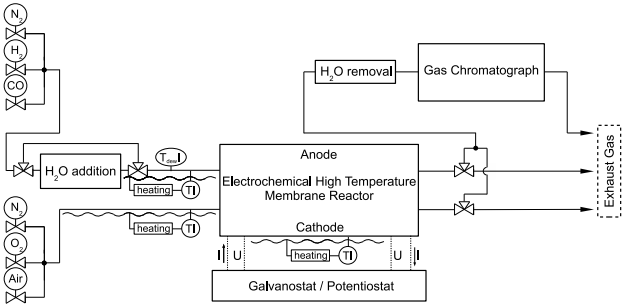


**Figure 3.10.:** Schematic experimental test stand design including main devices, sensors (TI - temperature, $T_{dew}$I - dew point temperature) and gas flow piping.

The experimental test stand was equipped with two serially connected tempered and insulated bubbler flasks to conduct the addition of gaseous $H_2O$ to the anode feed stream (EWGSR operation). This water addition section could be bypassed, which was required if the experiments demanded $H_2O$-free anode feed gas (HT-PEMFC operation).
All gas pipes leading from the bubbler flasks to the reactor, were heated and insulated to prevent condensation and to adjust the temperature of the feed gas to the reactor temperature. The test stand included no back pressure valve control for the anode and cathode gas stream and the effluents left the test stand at ambient pressure. The gas overpressure at the anode and cathode inlet was about 2 kPa and 5 kPa, respectively.

The HT-PEMFC was operated with an electronic load (ZS506-4NV, H&H GmbH, Germany), while the EWGSR experiments were conducted with a potentiostat / galvanostat (AMEL – 7060/7061).

**Feed Gas Humidification**

The molar water flow rate ($G_{H_2O}$) within the anode feed stream was controlled with the dew point temperature $T_{dew}$. The dew point temperature $T_{dew}$ in the anode feed stream was continuously measured after the tempered bubbler flask cascade in a separate flow-through gas chamber, being placed in the anode gas supply piping. The gas temperature at the dew point sensor was with approx. 368 K always higher than the respective dew point temperature $T_{dew}$ of the gas stream.
Assuming a negligible pressure difference between the gas ($T_{dew}$ measurement) and the ambient pressure, the continuously monitored anode gas dew point temperature was used to calculate the numerical values of $G_{H_2O}$ for all applied experimental conditions according to equation 3.7.

$$G_{H_2O} = \frac{p_{H_2O}(T_{dew})}{p_{gas} - p_{H_2O}(T_{dew})} \cdot G_{dry,in} \tag{3.7}$$

This equation was derived from the mass balance around the bubbler flask cascade, assuming ideal gas behaviour and a constant gas pressure $p_{gas}$ (see appendix C). The term $p_{H_2O}(T_{dew})$ represents the vapour pressure within the anode feed gas, being calculated with the Antoine equation using $T_{dew}$.

Figure 3.11 represents a summary of data, which are required for the design of EWGSR experiments. The displayed data were calculated based on equation 3.7, Faraday's law, and the assumption of a stoichiometric turnover during the electrochemical WGSR. The diagram gives a prompt overview on the interdependencies between the volume feed flow rate, the CO content, the dew point temperature and the stoichiometric limit of the CO oxidation current.
Five curves, associated to dry anode volume flow rates (solid grey lines), and several horizontal lines representing CO concentration levels (dashed black lines) are plotted in figure 3.11. The interception points of the flow rate curves and the horizontal CO concentration lines mark the minimal dew point temperatures (readable at the y-axis) which are required within the anode feed gas to reach the stoichiometric limit of the CO oxidation current (readable at the x-axis). In other words, figure 3.11 links the minimal required dew point temperature of the EWGSR feed gas to the maximal possible CO oxidation current (complete CO conversion), in dependence on the volume flow rate (solid lines) and the CO content (dashed lines) of the EWGSR feed gas.

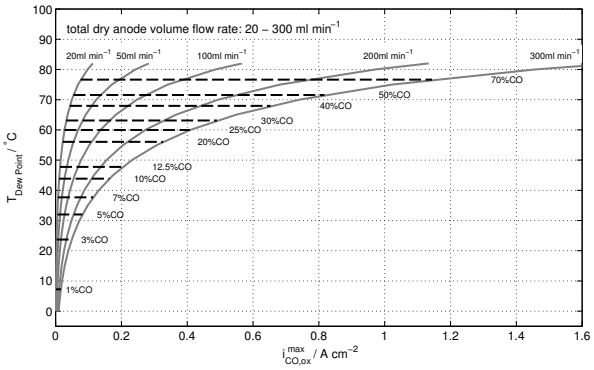


**Figure 3.11.:** The Relationship between the volume feed flow rate, the CO content, the feed gas dew point temperature and the maximal CO oxidation current during EWGSR operation $i^{max}_{CO,ox}$. The indicated CO concentrations and volume flow rates relate to dry gas conditions, prior to a $H_2O$ addition.

### Gas Analysis

The test stand was equipped with a gas chromatograph (GC) from Agilent (type 5890), using an automated gas sample valve. It was used to determine the reactor effluent gas composition (CO, $CO_2$, $H_2$). Here, He was applied as carrier gas, and two columns (HP-Plot/Q and HP-Molesieve) were applied for compound separation. A TCD detector was used for compound detection/quantification and the peaks of the chromatogram were integrated with the Chemstation software from Agilent (version B.04.02 SP1).

The TCD detector signal was calibrated with a series of gas mixtures with known CO, $CO_2$ and $H_2$ concentrations. Water vapour present within the anode effluent was removed before the GC analysis with a cooling trap and a silica gel filled gas dryer. The average of three consecutive GC measurements was used to determine the effluent gas concentrations under steady state conditions. Prior to three associated GC measurements, the reactor was stabilised for 10 minutes. To enable three GC measurements of the anode effluent, the respective current value was applied for 40 minutes. A constant current flow duration of 80 minutes was required to allow for the consecutive GC analysis of the anode and cathode effluent. In this case, six GC measurements in total were required at every applied current value.

# Chapter 4

# Experimental Investigations

This chapter summarises the experimental studies which were conducted with the developed electrochemical high temperature membrane reactor. At first, the collected results during the operation of the reactor as high temperature polymer electrolyte membrane fuel cell (HT-PEMFC) are presented (chapter 4.1). Furthermore, the investigations of the EWGSR operation mode are described and evaluated in chapter 4.2 and chapter 4.3.

## 4.1 CO Tolerance Improvement Study of the HT-PEMFC

This chapter focuses upon investigations which were carried out to characterise the improvement potential of high temperature proton exchange membrane fuel cells (HT-PEMFC) by introducing a platinum-ruthenium alloy as anode catalyst. The electrolyte was a $H_3PO_4$ doped poly(2,5-benzimidazole) polymer (ABPBI).
Steady state operation experiments were carried out in a temperature range between 403 K and 443 K with CO concentrations in the $H_2$ feed gas between 0 and 6.5 mol% CO. Furthermore, the dynamic cell voltage response to a current step was analysed under CO influence. There here presented investigations and results have been published in a peer reviewed journal article by Oettel et al. [62].

### 4.1.1. Motivation

Currently, the on-site hydrogen generation by means of catalytic reforming using hydrocarbon or alcohol feed is considered to overcome the current obstacles of the PEMFC technology, which are related to an insufficient $H_2$ infrastructure [131, 132]. An important by-product of the reforming process is carbon monoxide (CO), which leads, even in such low concentrations as 10 ppm, to severe power losses during the operation of LT-PEMFC [64, 65]. The removal of CO from hydrogen-rich gas to

a very low level requires a series of gas cleaning steps, which increases the system complexity and costs, while decreasing its flexibility.
Therefore, the increase of the CO tolerance of the PEMFC is a important field of research, where two strategies prevail to be highly promising. The first feasible option is the alloying of the Pt catalyst with other metals such as Ru. This showed to reduce the required anode potential to enable the electro-oxidation of adsorbed CO with $H_2O$ (see equation 4.1– 4.3). This reaction removes CO from the catalyst surface and, thus, reduces the influence of CO upon the cell performance [71, 72, 74].

$$CO + * \longrightarrow CO_{ad} \tag{4.1}$$

$$H_2O + * \longrightarrow OH_{ad} + H^+ + e^- \tag{4.2}$$

$$CO_{ad} + OH_{ad} \longrightarrow CO_2 + H^+ + e^- + 2* \tag{4.3}$$

For Pt-Ru catalyst alloys, it has been proposed that the CO adsorption and CO oxidation reaction follows the so-called bi-functional mechanism, where CO is exclusively adsorbed onto the Pt sites (equation 4.1) and water exclusively undergoes a dissociative chemisorption (equation 4.2) at the Ru sites [128, 133]. However, more recent studies have shown that CO adsorbs also onto Ru, resulting in an extension of the pure bi-functional mechanism to the pseudo bi-functional mechanism [73, 134].
The second promising concept to lower the influence of CO in PEMFCs is the increase of the operation temperature [66, 79, 80, 83, 91]. This led to the development of the HT-PEMFC, which tolerates a CO feed gas concentration of 3 mol% at about 473 K [91].
However, an even higher CO tolerance would be advantageous to lower necessary fuel purification efforts and, thus, the fuel cell system complexity. This is especially important if hydrogen-rich gas is generated from e.g. biomass, and simplified overall processes are required for to optimise the conversion of biomass to electricity [121, 122]. Therefore, the electrochemical membrane reactor in fuel cell mode (HT-PEMFC) was systematically investigated to evaluate its operation behaviour under CO influence with either Pt or Pt-Ru anode catalysts.

### 4.1.2. Experimental

The HT-PEMFC was operated within the test stand, which is introduced in chapter 3.4. During all experiments, the HT-PEMFCs were supplied with 320 $ml_N\,min^{-1}$ $O_2$ and 470 $ml_N\,min^{-1}$ $H_2$ at the cathode and anode, respectively. The flow rates are related to standard conditions (273.15 K and 101.3 kPa). The required CO concentration at the anode was realised by introducing a CO gas stream to the anode

feed stream. This anode feed stream was mixed with $N_2$ in order to achieve during all experiments a constant total anode gas input flow rate of 550 $ml_N\,min^{-1}$. The gases were not humidified, and the water in the system came entirely from the cell reaction. The experiments were carried out at the temperatures of 403 K, 423 K, and 443 K. If not stated otherwise, the anode gas CO concentration was 2.2 mol%, 3.6 mol%, 5.1 mol% or 6.5 mol%, whereas the $H_2$ concentration was always 85.5 mol%.
The HT-PEMFC was operated in galvanostatic mode, applying, if possible, consecutive current density steps (0.01; 0.11; 0.21; 0.31; 0.41; 0.51; 0.61 $A\,cm^{-2}$), where each current density value was maintained for a dwell time of 10 minutes to ensure stable experimental conditions.
Due to the constant inlet flow rates, the stoichiometry ratios $\lambda_{H_2}$ and $\lambda_{O_2}$, describing the ratio of the amount of supplied educts to consumed educts ($H_2$, $O_2$), changed with every current step. The $\lambda$ values can be determined from the species inlet flow rate and the respective operation current density. For the current densities of 0.01, 0.41, and 0.51 $A\,cm^{-2}$ and the stated inlet flow rates, $\lambda_{H_2}$ values of 260, 6.33, and 5.1 were achieved, respectively.

### 4.1.3. Results and Discussion

#### Influence of CO Feed Concentration

The performance of a Ru-free HT-PEMFC was used as reference within this study to evaluate the impact of Ru on the cell performance.
First, the Ru containing HT-PEMFC (Ru HTPEMFC in the following) and the Ru-free HT-PEMFC were operated with CO-free anode feed gas. Figure 4.1 shows the current voltage dependence of both HT-PEMFC types at a temperature of 423 K. The cell voltage decreased expectedly as a function of the applied current density for both investigated cells. Qualitatively, both cells delivered closely similar cell voltage - current density characteristics. Numerically, the current-voltage dependence with the Ru-free HT-PEMFC cell was slightly better than that of the Ru HT-PEMFC, e.g. at a current density of 0.51 $A\,cm^{-2}$, the cell voltage was 0.510 V (Ru-free HT-PEMFC) vs. 0.470 V (Ru HT-PEMFC).

If CO was introduced to the feed, the cell behaviour changed significantly. Figure 4.2 illustrates the influence of anodic CO (3.6 mol%) upon the polarisation curve at a temperature of 423 K. At a low current density, both the cells behaved practically similar. The cell voltage decreased expectedly with the applied current and the measured cell voltages were close to each other at the current density of 0.11 $A\,cm^{-2}$ (see figure 4.2). At this current density the cell voltage of the Ru-free HT-

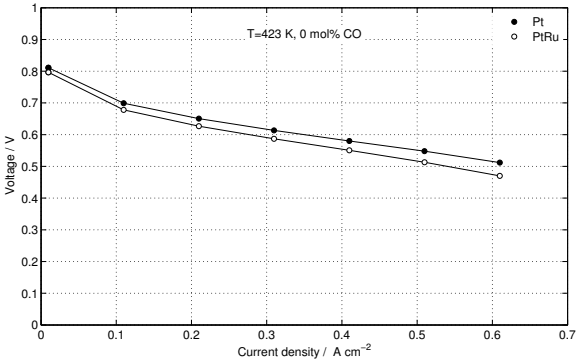


**Figure 4.1.:** Polarisation curves of the Ru free and Ru containing HT-PEMFCs, recorded with 85 mol% $H_2$ and no CO within the anode feed gas at a temperature of 423 K.

PEMFC (0.626 V) constituted 96.3% of the Ru HT-PEMFC cell voltage (0.650 V). However, the operational voltage output of the two cells differed strongly when the applied current density was increased above 0.11 $\mathrm{A\,cm^{-2}}$. The cell containing the Pt-Ru anode exhibited a clearly higher cell voltage, and the deviation between the two cell types is most pronounced at the highest current densities. As example, at a current density of 0.51 $\mathrm{A\,cm^{-2}}$ the measured cell voltage with the Ru-free HT-PEMFC was 0.162 V, being only 39.2% of the corresponding Ru HT-PEMFC voltage (0.413 V). The highest possible current density with the Ru-free HT-PEMFC was 0.61 $\mathrm{A\,cm^{-2}}$ which resulted in a voltage of 0.072 V, whereas the Ru HT-PEMFC obtained a cell voltage of 0.346 V at the same current density and temperature.

The dependency of the cell voltage upon CO concentration has been investigated in detail for Ru-free HT-PEMFCs [91]. The present study expands upon these results by comparing between two different anodic catalysts.

It is well known that CO causes poisoning of the anode catalyst, which strongly lowers the performance of PEM type fuel cells. The strong CO adsorption reduces the amount of active catalyst sites available for $H_2$ oxidation. This either results in the decrease of the $H_2$ oxidation rate (i.e. current density) during potentiostatic operation or an increase of the anode polarisation (i.e. anodic overvoltage) during galvanostatic operation. The latter operation mode was used in this study.

Generally, the electrode overvoltage which drives the electrochemical reactions, e.g.

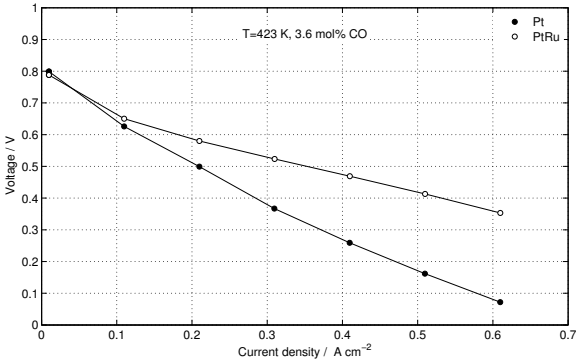


**Figure 4.2.:** Polarisation curves of the Ru free and Ru containing HT-PEMFCs, recorded with 85 mol% $H_2$ and 3.6 mol% CO in the anode feed gas at a temperature of 423 K.

the anode overvoltage $\eta_A$(i), is linked to the overall cell voltage $U_{cell}$(i), which can be expressed according to equation 4.4:

$$U_{cell}(i) = E_{i=0} - \eta_A(i) + \eta_C(i) - iR_{cell} \tag{4.4}$$

where $E_{i=0}$ is the open circuit voltage, $\eta_C$(i) is the cathodic overpotential, and $iR_{cell}$ summarises the ohmic voltage losses within the cell.

The experimental determination of the cell voltage is rather simple. However, as seen in equation 4.4, the cell voltage comprises of several contributions resulting from thermodynamics ($E_{i=0}$), from the anode and cathode performance ($\eta_A$(i) and $\eta_C$(i)), as well as from the electrolyte conductivity ($iR$).

In order to separate the CO catalyst poisoning effect from other processes influencing the cell voltage, the difference in the cell voltage resulting from the influence of CO was calculated using equation 4.5. Here, the recorded cell voltage measured under CO influence (CO in feed gas), $U_{cell,H_2/CO}$(i), was subtracted from the cell voltage recorded without CO influence (no CO in feed gas), $U_{cell,H_2}$(i), under otherwise equal operation conditions (temperature, cell current density, catalyst). Assuming that all other contributions of $U_{cell}$(i) (equation 4.4), besides $\eta_A$(i), are not influenced by the anodic feed CO content, the calculated voltage difference, $\Delta U_{cell,CO}$(i) in equation 4.5 is directly related to the influence of CO on the anode and represents the anode overvoltage caused by CO. The voltage difference $\Delta U_{cell,CO}$(i) is called CO voltage loss in the following.

$$\Delta U_{cell,CO}(i) = U_{cell,H_2}(i) - U_{cell,H_2/CO}(i) = \eta_{A,H_2}(i) - \eta_{A,H_2/CO}(i) \tag{4.5}$$

Figure 4.3 a illustrates the measured CO voltage loss $\Delta U_{cell,CO}(i)$ as a function of the CO feed concentration, calculated according to equation 4.5, with the Ru-free HT-PEMFC at the current density of 0.51 A cm$^{-2}$. The CO concentration was varied from zero up to 5.1 mol%.

The CO voltage loss was strongly dependent on the CO concentration. At the temperature of 423 K, a CO voltage loss of 0.440 V was measured with the CO feed concentration of 3.6 mol%. Higher temperatures lowered the CO influence. The corresponding voltage loss at a temperature of 443 K and the same CO feed concentration was 0.233 V. It was not possible to carry out a measurement with the Ru-free HT-PEMFC cell at 404 K and $i = 0.51$ A cm$^{-2}$, as the overall cell voltage collapsed already at a lower current density due to CO poisoning.

If the CO voltage losses observed with the Ru-free HT-PEMFC cell (figure 4.3 a)

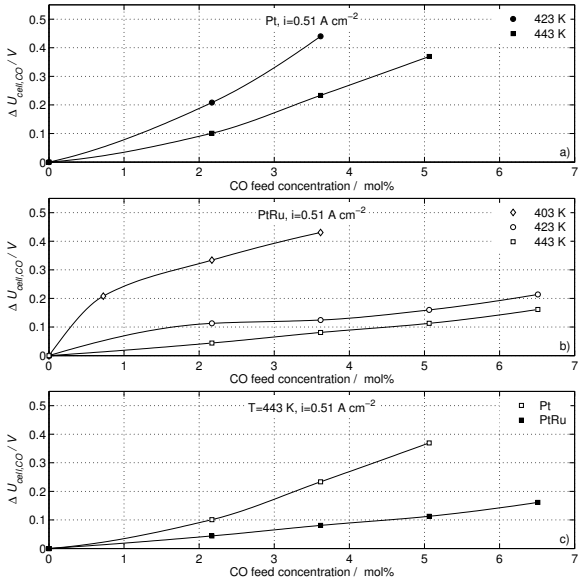


**Figure 4.3.:** The CO voltage loss as a function of the CO feed gas concentration: a) Ru-free HT-PEMFC, at a current density of $i = 0.51$ A cm$^{-2}$ and an operation temperature of 423 K and 443 K; b) Ru HT-PEMFC, at a current density of $i = 0.51$ A cm$^{-2}$ and an operation temperature of 423 K and 443 K; c) Ru-free HT-PEMFC and Ru HT-PEMFC, at a current density of $i = 0.51$ A cm$^{-2}$ and an operation temperature of 443 K.

are compared to those measured with the Ru HT-PEMFC (figure 4.3 b), a clear difference can be observed.

For the Ru HT-PEMFC the CO voltage loss was clearly lower than the corresponding values of the Ru-free HT-PEMFC measurements. The cell equipped with the Pt-Ru anode could be operated at $i = 0.51\ \mathrm{A\,cm^{-2}}$ with CO concentrations up to 3.6 mol% at the temperature of 404 K. The CO voltage loss at 404 K increased with the CO concentration, whereas a steep increase was present in the low CO concentration range (0-0.7 mol% CO). At the anode feed gas concentration of 3.6 mol% CO and 404 K, a CO voltage loss of 0.430 V was reached, being close to the value obtained with the Ru-free HT-PEMFC operated at 423 K.

The CO voltage loss increased also as a function of CO concentration at the temperatures of 423 K and 443 K, as clearly seen in figure 4.3 b. However, the influence of the CO feed gas concentration on the CO voltage loss was less pronounced than at the lower temperature 403 K.

The rise of the CO voltage loss was more gradual at 423 K and 443 K than at 404 K. The experimental data show, that the voltage loss values were slightly lower for 443 K, if compared to the values obtained at 423 K. Here, a maximal CO voltage loss of 0.160 V was measured at $i = 0.51\ \mathrm{A\,cm^{-2}}$, 6.5 mol% CO and 443 K, whereas the CO voltage loss increased to 0.214 V at 423 K and otherwise equal operation conditions (Figure 4.3 b).

By comparing the results in the figures 4.3 a and b it is clearly visible, how the application of a Pt/Ru alloy as anode catalyst improves the CO tolerance of a HT-PEMFC significantly. To further highlight this point, figure 4.3 c directly compares the CO voltage loss of both applied cells for the temperature of 443 K and $i = 0.51\ \mathrm{A\,cm^{-2}}$. The difference in the CO tolerance between the two applied catalyst types is obvious, and more pronounced at high CO feed concentrations. For example, the CO voltage loss decreased from 0.370 V to 0.113 V with 5.1 mol% CO in the feed by replacing the Pt anode catalyst with the Pt-Ru bimetallic alloy.

**Influence of Temperature**

The CO voltages loss as a function of the operation temperature is illustrated in figure 4.4 for both types of applied HT-PEMFCs and two differed CO feed gas concentrations. It was not possible to apply a current density of $0.51\ \mathrm{A\,cm^{-2}}$ to the Ru-free HT-PEMFC at 404 K. Figure 4.4 illustrates the CO voltage loss for this cell only at temperatures of 423 K and 443 K. For the Ru containing HT-PEMFC, experimental results determined at the temperatures of 404 K, 423 K and 443 K are shown.

As illustrated in figure 4.4, a significant influence of the operation temperature upon the measured CO voltage loss was observed. The CO voltage loss of the Ru HT-PEMFC decreased sharply when the temperature was increased from 404 K to 423 K. This phenomenon can be seen for the CO concentrations of 2.2 mol% and

3.6 mol%.

It might be concluded, that two factors positively influence the operation at a higher temperature. First, the CO adsorption is weaker, which lowers the anode overvoltage as more unoccupied active sites are available for the hydrogen electro-oxidation. Secondly, a direct CO electro-oxidation with $H_2O$, produced in the cathode reaction and possibly transported through the electrolyte membrane, might also occur to a larger extent at a higher temperature, especially when a Ru containing catalyst is applied. This agrees well with the observations made by Modestov et al. [123], who operated with humidified feed gas.

In summary, the Ru HT-PEMFC exhibited higher cell voltages, i.e. it shows a

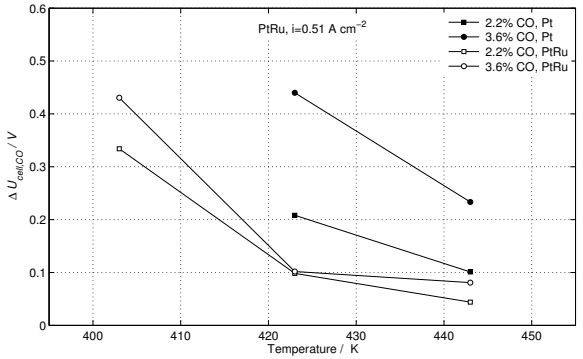


**Figure 4.4.:** The CO voltage loss as a function of the operation temperature, shown for the Ru-free HT-PEMFC and Ru HT-PEMFC operated with 2.2 and 3.6 mol% CO in the anode feed gas.

clearly higher CO tolerance, than the Ru-free HT-PEMFC at every investigated temperature, CO concentration and current density during steady state operation. Consequently, anodic Pt-Ru catalysts in ABPBI based HT-PEMFCs enhances the CO tolerance, exceeding the well known beneficial effect of elevated operation temperatures. The obtained results coincide well with the known CO tolerance enhancing effect of the Pt-Ru catalyst in conventional low temperature PEMFCs [66, 71–76, 78, 134, 135]. The presented results clearly show that a CO tolerance enhancement of the HT-PEMFC can not only be reached by increasing its operation temperatures, but also by an optimal catalyst adjustment.

### Voltage Transient Behaviour

The second part of the HT-PEMFC experimental study focused upon the transient behaviour of the cell voltage after a load change.

At first, the cell voltage transient was determined after a small current step of 0.01 $A\,cm^{-2}$ from open circuit conditions ($i = 0.0\ A\,cm^{-2}$) to 0.01 $A\,cm^{-2}$ with the Ru containing and Ru free HT-PEMFC. The voltage transients at 443 K are shown in figure 4.5 exemplary for the anode feed gas without CO and with 5.1 mol% CO. The applied load change at $t = 0$ resulted in an expected immediate cell voltage drop under all conditions. The relaxation of the cell voltage, corresponding to the applied current density, occurred rapidly without a visible overshoot for both the tested Ru free and Ru containing HT-PEMFCs. This holds for the operation with and without CO in the anode feed gas. It was experimentally observed that the voltage transients of the Ru HT-PEMFC were practical identical for 0 mol% up to 5.1 mol% CO. The phenomenon can be clearly seen in the magnification (figure 4.5), which enlarges the first 100 seconds after the current step.

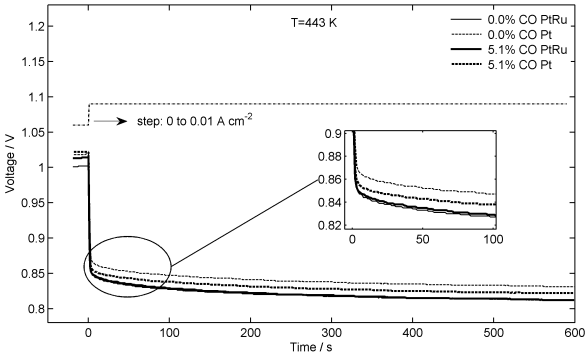


**Figure 4.5.:** The voltage response as a function of time, recorded with the Ru-free HT-PEMFC and the Ru HT-PEMFC at $T = 443$ K with 0.0 and 5.1 mol% CO in the anode feed gas, after a load change from open circuit conditions to $i = 0.01\ A\,cm^{-2}$.

The transient behaviour of the CO voltage loss after the low current step (0 $A\,cm^{-2}$ to 0.01 $A\,cm^{-2}$) is shown in figure 4.6 for the Ru-free HT-PEMFC. As can be seen, a small CO voltage loss was recorded for the Ru-free HT-PEMFC. No CO voltage loss could not be detected for the Ru HT-PEMFC ($\Delta U_{cell,CO}(i) = 0$) during the low current step. This phenomenon is seen also in figure 4.5 by the overlapping of the cell voltages recorded with the Ru containing catalyst.

Nevertheless, one should note here that even with Ru-free catalyst, the CO voltage loss was very small, and the overall difference between the two investigated cells (Ru-free and Ru HT-PEMFC) is minor under the conditions shown in figure 4.5 and 4.6. Hence, in this current density range, no conclusions can be made with respect to the CO tolerance of the two catalyst types.

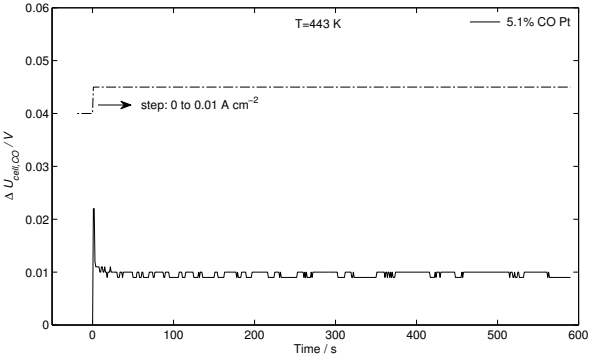


**Figure 4.6.:** The CO voltages loss response function of the Ru-free HT-PEMFC, operated at $T = 443\,K$ with 5.1 mol% CO in the anode feed gas after a load change from open circuit conditions to $i = 0.01\ A\,cm^{-2}$.

A sharp, peak-like overshoot of the CO voltage loss can be observed in figure 4.6 for the Ru-free HT-PEMFC. This overshoot can be attributed to a slightly faster voltage response of the cell if operated under CO influence. The deviation was, however, observed only for a very short time and it disappeared after two seconds. It might be suggested, that this effect is related to a possibly lower capacity of the anodic electrochemical double layer, caused by a higher CO surface coverage if compared to the CO free operation.
Besides this very sharp initial overshoot at $t = 0$, the temporal course of the CO voltage loss (figure 4.6) was unchanged throughout the experiment and the voltage loss was approximately 0.01 V with the Ru-free HT-PEMFC.

Cell voltage transients of the Ru HT-PEMFC and Ru-free HT-PEMFC after a current step of $0.1\ A\,cm^{-2}$, from $0.41\ A\,cm^{-2}$ to $0.51\ A\,cm^{-2}$, are exemplary depicted in figure 4.7 for the anode feed CO concentrations of 0.0 and 5.1 mol%.
Focusing first on the CO free operation, it can be stated that the cell voltage responses were practically instantaneous for both catalysts applied, and followed directly the current change by exhibiting a fast step without any distortion or overshoot. However, under CO influence (5.1 mol%) the cell voltage transients exhibit a significant voltage overshoot after the load change. Here, the observed overshoot was clearly more pronounced for the Ru-free HT-PEMFC.

The relaxation course of the voltage transients after the initial overshoot showed for both used catalysts similarities to a first-order system known from the systems theory [136]. Such systems approach a stable operation in an asymptotic manner. The difference of the cell voltage loss caused by CO, after a current step of

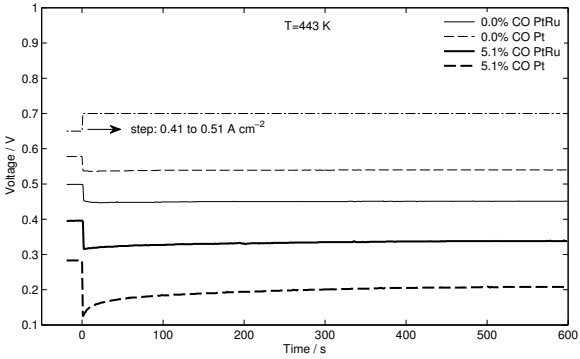


**Figure 4.7.:** The voltage response function of the Ru-free HT-PEMFC and the Ru HT-PEMFC operated at $T = 443\,K$ with 0.0 and 5.1 mol% CO in the anode feed gas, after a current step from $i = 0.41\ A\,cm^{-2}$ to $i = 0.51\ A\,cm^{-2}$.

$0.1\ A\,cm^{-2}$ was calculated for both applied HT-PEMFCs according to equation 4.5, and is shown as a function of time in figure 4.8 for the CO concentration of 5.1 mol% at 443 K.

This illustration shows clearly the overshoot of the CO voltage loss after the load change for both catalysts used. The peak overshoot intensity, i.e. difference between the steady state value and the overshoot peak, for the Pt catalyst was with 82 mV much higher than that of the respective value for the Pt-Ru catalyst operation (24 mV). The time span necessary to reach the steady state after a current step did not differ significantly between the Ru-free HT-PEMFC and Ru HT-PEMFC. However, the absolute difference between the initial, maximal CO voltage loss and its steady state value was always smaller for the Ru HT-PEMFC.

The described findings indicate that the dynamic behaviour of HT-PEMFCs utilizing a mono-metallic Pt anode catalyst is more severely influenced by CO, than the HT-PEMFCs utilizing a Pt-Ru alloy anode catalyst. In particular, the lower overshoot peak values of the voltage transient, exhibited by the Ru HT-PEMFCs, indicate a significantly shorter overall response time of the electrode processes and faster dynamics of the electrode reactions, as less electrode polarisation was necessary to enable the increased electrical current flow.

Influencing factors of the lower electrode polarisation could be a larger fraction of available anodic active surface sites with adsorbed hydrogen, a larger capacity of the anodic electrochemical double layer, or a higher hydrogen concentration in the gas phase of the anodic catalyst layer. As the hydrogen concentration was constant during all conducted experiments, the last factor might be excluded.

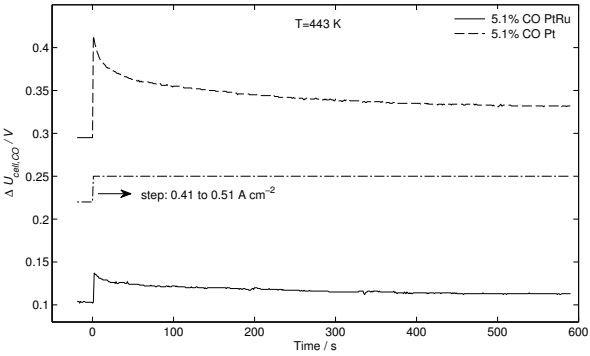


**Figure 4.8.:** The CO voltage loss response function of the Ru-free HT-PEMFC and the Ru HT-PEMFC, operated at $T = 443$ K with 0.0 and 5.1 mol% CO in the anode feed gas, after a load change from $i = 0.41$ A cm$^{-2}$ to $i = 0.51$ A cm$^{-2}$.

However, a larger fraction of available anodic active surface sites for the Ru-containing catalyst might be a reason for the observed lower overshoot of the CO voltage loss compared to the Ru-free catalyst. It was reported that Ru influences the CO adsorption behaviour onto Pt as it leads to weaker CO adsorption energies [76–79]. This in turn could lead to a lower CO surface coverage and a larger fraction of available active surface sites for hydrogen oxidation at the anode.
If a higher amount of active surface sites is available in the Ru containing catalyst for the hydrogen reaction, the intrinsic hydrogen oxidation rate at each active surface site is lower under equal galvanostatic conditions. Consequently, a lower electrode polarisation is needed to drive the lower surface site related reaction rate. The possible dependency of the anodic electrochemical double layer capacity upon the CO surface coverage was already briefly discussed for the low current step (figure 4.6). Unlike adsorbed hydrogen, CO is not able to release an electron and form an ion under the investigated operation conditions. This would be necessary for the build-up of an electrochemical double layer. Hence, it might be suggested that a lowering of the hydrogen surfaces coverage by a higher CO adsorption, likely leads to a lower capacity of the anodic electrochemical double layer.

In summary, the presence of Ru within the anode catalyst reduces the influence of CO upon the voltage transient behaviour of HT-PEMFC, if compared to Ru free anode catalysts. This finding directly influences the optimisation of control strategies for HT-PEMFC systems.

**Carbon Monoxide Tolerance**

It was shown in figure 4.4 that the Ru-free HT-PEMFC exhibited an increasing CO tolerance with increasing temperatures. This dependency, a result of a lower CO poisoning of the Pt catalyst at higher temperatures due to a lower total CO catalyst surface adsorption, is in good agreement with the results of Li et al. [91]. Furthermore, the here presented results showed very clearly that the Ru containing HT-PEMFC exhibits a similar dependency of the CO tolerance upon temperature, which is most likely caused by a decreased CO coverage of the active surface at elevated temperatures.
But, when the performance of the Ru containing and Ru-free HT-PEMFC are compared directly to each other, a clearly improved CO tolerance of the Ru containing HT-PEMFC is observed. In the following, the CO voltage loss transients after a high current step (see figure 4.8) are used to discuss the nature of the CO tolerance increase of HT-PEMFCs due to the presence of Ru at the anode.

Within the low temperature PEMFC literature it has been reported that the presence of Ru in Pt based catalyst promotes the electrochemical CO oxidation with $H_2O$ [66, 70–75], and leads to the weakening of the bond between CO and Pt and thus lowers the equilibrium surface coverage of CO on Pt [76–78].
The low initial CO voltage loss overshoot after the current step $\Delta i = 0.1\ \mathrm{A\,cm^{-2}}$, at $t = 0$ for the Pt-Ru catalyst (see figure 4.8) indicates that only a slight polarisation increase of the Pt-Ru anode is needed to enable the higher current controlled hydrogen oxidation rate. On the contrary, the immediate CO voltage loss of the Ru-free HT-PEMFC after the equal current step is significantly larger. This can be interpreted as a more intensive polarisation of the Pt anode, which is necessary to drive the increased $H_2$ oxidation rate.
The necessity of the initially stronger anode polarization could result from a smaller amount of free active surface sites available at the Pt anode for the $H_2$ oxidation, compared to the Pt-Ru anode. Following this argumentation, Ru might lower the CO adsorption coverage on the anodic active catalyst sites of the Ru HT-PEMFC, according to similar findings in low temperature PEMFCs [76–78].

A second well known effect of Ru in low temperature PEMFCs, is the reduced overpotential of the electrochemical oxidation of CO with $H_2O$ (equation 4.1–4.3). During the operation of HT-PEMFCs with dry feed gases, anodic $H_2O$ can only be provided by back-diffusion of $H_2O$ formed at the cathode [137], or by an undesirable $O_2$ crossover and a consecutive chemical $H_2$ oxidation at the anode.
Focusing upon the relaxation of the CO voltage loss after the initial overshoot in figure 4.8 (i.e. a recovery of the overall cell voltage), it could be suggested that this time-dependent decrease results from a gradual removal of CO from the catalyst

surface by electrochemical oxidation with $H_2O$, which is transported by diffusion from the cathode to the anode. The $H_2O$ diffusion would strongly depend upon the electrolyte membrane conditions. However, indications of the presence of a certain anode onset overvoltage, needed for the electrochemical CO oxidation, were not found during the experiments.
Independent of the current density step and the corresponding initial anode polarisation, the qualitative behaviour of the CO voltage loss transients was similar during all current density steps between 0.11 $\mathrm{A\,cm^{-2}}$ and 0.61 $\mathrm{A\,cm^{-2}}$ for both catalysts.
Therefore, it might be concluded that the Ru promoted electrochemical CO oxidation contributes, if present, only weakly to the observed enhanced CO tolerance of the Ru HT-PEMFC.

**Conclusions**

The results of the investigation about the influence of Ru upon the CO tolerance of HT-PEMFCs summarise as follows::

1. It was possible to show that Pt-Ru alloys improve the CO tolerance of ABPBI based HT-PEMFCs in a similar manner as it is well known for low temperature PEMFCs.
2. The anode catalyst based on Pt-Ru alloys improved the CO tolerance of HT-PEMFCs beyond the known improved temperature dependent CO tolerance. Under all investigated conditions with anodic CO, the performance of the Ru containing HT-PEMFC was superior to HT-PEMFCs with Pt catalysts.
3. The reported data suggests that the CO tolerance increase of Ru containing HT-PEMFCs might result from a reduced adsorption of CO onto the catalyst surface, additional to the temperature dependent CO poisoning mitigation in this fuel cell type.
4. The investigation of the voltage transient after a load change under CO influence showed an instantaneous overshoot after the current increase, followed by a relaxation period which exhibited similarities to a classical first-order system. This characteristic was dampened by the utilization of the Pt-Ru anodic catalyst, as the CO voltage loss overshoot peak was lowered, compared to the Pt anodic catalyst.

## 4.2 EWGSR Study with CO Containing Feed Gas

This chapter describes the first part of the experimental EWGSR study, which focused upon the generation of $H_2$ from CO and $H_2O$ via the electrochemical CO oxidation.
The reactor operation was investigated at 403 K and 423 K with a $H_2$ free anode feed stream of humidified CO and $N_2$. The described experiments and results were published as individual peer reviewed journal article by Oettel et al. [63].

### 4.2.1. Motivation

The EWGSR reactor concept and its advantages over state-of-the-art processes (see chapter 2.1) was discussed in chapter 3.3.
It was shown in figure 3.9, that two reactions proceed simultaneously during the intended operation of the EWGSR. In order to understand the reactor operation behaviour under different conditions, it is important to investigate first the EWGSR characteristics under single reaction conditions. In the case that the feed gas contains only $H_2$ and no CO, $H_2$ is oxidised and reduced within the EWGSR (see equation 3.1, 3.2, 3.6). This electrochemical $H_2$ pump mode was in the focus of several research studies and is well understood [92–95]. However, the intended driven electrochemical CO oxidation within a electrochemical membrane reactor has been, to the authors best knowledge, hardly investigated [124], let alone in context of the EWGSR concept.
The driven electrochemical CO oxidation was experimentally investigated as option to generate $H_2$ from CO and $H_2O$. The occurring reaction steps of the electrochemical water gas shift reaction (i.e. electrochemical CO oxidation) can be described with the equations 3.3-3.5. An externally applied potential gradient between anode and cathode drives the $H^+$ through the electrolyte membrane to the cathode where they recombine with electrons, supplied from the electrical circuit, to $H_2$ (equation 3.6).
The experiments which are presented in the following were conducted to determine the influence of operation conditions upon the CO electro-oxidation during the EWGSR operation. The obtained results contribute strongly to the understanding of the EWGSR operation with reformat type feed gas, which is the topic of chapter 4.3.

### 4.2.2. Experimental

During all experiments, the inlet flow rate of the bubbler flask cascade was 200 $ml_N\,min^{-1}$, i.e. a total dry molar flow rate $G^{tot}_{dry,in}$ of $1.49{\cdot}10^{-4}$ $mol\,s^{-1}$ at the bubbler inlet. The bubbler inlet gas stream was a mixed stream of CO and $N_2$ with varied concentrations of CO. The molar water flow rate within the wet reactor inlet stream was calculated to be about $G_{H_2O} = 1.12{\cdot}10^{-4}$ $mol\,s^{-1}$ during all experiments. The influence of the temperature on the operation of the EWGSR was investigated at 403 K and 423 K. The influence of the CO concentration on the operation was determined with three different anodic CO concentrations, being listed in table 4.1. In the following presentation and discussion of the experimental results, the dry anode inlet CO gas concentrations will be used to refer to the respective experiment. The dew point temperature of the anode feed gas was set to 351 K, resulting in wet anode inlet streams with approx. 43 mol% water and altered CO concentrations in the wet inlet gas (see table 4.1). The resulting molar ratios of $H_2O$ to CO within the anode feed gas at the reactor inlet are listed in table 4.1 as well.

| $T_{dew}$ / K | dry gas /mol% | wet gas /mol% | | molar ratio / - |
|---|---|---|---|---|
| | CO | CO | $H_2O^*$ | $\frac{G_{H_2O}}{G_{CO}}$ |
| 351 | 12.5 | 7 | 43.0 | 6.1 |
| 351 | 25.0 | 14 | 43.0 | 3.1 |
| 351 | 50.0 | 28 | 43.0 | 1.5 |

**Table 4.1.:** Applied anode feed gas compositions (assuming ideal gas conditions) during the experiments with CO containing feed gas. Species fractions are listed for the dry and wet anode feed gas ($^*$ calculated from the dew point).

The EWGSR was operated in galvanostatic mode with current densities varying from 0 to 0.11 $A\,cm^{-2}$. Each experiment consisted of a voltage measurement at open circuit conditions and five consecutively applied constant current densities. At every investigated CO concentration the applied current densities were set to reach CO conversions of 0%, 5%, 10%, 15%, and 20%. Finally, one measurement point (10% CO conversion) was always repeated and the obtained EWGSR voltage was compared to the previous one to assure a degradation free operation. The reproducibility of the results was excellent, so the repeated measurement points are not shown in the illustrations.

The composition (CO, $CO_2$, $H_2$) of the reactor anode and cathode effluents was analysed during the experiments with the Agilent gas chromatograph (GC) (type 5890).

The ohmic resistance of the EWGSR, constituting of the membrane resistance and all other electric resistances, was estimated based upon results of preliminary electrochemical $H_2$ pump experiments in the current density range of 0.1-0.2 $A\,cm^{-2}$. During these experiments, the anode and cathode gas compartments were flushed with $H_2$, using high flow rates to avoid transport limitations. The electrochemical cell was operated under steady state conditions at several current densities (dwell time 2 min) and the voltage response was measured using a potentiostat. The anode overpotential of the $H_2$ oxidation, as well as the cathode overpotential of the $H_2$ evolution was assumed to be negligible.

### 4.2.3. Results and Discussion

#### Feasibility of the EWGSR Concept

At first, the postulated EWGSR operation principle, see chapter 3.3, was verified. Furthermore, Pt and PtRu were compared to each other with respect to their applicability as anode catalysts in the EWGSR.
Two different types of EWGSR reactors were prepared. One was equipped with a Pt containing anode and one with a PtRu containing anode. Their electrochemical operation behaviour can be compared in figure 4.9, which depicts the measured EWGSR voltage as a function of the applied current density. Under open circuit conditions, the measured open circuit voltage (OCV) was negative for both the Pt and PtRu anode electrode. However, the Pt containing EWGSR (Pt-EWGSR) exhibited an open circuit voltage (OCV) of -0.160 V, which was clearly lower than the OCV of PtRu containing EWGSR (PtRu-EWGSR, -0.012 V).
In general, the OCV of an electrochemical cell is the result of different electrochemical double layer (ECDL) potentials at its electrodes. Different chemical species on the electrode surface or different surface concentrations of one chemical compound lead to different ECDLs and different ECDL potentials. It is most likely that two different catalysts exhibit a different surface species composition in an otherwise unchanged setup. As the EWGSR cathodes were identical in both reactors, it can be assumed that the observed OCV deviation results from different ECDLs (i.e. surface species compositions) at the utilized anode catalysts (Pt and PtRu).
Both Pt and Ru catalyse the WGSR [30, 130]. The non-electrochemical WGSR is probably taking place in minor extent at the anode catalyst surface, as traces of $CO_2$, a product of the WGSR, were detected in the anode effluents under OCV conditions with $CO_2$ free inlet gases. However, the kinetics of the WGSR on Pt at 423 K is slow and the $H_2$ concentration in the anode effluent stayed below the GC

detection limit.

Nevertheless, small amounts of $H_2$ are probably present in the anodic catalyst layer. This would enable the CO hydrogenation at the Ru containing catalyst surface, which would result in $CH_4$ via a multi-step reaction mechanism [138–140].

The possibility of CO hydrogenation by $H_2$ (originating from the WGSR) under OCV conditions, increases the variety of possible surface species at the catalyst highly. Hence, the strongly deviating OCV value, measured with the two different catalysts, might be influenced by two different surface species compositions, leading to the OCV deviation between the Pt-EWGSR and the PtRu-EWGSR.

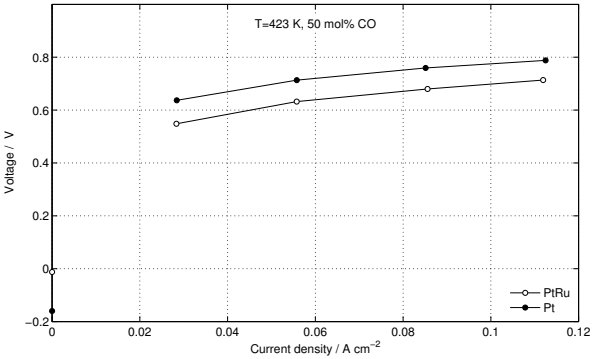


**Figure 4.9.:** Current voltage curve of the electrochemical water gas shift reactor with a Pt or a PtRu anode, operated at 423 K with 50 mol% CO (related to the dry feed stream).

At the lowest applied current density (0.0281 A cm$^{-2}$), the obtained EWGSR voltages were 0.637 V and 0.548 V for the Pt-EWGSR and PtRu-EWGSR, respectively (see figure 4.9). These voltage values, measured under galvanostatic operation, were caused by an increase of the anode potential. This potential increase was required for the activation of the electron supplying electrochemical oxidation of CO by $H_2O$ (equation 3.3-3.5).

Furthermore, it is clearly visible that the Pt-EWGSR required higher voltages than the PtRu-EWGSR at all applied current densities. The voltage difference between the two polarisation curves under current flow is relatively stable, ranging between 75 mV and 90 mV.

This observation agrees well with published results, which describe the behaviour of Pt and PtRu as anode material below 373 K. PtRu alloy catalysts are widely applied in LT-PEMFCs, if operated with a CO containing anode feed gases [66, 69, 98, 129, 130]. Ruthenium within a Pt based catalyst lowers the necessary overpotential for the dissociative chemisorption of $H_2O$ (equation 3.4), which is considered

to be the initial step of the CO oxidation [66, 70–72, 128, 130].
Qualitatively, the dependence of the voltage on the current density is closely similar for both applied anode catalysts. Both polarisation curves exhibit a nearly linear dependence upon the current density above the current density $i = 0.056\ \mathrm{A\,cm^{-2}}$ (see figure 4.9). The ratio of the voltage change to the current change in the interval from $0.056\ \mathrm{A\,cm^{-2}}$ to $0.112\ \mathrm{A\,cm^{-2}}$ correlates well with an estimated total ohmic cell resistance ($R_{cell}$) of approx. $50\,\mathrm{m\Omega}$. This cell resistance value was obtained from voltage-current measurements during separate ECHP experiments (not shown here). These experiments were conducted with the EWGSR cell setup at low current densities to avoid any mass transport limitation influences upon the measured voltage.

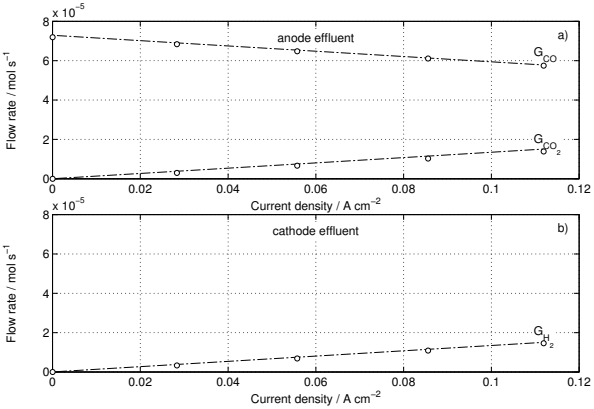


**Figure 4.10.:** Molar flow rates of CO, $CO_2$ and $H_2$ within the anode and cathode effluent as a function of the applied current density, recorded at 423 K with 50 mol% CO (related to the dry feed stream).

The molar flow rates of CO and $CO_2$ in the anode effluent, as well as the $H_2$ molar flow rate in the cathode effluent are shown in figure 4.10a and 4.10b, respectively. The flow rate data are average values, determined from three GC analysis at the respective operation point. These flow rates directly correspond to the polarisation curves shown in figure 4.9.
The measured CO, $CO_2$ and $H_2$ concentrations from both the Pt-EWGSR and PtRu-EWGSR, obtained at equal current densities, were closely equal. Thus, only the molar flow rates of the PtRu-EWGSR experiment are presented in figure 4.10. The circle symbols mark the experimentally determined values, and the dashed line represents the values calculated from the applied current with Faraday's law.
The experimental values in figure 4.10a and 4.10b coincide with the respective

dashed line, showing that the EWGSR operation follows quantitatively Faraday's law within the range of applied current densities. The molar flow rate of CO ($G_{CO}$) in the anode effluent (figure 4.10a) decreases with increasing current density and the molar flow rate of $CO_2$ ($G_{CO_2}$) increases accordingly, confirming the electrochemical CO oxidation (equation 3.3-3.5).
The $H_2$ generation in the cathode compartment, which expectedly is proportional to the current density, is shown in figure 4.10 b. Here, the molar flow rate of $H_2$ ($G_{H_2}$) within the cathode effluent increases as a function of the current, starting with $G_{H_2}$=0 $mol\,s^{-1}$ at i=0 $A\,cm^{-2}$ and rising up to $G_{H_2}$=1.46·10$^{-5}$ $mol\,s^{-1}$ at i=0.112 $A\,cm^{-2}$.
The $CO_2$ flow ($G_{CO_2}$) in the anode effluent corresponds very well with the generated hydrogen $G_{H_2}$. The maximal observed mass balance deviation was about 5%, measured at the highest current density. This deviation might be assigned to inaccuracy and reduced sensitivity of the TCD detector for gas chromatographic hydrogen analysis.
Due to the excellent correlation between the measured $G_{H_2}$ and $G_{CO_2}$ flow rates, the analysis of the cathode effluent was omitted in the further EWGSR experiments. As seen clearly in figure 4.10a and 4.10b, $G_{H_2}$ can be directly deduced based upon the respective $G_{CO_2}$ flow rate by considering Faraday's law.

In summary, the results in figure 4.9 and figure 4.10 clearly show that both utilized anode catalysts (Pt and PtRu) enable EWGSR operation which follows strictly Faraday's law. As the PtRu-EWGSR exhibited lower voltages than the Pt-EWGSR catalyst, all further experiments were carried out only with the anodic PtRu catalyst.
The electrical power demand of the EWGSR is directly correlated to the operation voltage. Therefore, the lower voltages obtained with the PtRu anode catalyst are especially advantageous for the optimisation of the EWGSR operation.

**Influence of Temperature and CO Concentration**

Figure 4.11 displays the EWGSR voltage as a function of the current density at three different CO concentrations (12.5 mol%, 25.0 mol% and 50.0 mol%) and two different operation temperatures (403 K and 423 K). During each measurement the applied current densities were chosen to achieve five defined CO conversions, which were equal for all applied CO feed gas concentrations. The selected CO conversions were 0%, 5%, 10%, 15% and 20%.
The resulting current density intervals for different CO concentrations partially overlap, as seen in figure 4.11. All polarisation curves, recorded for the different

CO concentrations, contain a voltage value measured at the current density of i=0.028 A cm$^{-2}$.

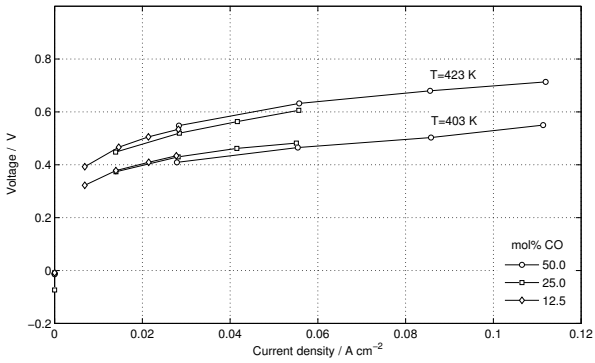


**Figure 4.11.:** Current voltage curves of the electrochemical water gas shift reactor with a PtRu anode, recorded with various different CO feed gas concentrations at 403 K and 423 K.

As can be seen in figure 4.11, the recorded polarisation curves are grouped within the diagram according to the operation temperature of the EWGSR. Furthermore, the polarisation curves recorded at one temperature were found to be nearly independent from the CO feed gas concentration.

At the current density of i=0.028 A cm$^{-2}$, the cell voltages of 0.43 V, 0.43 V and 0.41 V were measured at 403 K for 12.5 mol%, 25.0 mol% and 50.0 mol% CO, respectively. At the same current density, the cell voltages of 0.55 V, 0.52 V and 0.53 V were measured at 423 K for the same feed gas compositions. The obtained results suggest that the electrochemical CO oxidation exhibits a reaction order of zero, with regards to the CO feed gas concentration and the investigated operation conditions, as the CO concentration changes did not influence the EWGSR operation behaviour.

However, it is generally accepted that the reaction kinetics of the electrochemical CO oxidation depends mainly upon the catalyst surface coverage of the participating species. The anode CO surface coverage was not investigated in detail within this study and more in-depth investigations would be required for a final statement regarding the reaction order of the CO oxidation.

Figure 4.11 shows that the temperature influences clearly the EWGSR operation. For the current density of i=0.028 A cm$^{-2}$, the measured voltage was about 100 mV lower at 403 K than the voltage obtained at 423 K. This behaviour of the EWGSR voltage holds for all applied CO feed gas concentrations and current densities.

Such a reverse temperature dependency is not typical for chemical and electro-

chemical reactions, as normally higher temperatures increase the rate of reaction or lowers the required overpotential at a constant reaction rate, according to the Arrhenius equation. Therefore, it can be assumed that a process or mechanism, differing from the intrinsic surface reaction, dominates the EWGSR voltage temperature dependence.
The conductivity of the applied electrolyte membrane is a function of the temperature and the relative feed gas humidity (RH) [101, 104]. The RH value is defined as the ratio of the partial water pressure in the feed gas to the saturation pressure of water vapour at the respective temperature. Asensio et al. reported for $H_3PO_4$ doped ABPBI electrolyte membranes that the membrane conductivity increases with temperature and RH [104]. The water flow rate $G_{H_2O}$ was constant during all EWGSR experiments. Consequently, when the temperature was increased from 403 K to 423 K, the RH value decreased. When the temperature increases and the RH decreases, they lead, if considered separately, to a conductivity increase and conductivity decrease, respectively.
Considering the results of Asensio et al., it is a reasonable assumption that the influence of the temperature change and the RH change upon the membrane conductivity counterbalanced each other under the used experimental conditions. Consequently, the observed strong influence of the temperature upon the EWGSR operation is likely not resulting from an alternating membrane resistance. However, the temperature significantly influences the CO adsorption behaviour and, thus, it might influence the electrochemical CO oxidation.
The electrochemical CO oxidation is a multi step reaction, as CO first adsorbs on the electrode surface and is subsequently oxidised (see Equations 3.3-3.5). Consequently, the reaction rate might depend rather on the CO surface concentration than on the CO gas concentration, which was similar at both operation temperatures.

In the following, a kinetic model equation, describing the electrochemical CO oxidation rate among others in dependence on the CO surface coverage, is used to elucidate the observed temperature dependence of the EWGSR voltage. For this purpose the kinetic equation (equation 4.6) from Baschuk et al. [141] is chosen. The equation describes the CO electro-oxidation rate $r_{CO}^{ox}$, using a reaction constant $k_{CO}^{ox}$, the CO surface coverage $\Theta_{CO}$ of the catalyst and the anode overpotential $\eta_A$ within a sinus hyperbolicus function, derived from the Butler-Volmer equation.

$$r_{CO}^{ox} = k_{CO}^{ox} \cdot \Theta_{CO} \cdot sinh\left(\frac{\eta_A \cdot z \cdot F}{R \cdot T}\right) \tag{4.6}$$

The terms $R$, $T$ and $z$ represent the universal gas constant, the operation temperature and the number of transferred electrons, respectively. The inserted number of transferred electrons is two, as two electrons are generated during the oxidation of one CO molecule.

Equation 4.6 does not contain in particular the OH surface coverage. This implies the assumption that an alternation of the OH formation rate (equation 3.4) or changes of OH surface coverage have no significant influence upon the CO oxidation rate. The influence of OH upon $r_{CO}^{ox}$ is embedded into the reaction constant $k_{CO}^{ox}$. This applies if the anode potential is high enough to facilitate the dissociative chemisorption of $H_2O$ (generation of adsorbed OH) according to equation 3.4 [71, 72, 98], and the influence of the $H_2O$ concentration and mass transport can be neglected.

The onset potential of the OH formation was reached in every experiment already at the lowest measured current density. This can be deduced from figure 4.10, as the measured effluent flow rates of CO ($G_{CO}$) and $CO_2$ ($G_{CO_2}$) correlate well with the stoichiometry of the electrochemical CO oxidation equation 3.3-3.5 at every current density. The $H_2O$ concentration within the anode feed gas exceeded with appox. 43 mol% clearly the CO concentrations and was constant during all experiments.

It is assumed that the $H_2O$ concentration within the catalyst layer was similar at equal current densities throughout the experiments. Possible changes of the $H_2O$ mass transport due to the temperature difference of 20 K were neglected. Therefore, the possible influence of the $H_2O$ transport upon the OH formation (and the EWGSR voltage) at identical current densities is assumed to be similar at both temperatures.

Measured $iR$ corrected overvoltages, recorded at one current density and one operation temperature can be applied to equation 4.6 as $\eta_A$. For this purpose the $iR$ corrected EWGSR voltages, recorded with $i = 0.028\ \mathrm{A\,cm^{-2}}$ and CO feed gas concentration of 25.0 mol% at 403 K and 423 K, were used (figure 4.11). This was motivated by assuming that the influences of the cathode overpotential (necessary for the $H_2$ evolution by reducing $H^+$), of the equilibrium potential, and of the anode concentration overpotential upon the EWGSR voltages are negligible. The respective $iR$ corrected EWGSR voltages are $U_{EWGSR}^{403\,K}$=0.388 V and $U_{EWGSR}^{423\,K}$=0.494 V.

The previously obtained cell resistance of approx. 50 mΩ was used for the $iR$ correction. Due to the identical current density ($i = 0.028\ \mathrm{A\,cm^{-2}}$), the CO oxidation rates, $r_{CO}^{ox,403\,K}$ and $r_{CO}^{ox,423\,K}$, are considered to be equal. Hence, a relation can be deduced from equation 4.6, which includes the voltages and temperatures of both operation points. All other terms, except of the respective reaction constants $k_{CO}^{ox}$ and CO surface coverages $\Theta_{CO}$ are known. Consequently, equation 4.6 leads to the ratio $(k_{CO}^{ox,403\,K} \cdot \Theta_{CO}^{403\,K}) / (k_{CO}^{ox,423\,K} \cdot \Theta_{CO}^{423\,K}) \approx 116$.

The CO oxidation rate constant (equation 4.6) can be assumed to follow the Ar-

rhenius relation [141], leading to $k_{CO}^{ox,403\,K} < k_{CO}^{ox,423\,K}$. Consequently, if equation 4.6 applies, the surface coverage of CO must be significantly higher at 403 K than at 423 K ($\Theta_{CO}^{403\,K} \gg \Theta_{CO}^{423\,K}$), regardless of the exact $k_{CO}^{ox}$ values.
The CO electro-oxidation activation energy was estimated by Modestov et al. to be in the range of 110 kJ mol$^{-1}$ [124]. If this value is applied numerically to obtain the $k_{CO}^{ox,403\,K}/k_{CO}^{ox,423\,K}$ ratio, a value for $\Theta_{CO}^{403\,K}/\Theta_{CO}^{423\,K}$ larger than 500 can be calculated. However, one should notice here that the anode feed gas water concentration was not constant during the experiments of Modestov et al., which precludes a direct application of their findings to our analysis.
The concluded increase of the CO surface coverage at lower temperatures coincides well with the known temperature dependency of the CO adsorption on Pt. Carbon monoxide adsorbs stronger on Pt surfaces at lower temperatures, due to its negative free Gibbs adsorption energy, which decreases with decreasing temperatures [87]. This dependency was shown experimentally for Pt and PtRu containing PEMFC electrodes by Pitois et al. and Davies et al., respectively [142, 143].
Therefore, it is concluded that the observed lower cell voltage at 403 K probably results from a higher catalyst CO surface coverage, if compared to 423 K. The higher CO surface coverage supports the CO electro-oxidation as more catalyst sites are occupied by CO, which increases the probability of the reaction between CO and adsorbed OH.

The above described temperature dependence, however, disagrees with the findings of Modestov et al. who observed a decrease of the operation voltage with increasing temperatures during a driven CO electro-oxidation, using cyclic voltametry [124]. In principle, their reactor setup was comparable to this study. However, the operation conditions are not comparable to the experimental conditions of the here presented study. The anode feed gas concentration was significantly lower (approx. 7 mol%) and the measurements were not conducted under steady state conditions. Furthermore, it should be pointed out that Modestov et al. increased the $H_2O$ concentration in the anode feed gas along with the temperature to keep the relative humidity of the feed gas constant throughout the investigated temperature range. This might have resulted in the lower voltages at higher temperatures as reported by Modestov et al.. The increased $H_2O$ feed gas content at higher temperatures significantly increased the stoichiometric ratio of $H_2O$ to CO at the catalyst surface. The higher $H_2O$ feed gas content likely overbalanced the inhibiting effect of a lower temperature dependent CO surface coverage during the experiments of Modestov et al., as it increases the CO oxidation rate at low CO concentrations.
Additionally, the kinetics of the non electrochemical WGSR is faster at higher temperatures, generating $H_2$ which can be pumped to the cathode side at a lower anode overpotential than necessary for the electrochemical CO oxidation.

**Power Demand**

In contrary to the conventional water gas shift reactor, which optimally does not require additional energy supply due to the exothermic reactions, the EWGSR is operated with electrical energy.
However, the utilization of electrical power enables a simultaneously hydrogen purification, which is the unique feature of the EWGSR. Figure 4.12 shows the generated $H_2$ as a function of the applied electrical power density ($P_{el}$) with Pt and PtRu anodic catalyst, carried out with a CO feed gas concentration of 50 mol%. The values in figure 4.12 are related to the geometrical surface area of the EWGSR electrode.
Figure 4.12 shows clearly that the PtRu-EWGSR, operated at 403 K, generates the

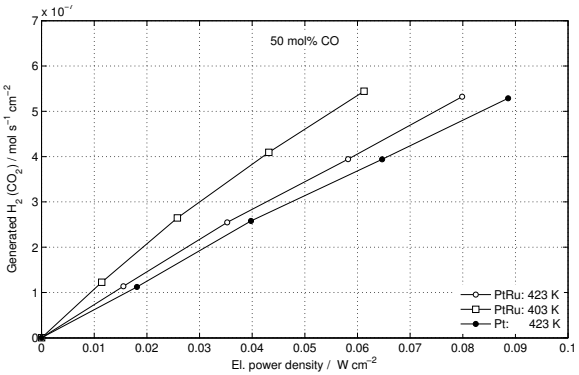


**Figure 4.12.:** Hydrogen generation rate as a function of the required electrical power density, obtained with a Pt and a PtRu anode at 403 K or 423 K, 50 mol% CO (related to the dry feed stream), balanced by $N_2$.

highest amount of $H_2$ at a power of 0.06 W cm$^{-2}$, followed by the PtRu-EWGSR operation at 423 K. The lowest $H_2$ generation was obtained with the Pt-EWGSR at 423 K.
This dependency of the $H_2$ generation rate upon the applied anode catalyst and operation temperature was valid for the whole range of applied electrical power. The generation of approx. $5.3 \cdot 10^{-7}$ mol s$^{-1}$ cm$^{-2}$ $H_2$ with the PtRu-EWGSR at 403 K required only 69 % of the electrical power which was necessary with the Pt-EWGSR at 423 K. At the temperature of 423 K, only 90 % of the Pt-EWGSR electrical power demand was necessary with PtRu-EWGSR to obtain the same hydrogen generation rate.
The results in figure 4.12 show that the electrical power demand of the EWGSR

was significantly lowered by lowering the temperature and using PtRu as catalyst. It is likely that the electrical power demand could be further lowered by optimising the electrodes and further adjustment of operation conditions.

**Conclusions**

The results of the study, which was dedicated to electrochemical CO oxidation within the EWGSR can be summarised in the following points:

1. The feasibility of the concept to simultaneously generate and separate $H_2$ via a driven electrochemical water gas shift reaction was demonstrated.
2. It was experimentally verified that the CO oxidation and $H_2$ evolution follows Faraday's law and take place in one process step.
3. The application of PtRu as anode catalyst, instead of Pt, leads to significant lower EWGSR voltages at the same $H_2$ generation rate, and, thus, to a lower electrical power demand.
4. The experiments at constant temperatures with 12.5 mol% to 50 mol% CO showed that under $H_2$ free conditions the EWGSR voltage was only slightly dependent upon the CO concentration.
5. Low operation temperatures were found to be favourable for the EWGSR operation with only CO in the feed gas. This is probably a result of the CO adsorption behaviour on Pt, as the CO adsorption is more pronounced at lower temperatures, and this, presumably enhances the CO oxidation kinetics.

## 4.3 EWGSR Study with $H_2$ and CO Containing Feed Gas

This chapter introduces the results of the experimental EWGSR study, where the reactor was operated with $H_2$ and CO as active species within the feed gas. The study focuses upon the interplay of the simultaneously proceeding electrochemical reactions, electrochemical pumping and the electrochemical CO oxidation (see equation 3.1-3.5), and their influence upon the EWGSR operation characteristics. Several operation parameters were varied and their influence upon the EWGSR operation characteristics (e.g. cell voltage, electrochemical CO oxidation, the energy demand etc.) was investigated.
The described experiments and results were published as a individual peer reviewed journal article by Oettel et al. [125].

### 4.3.1. Motivation

The EWGSR reactor concept and its advantages in comparison to state-of-the-art processes (see chapter 2.1) was discussed earlier.
In contrast to chapter 4.2, the EWGSR was operated here with anode feed gas containing $H_2$ and CO as active species. It was shown in figure 3.9, that these two species likely simultaneously participate in two different reactions during the intended operation mode of the EWGSR.
The rates of the single reactions are expected to vary in dependence upon the operation conditions. For example, the electrochemical WGSR (see equation 3.3-3.5) requires a higher anode overvoltage than the electrochemical $H_2$ pumping (ECHPR) (see equation 3.1, 3.2). This is expected to lead to varying reaction ratios at different cell voltages. Furthermore, temperature and other operation conditions most likely influence the single reactions rates and, consequently, the utilisation degree of each species.
In order to evaluate the feasibility of the EWGSR concept, the influence of temperature, voltage and concentration need to be understood to identify optimised operation conditions. Additionally, the simultaneously proceeding of the ECHPR and the electrochemical WGSR need to be characterised to allow for adjustments of the EWGSR operation with respect to the desired anodic product gas.

### 4.3.2. Experimental

Two sets of experiments were carried out. Initially, the influence of temperature, CO and $H_2$ concentration, and cathode purge flow rate on the cell voltage was investigated without gas analysis. Here, the EWGSR was operated in galvanostatic mode by consecutively increasing the current density in steps of 0.01 $A\,cm^{-2}$ up to a maximal current density of 0.39 $A\,cm^{-2}$, while applying a dwell time of two minutes at each current density.

The second set of experiments was carried out with the analysis of the reactor effluent gas. Here, open circuit conditions and five current densities (0.06 $A\,cm^{-2}$, 0.17 $A\,cm^{-2}$, 0.28 $A\,cm^{-2}$, 0.39 $A\,cm^{-2}$, 0.17 $A\,cm^{-2}$) were applied to the EWGSR. The operation at the current density of 0.17 $A\,cm^{-2}$ was repeated in order to detect possible reactor degradations during the experiment. The reproducibility of the results was excellent so that the performed repeated measurements are omitted in the illustrations.

Three different temperatures (393 K, 403 K, 413 K) were used during the experiments. The employed concentrations of $H_2$, CO and $H_2O$ in the anode feed gas as well as the molar feed ratio of $H_2O$ to CO ($G_{H_2O}/G_{CO}$) are summarised in Table 4.2. Please note that in the following discussion, CO and $H_2$ concentrations related to the dry anode feed stream (before the addition of $H_2O$) are used to refer to the respective experimental data.

Two different dew point temperatures ($T_{dew}$), 351±1 K and 345±1 K, were used

| $T_{dew}$ / K | dry gas /mol% | | wet gas /mol% | | | molar ratio / - |
|---|---|---|---|---|---|---|
| | $H_2$ | CO | $H_2$ | CO | $H_2O^*$ | $\frac{G_{H_2O}}{G_{CO}}$ |
| 351 | 50 | 10.0 | 28.5 | 5.7 | 43.0 | 7.54 |
| 351 | 50 | 12.5 | 28.5 | 7.1 | 43.0 | 6.06 |
| 351 | 50 | 25.0 | 28.5 | 14.3 | 43.0 | 3.01 |
| 351 | 50 | 50.0 | 28.5 | 28.5 | 43.0 | 1.51 |
| 345 | 50 | 12.5 | 33.2 | 8.3 | 33.5 | 4.01 |
| 351 | 60 | 12.5 | 34.2 | 7.1 | 43.0 | 6.06 |
| 351 | 70 | 12.5 | 40.0 | 7.1 | 43.0 | 6.06 |

**Table 4.2.:** Applied anode feed gas compositions (assuming ideal gas conditions) during the experiments with CO and $H_2$ containing feed gas. Species fractions are listed for the dry and wet anode feed gas (* calculated from the dew point).

during the experiments for the addition of $H_2O$ into the anode feed stream. This led to an added molar water flow rate $G_{H_2O}$ of $1.12{\cdot}10^{-4}$ $mol\,s^{-1}$ and $0.75{\cdot}10^{-4}$ $mol\,s^{-1}$, respectively. The determination of the molar water flow rate using the

dew point temperature is described in chapter 4.2.2.
During all experiments, the total volume flow rate of the dry anode feed gas stream was set to 200 $ml_N\,min^{-1}$. As illustrated in figure 3.9, the cathode compartment was purged with $N_2$ in most of the EWGSR experiments. If not stated otherwise, the cathode was purged with $N_2$ at a flow rate of 200 $ml_N\,min^{-1}$.
The reactor effluent was monitored using the gas chromatography, as introduced in chapter 3.4. Using the GC, $H_2$, CO and $CO_2$ were not detected within the EWGSR cathode effluent under open circuit conditions. Furthermore, the components CO and $CO_2$ were not detected within the cathode effluent during the EWGSR operation. Thus, the crossover of these species through the electrolyte membrane is negligible.

### 4.3.3. Results and Discussion

#### Polarisation Curve

In contrast to the previous EWGSR study (no $H_2$ in the feed gas, chapter 4.2), the EWGSR was operated here with an anode feed gas mixture of CO and $H_2$. This leads to two possible current driven anodic reactions, namely (i) the electrochemical $H_2$ oxidation (equation 3.1-3.2) and (ii) the electrochemical CO oxidation (equation 3.3-3.5).
Figure 4.13 shows a polarisation curve, recorded with an anode feed gas composition of 12.5 mol% CO and 50 mol% $H_2$ at 393 K. The recording started at $i = 0.01$ $A\,cm^{-2}$ where a cell voltage of -0.057 V was measured. The cell voltage is the sum of the Nernst voltage and the voltage losses under current flow (e.g. ohmic losses, activation losses, etc.). As long as the cell voltage is negative, the EWGSR operates as galvanic cell, i.e. spontaneous electric current flow. When the cell voltage is positive, the electric current is driven by the external power source.
Within the current range of 0.01 - 0.07 $A\,cm^{-2}$ the observed cell voltage increased linearly with the applied current. Here, the observed behaviour is suggested to result mainly from the ohmic resistance of the EWGSR and the proportional increase of the cathodic $H_2$ concentration with increasing current (equation 3.6). The $H_2$ concentration increase at the cathode reduces the concentration gradient between anode and cathode, thus, it lowers the concentration dependent potential difference between the electrodes.
In the current range of 0.08-0.17 $A\,cm^{-2}$ the cell voltage increases more intensely at every current density step. Within this current range, the cell voltage exhibits an increase from 0.079 V to 0.411 V. This part of the polarisation curve indicates a

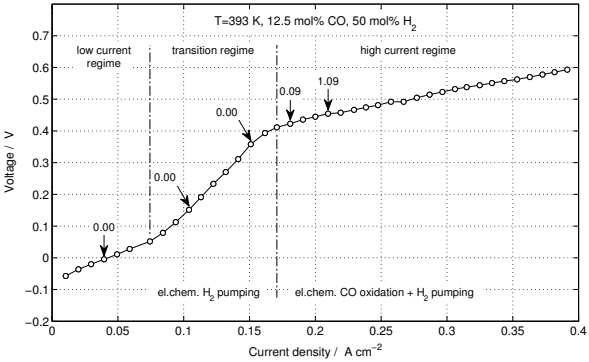


**Figure 4.13.:** A typical EWGSR polarisation curve with indicated operation regimes, recorded at T=393 K with an anode feed gas containing 12.5 mol% CO and 50 mol% $H_2$ (related to the dry feed stream). The anode effluent $CO_2$ concentration, determined using GC analysis, is displayed for five selected operation points.

transition in the cell operation, wherefore it is addressed in the following as transition regime.

A second linear part of the polarisation curve is observable in figure 4.13 in the current density range of 0.17-0.39 $A\,cm^{-2}$. However, the voltage increases to a lesser extent with increasing current than observed first linear part of the polarisation curve (low current regime). The linearity within this third regime might result from the superposition of several influencing factors, being a Tafel-type dependence of the $H_2$ and CO electro-oxidation, ohmic voltage losses of the EWGSR, the current-dependent cathode potential and the alternation of the potential-dependent anode catalyst CO coverage.

At selected current densities, the anode effluent $CO_2$ concentration was measured as indicated in figure 4.13. Considering the applied operation temperature and the anode feed gas components, the only possible $CO_2$ source within the process is the water supported electrochemical oxidation of CO to $CO_2$ (equation 3.3-3.5). As seen in figure 4.13, no $CO_2$ was detected at low currents up to a current density of 0.15 $A\,cm^{-2}$ (0.358 V). The first indication of a CO electro-oxidation was found at a current density of 0.18 $A\,cm^{-2}$ (0.423 V), where an anode effluent $CO_2$ concentration of 0.09 mol% was measured. The $CO_2$ concentration increases further with the current density. At 0.21 $A\,cm^{-2}$ (0.455 V), a concentration of 1.09 mol% $CO_2$ was measured in the anode effluent.

Consequently, based on the gas analysis of the effluent it is obvious that the electrochemical oxidation of CO takes place only if the EWGSR is operated within

the third regime of the polarisation curve. At low current densities only the direct electrochemical $H_2$ oxidation takes place.

The shape of the polarisation curve (figure 4.13) and the start of the CO oxidation in the third regime ($i > 0.17$ A cm$^{-2}$) is related to the CO adsorption and CO electro-oxidation characteristics. Carbon monoxide is a known Pt catalyst poison, as it strongly adsorbs on the active surface sites of the catalyst and, thus, reduces the amount of available active sites for the $H_2$ oxidation [67, 68]. The electrochemical oxidation of CO with $H_2O$ depends upon the respective anode overpotential. The dissociative chemisorption of $H_2O$ (equation 3.4) requires a certain electrode overpotential to occur [71, 72, 130, 134].
The observed intense increase of the polarisation curve slope in the transition regime ($i = 0.08$ - $0.17$ A cm$^{-2}$) is most likely caused by the absence of a sufficient amount of free anodic active surface sites for the faradaically controlled $H_2$ oxidation reaction, as CO occupies a large portion of catalyst sites by adsorption.
Consequently, the anode overvoltage rises significantly with increasing cell current as the available anodic active surface sites become the limiting factor for $H_2$ oxidation. This occurred likely approx. at $i = 0.08$ A cm$^{-2}$ (figure 4.13), being the start of a more pronounced anode polarisation.
The beginning of the electrochemical CO oxidation can be identified in figure 4.13 not only by the gas analysis, but also by the more moderate cell voltage increase during the current density step from 0.16 to 0.17 A cm$^{-2}$.
In the high current regime ($i > 0.16$ A cm$^{-2}$), no indications of significant mass transport limitations of the occurring reactions are visible in figure 4.13.

**Influence of the CO and $H_2$ gas concentration**

The influence of the anode feed gas CO concentration on the EWGSR voltage is shown in figure 4.14a. Polarisation curves, recorded at 393 K for three different CO concentrations (12.5, 25 and 50 mol%) and 50 mol% $H_2$, are shown.
All three curves exhibit the above described three characteristic regimes. However, it is clearly visible that a higher CO feed gas concentration shifts the transition regime to lower current densities. For a CO concentration of 50 mol%, a pronounced anode polarisation is observed already at about $i = 0.05$ A cm$^{-2}$, compared to a value of $i = 0.09$ A cm$^{-2}$ with 25 mol% CO and 12.5 mol% CO. However, the voltage increase was observed to be flatter at 12.5 mol% CO than at 25 mol% CO and 50 mol% CO.

For all three applied CO concentrations, the end of the transition regime was observed at a cell voltage of about 0.410 V. Here, the operation points at $i = 0.09$ A cm$^{-2}$ (0.427 V), $i = 0.12$ A cm$^{-2}$ (0.405 V) and $i = 0.17$ A cm$^{-2}$ (0.411 V) for an

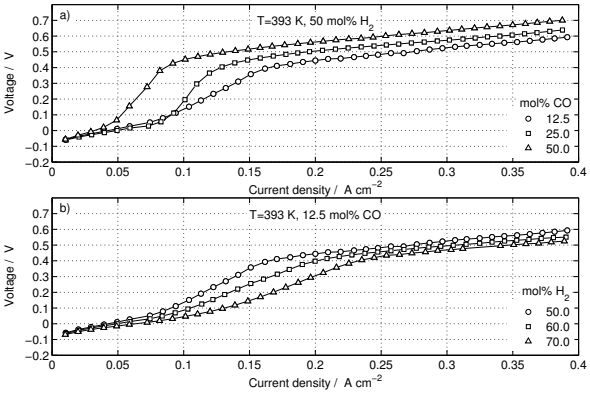


**Figure 4.14.:** Polarisation curve dependency upon selected operation parameters and otherwise unchanged operation conditions: a) influence of the anode feed gas CO concentration, recorded at $T = 393\,K$ with 50 mol% $H_2$ (related to the dry anode feed stream), b) influence of the anode feed gas $H_2$ concentration, recorded at $T = 393\,K$ with 12.5 mol% CO (related to the dry anode feed stream).

operation with 50 mol% CO, 25 mol% CO and 12.5 mol% CO, respectively, can be identified as starting points of the electrochemical CO oxidation by examining the first derivative of the polarisation curve. Hence, the value of the anode overvoltage at the start of the electrochemical CO oxidation seems to be nearly independent on the CO concentration of the anode feed gas.
However, the electrochemical CO oxidation shifts with respect to the current density, as the transition regime of the EWGSR polarisation curve is shifted to lower current densities at increasing CO feed gas concentrations. At current densities with proceeding CO electro-oxidation, all three polarisation curves in figure 4.14a have a similar slope of about 0.075 V per 0.1 $A\,cm^{-2}$.

The influence of the $H_2$ feed gas concentration upon the EWGSR operation is shown in figure 4.14b. The experiments were conducted for 12.5 mol% CO and $H_2$ feed gas concentrations of 50, 60 and 70 mol% at 393 K.
In the low current density range ($i = 0.01$ - $0.08\ A\,cm^{-2}$), the $H_2$ feed gas concentration was found to influence the voltage to some extent. A lower $H_2$ feed gas concentration led to a stronger voltage rise. The concentration gradient dependent voltage between the electrodes (see Nernst equation) is directly influenced by a change of the anode $H_2$ feed gas concentration. During the recording of the polarisation curves in figure 4.14b, the cathodic $H_2$ concentration was equal at equal currents. The $H_2$ concentration gradient between the anode and cathode compart-

ments increased with the increase of the anode $H_2$ feed gas concentration, and therefore increases the nominal value of the concentration dependent potential difference between the electrodes. Thus, the polarisation curves recorded with higher $H_2$ concentrations exhibit lower cell voltages within the low current density range. The polarisation curve slope changed at approx $i = 0.08$ A cm$^{-2}$, $i = 0.10$ A cm$^{-2}$ and $i = 0.12$ A cm$^{-2}$ for the curves recorded with 50 mol%, 60 mol% and 70 mol% $H_2$, respectively. Consequently, the beginning of the transition regime is shifted to higher current densities with higher $H_2$ anode feed gas concentrations. A higher $H_2$ feed gas concentration results in a CO oxidation starting at higher current densities.
However, the *cell voltage* at which the CO oxidation starts was found to be approx. 0.411 V - 0.420 V for all three $H_2$ concentrations. This coincides well with the values found during the experiments with different CO feed gas concentrations (see figure 4.14a. All three polarisation curves depicted in figure 4.14b show, for $U_{cell} > 0.420$ V, the same characteristic linear dependency of the cell voltage upon the applied current density as the curves in figure 4.13 and 4.14a.

**Influence of Temperature**

The influence of the operation temperature upon the EWGSR current-voltage characteristics is shown in figure 4.15a. The anode feed gas composition was 50 mol% $H_2$, 12.5 mol% CO balanced by $N_2$.
Under these conditions, lower cell voltages were generally observed at higher temperature. At low current densities, the temperature did not influence the polarisation curve significantly (see figure 4.15a). However, the position of the transition regime changed remarkably with changing temperature. For the polarisation curve recorded at 393 K, the strong anode polarisation started already below $i = 0.1$ A cm$^{-2}$, whereas 403 K and 413 K led to transition regimes with lower voltage slopes at $i > 0.1$ A cm$^{-2}$.

At 403 K and 413 K, no clear beginning of the transition regime is visible. The temperature dependency of the EWGSR polarisation curve is likely connected to the CO surface coverage of the anode catalyst, which increases the anode polarisation by limiting the amount of surface sites active for the $H_2$ oxidation.
In this context one should remember, that the fraction of Pt catalyst active sites covered by CO, therefore being unavailable for the $H_2$ oxidation, increases with decreasing operation temperature. This is caused by the negative free Gibbs adsorption energy of CO, which decreases with decreasing temperatures [87].
An experimental validation of this dependency was carried out by e.g. Pitois et al. and Davies et al. for Pt and PtRu containing LT-PEMFC electrodes, respectively

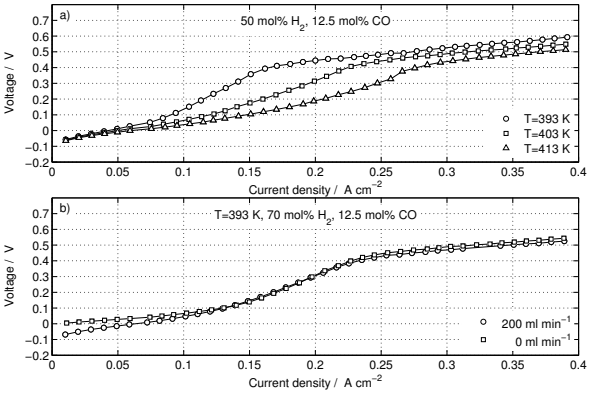


**Figure 4.15.:** Polarisation curve dependency upon selected operation parameters and otherwise unchanged operation conditions: a) influence of the operation temperature, recorded with 50 mol% $H_2$ and 12.5 mol% CO (related to the dry anode feed stream), b) influence of the cathode purge $N_2$ flow rate, recorded at $T = 393\,K$ with 50 mol% $H_2$ and 12.5 mol% CO (related to the dry anode feed stream).

[142, 143]. Furthermore, the results of the $H_2$ free EWGSR study (chapter 4.2) support the findings of this CO adsorption temperature dependency under EWGSR conditions, where lower cell voltages for the CO oxidation at lower temperatures were observed.

Consequently, it can be stated that an increased operation temperature lowers the amount of CO adsorbed on the catalyst surface and, hence, increases the catalyst surface available for the $H_2$ oxidation. Therefore, at 413 K the transition regime was shifted to a higher current densities, compared to the curves recorded at 393 K and 404 K (figure 4.15a).

Based on the results presented in figure 4.13, the CO oxidation at 393 K, 403 K and 413 K (figure 4.15a) is assumed to start at approx $i = 0.17\ A\,cm^{-2}$, $i = 0.24\ A\,cm^{-2}$ and $i = 0.28\ A\,cm^{-2}$, respectively. The corresponding cell voltages of 0.411 V (393 K), 0.425 V (403 K) and 0.398 V (413 K) are in the same range as observed under variation of the CO feed concentration, which indicates that the onset of the CO oxidation does not significantly change with respect to the voltage within the applied temperature and educt concentration range.

**Influence of Cathodic Purging**

A cathodic purge flow rate of 200 $\mathrm{ml\,min^{-1}}$ $N_2$ was applied during most of the experiments. However, a purge flow is not desired when one aims to generate pure, concentrated $H_2$. Therefore, experiments without the cathodic purge flow were conducted to observe the influence of the cathodic $N_2$ flow upon the EWGSR voltage. A comparison of two EWGSR polarisation curves, recorded with (200 $\mathrm{ml\,min^{-1}}$) and without (0 $\mathrm{ml\,min^{-1}}$) cathode purging, is shown in figure 4.15b. These polarisation curves were recorded at 393 K with an anode feed gas composition of 70 mol% $H_2$ and 12.5 mol% CO.
The curves are closely identical, deviating only at low current densities. Here, the curve recorded with cathode purging exhibits negative cell voltages and a stronger voltage increase in the current density interval from 0.01 $\mathrm{A\,cm^{-2}}$ to 0.12 $\mathrm{A\,cm^{-2}}$ than the curve recorded without cathode purging.
The positive cell voltages at low current densities during the EWGSR operation without cathode purging originate from the reversed concentration gradient between anode and cathode, as the cathode compartment is completely flooded with $H_2$.
The comparison of the two polarisation curves in figure 4.15b shows that the cathode purging only influences the EWGSR voltage at $i < 0.12$ $\mathrm{A\,cm^{-2}}$.

**CO Conversion**

Figure 4.16 displays current-voltage values obtained at 393 K and 403 K with an anode feed gas containing 10 mol% CO and 50 mol% $H_2$, as well as the determined corresponding $CO_2$ flow rates in the anode effluent. A proceeding CO oxidation ($CO_2$ within the effluent) was proven at 393 K and 403 K for the current range $i \geq 0.28$ $\mathrm{A\,cm^{-2}}$ and $i \geq 0.39$ $\mathrm{A\,cm^{-2}}$, respectively.

Similar to the results shown in figure 4.15a, higher voltages were measured at 393 K than at 403 K for $i > 0.1$ $\mathrm{A\,cm^{-2}}$. The $CO_2$ molar flow rate in the effluent was zero for both temperatures at current densities below $i = 0.17$ $\mathrm{A\,cm^{-2}}$. At a current density of 0.28 $\mathrm{A\,cm^{-2}}$ and a temperature of 393 K, the $CO_2$ molar flow rate ($G_{CO_2}$) was $8.5 \cdot 10^{-8}$ $\mathrm{mol\,s^{-1}\,cm^{-2}}$, whereas at 403 K no $CO_2$ was detected. The increase of the current density to 0.39 $\mathrm{A\,cm^{-2}}$ led to $G_{CO_2} = 1.76 \cdot 10^{-7}$ $\mathrm{mol\,s^{-1}\,cm^{-2}}$ at 393 K and $G_{CO_2} = 1.25 \cdot 10^{-7}$ $\mathrm{mol\,s^{-1}\,cm^{-2}}$ at 403 K.
It is visible, that the lowest current density, where the generation of $CO_2$ was experimentally observed, was temperature dependent (figure 4.16). This finding agrees well with the previous conclusion regarding the shift of the transition regime. For example, at 403 K and $i = 0.28$ $\mathrm{A\,cm^{-2}}$, the obtained voltage (0.373 V) did not

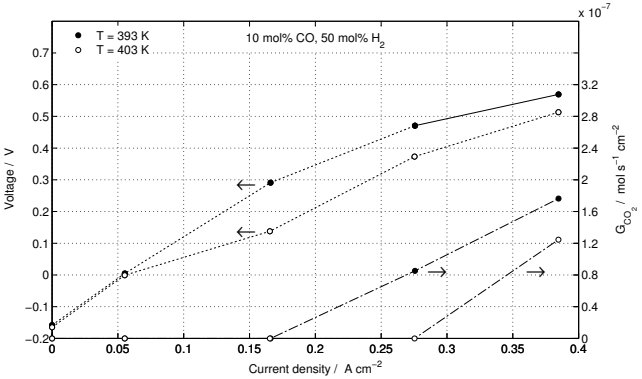


**Figure 4.16.:** Anodic $CO_2$ evolution rates in combination with the corresponding EWGSR voltages, obtained at $T = 393\,K$, $T = 403\,K$ and different current densities with 50 mol% $H_2$ and 12.5 mol% CO (related to the dry anode feed stream).

exceed 0.4 V and no $CO_2$ was detected, whereas at 393 K a voltage of about 0.471 V was measured and a significant $CO_2$ generation in the anode was detected.
The obtained $CO_2$ molar flow rate can be directly correlated to the reaction rate of the proceeding electrochemical CO oxidation. The $CO_2$ flow rate is lower at the higher temperature. Therefore, at $i = 0.39\ A\,cm^{-2}$ the fraction of $H_2$ being oxidised, and thus contributing to the current, is larger at 403 K than at 393 K.
The rate of chemical reactions is typically a function of the concentration of the participating species and their molar ratio. Therefore, the amount of water, added to the dry anode feed gas, likely influences the EWGSR operation. The influence of water was investigated by changing the $H_2O/CO$ ratio from 4.01 to 6.06 (see table 4.2).

Figure 4.17 shows that the lowest current density with $CO_2$ detection, as well as the determined $CO_2$ effluent flow rate values, was not significantly influenced by the $H_2O/CO$ ratio. The current voltage curve recorded at a $H_2O/CO$ ratio of 4.01 exhibits only slightly higher voltages than that recorded at a $H_2O/CO$ ratio of 6.06. The EWGSR voltage was 0.536 V and 0.514 V at $i = 0.28\ A\,cm^{-2}$ with the $H_2O/CO$ ratios of 4.01 and 6.06, respectively.
During the operation at $i = 0.28\ A\,cm^{-2}$, $CO_2$ flow rates of $G_{CO_2} = 9.40 \cdot 10^{-8}$ and $G_{CO_2} = 9.84 \cdot 10^{-8}$ in $mol\,s^{-1}\,cm^{-2}$ were obtained with $H_2O/CO$ ratios of 4.01 and 6.06, respectively. The minor deviation of these values indicates that the CO oxidation rate did not change significantly as a function of the $H_2O/CO$ ratio. To

understand the voltage change due to different feed gas water content, the following considerations can be made.

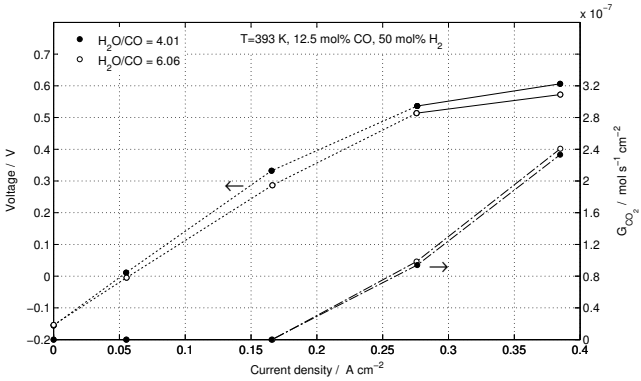


**Figure 4.17.:** Anodic $CO_2$ evolution rates combined with the corresponding EWGSR voltages, obtained two different anode feed gas $H_2O/CO$ ratios, versus the current density.

First, the higher EWGSR voltage with a $H_2O/CO$ ratio of 4.01 might indicate an increase of the anode overvoltage, resulting from an influence of the lower $H_2O$ content upon the reaction kinetics. A change of the anode overvoltage would influence both the $H_2$ oxidation and the CO oxidation.
As the $H_2$ oxidation does not depend upon $H_2O$ as educt, the assumed higher anode overvoltage with the $H_2O/CO$ ratio of 4.01 would result in a higher $H_2$ oxidation rate. This in turn implies that the actual CO oxidation rate decreases, as the total number of transferred electrons is constant at a constant current. The experimental results in figure 4.17 show a lower $G_{CO_2}$ at $i = 0.28\ \mathrm{A\,cm^{-2}}$ and $i = 0.39\ \mathrm{A\,cm^{-2}}$ when the feed gas water content was lower. This observation supports the assumption of a higher anode overvoltage at lower $H_2O/CO$ ratios. But, the deviation of $G_{CO_2}$ due to the different anode feed gas water content is negligible when considering the accuracy of GC measurements.
Secondly, the deviating EWGSR voltage with different anode feed gas water content might be related to changes in the membrane conductivity. Asensio et al. [104] showed that a higher water content in the feed gas influences the conductivity of ABPBI based polymer electrolytes positively. Consequently, the here observed higher voltages with the lower $H_2O/CO$ ratio could also be caused by a slightly decreased membrane conductivity.

The dependence of the CO oxidation rate on the CO feed gas concentration and the corresponding current voltage dependency is shown in figure 4.18.

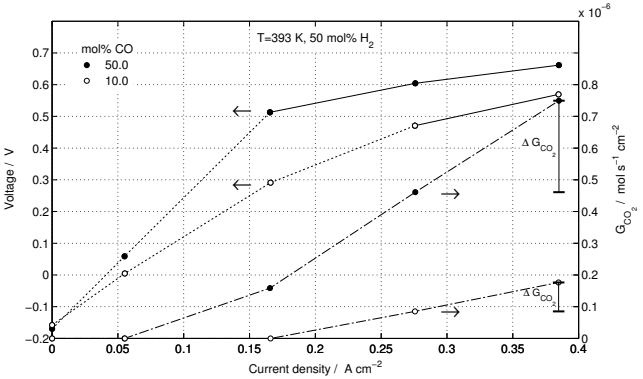


**Figure 4.18.:** Anodic $CO_2$ evolution rates combined with the corresponding EWGSR voltages, obtained at two different CO feed concentrations, versus the current density.

The obtained current voltage dependencies coincide well with the results shown in figure 4.14a. The CO feed gas concentration of 50 mol% led to a more pronounced increase of the EWGSR voltage (anode polarisation) until the first $CO_2$ detection in the anode effluent, if compared to 10 mol% CO. Furthermore, for all applied current densities the recorded voltages were higher for 50 mol% CO than for 10 mol% CO. With 50 mol% CO, the current voltage curve exceeded 0.4 V at $i = 0.17$ A cm$^{-2}$, which was found previously to be approximately the starting voltage of the CO oxidation within the used EWGSR setup.

The flow rate of $CO_2$, $G_{CO_2} = 1.59 \cdot 10^{-7}$ mol s$^{-1}$ cm$^{-2}$, was determined for $i = 0.17$ A cm$^{-2}$ and 50 mol% CO, whereas no $CO_2$ was detected with 10 mol% CO at this current, likely due to the relatively low voltage of 0.29 V. The higher current density of $i = 0.28$ A cm$^{-2}$ led to a $CO_2$ detection also for the 10 mol% CO operation.

The difference of the $CO_2$ flow rate $\Delta G_{CO_2}$ between two current densities, indicated in figure 4.18, reveals that the CO oxidation rate increased stronger for 50 mol% CO ($\Delta G_{CO_2} = 2.83 \cdot 10^{-7}$ mol s$^{-1}$ cm$^{-2}$) than for 10 mol% CO ($\Delta G_{CO_2} = 0.93 \cdot 10^{-7}$ mol s$^{-1}$ cm$^{-2}$). The respective $\Delta G_{CO_2}$ values were calculated for the current range of $i = 0.28$ - $0.38$ A cm$^{-2}$.

Using the Faraday law, the determined $\Delta G_{CO_2}$ values can be compared directly to the imposed increase of the total current density ($\Delta i = 0.11$ A cm$^{-2}$). Calculated from the amount of $CO_2$, it can be seen that the CO oxidation ($\Delta i_{CO,ox} = 0.055$ A cm$^{-2}$) contributed about 50 % to the overall current increase, whereas the rest can be assigned to the hydrogen oxidation. On the other hand, at 10 mol% CO the CO oxidation rate rise contributed only about 16.4 % ($\Delta i_{CO,ox} = 0.018$ A cm$^{-2}$) to the

current rise, whereas the $H_2$ oxidation provided the major fraction ($\Delta i_{H_2,ox} = 0.092$ A cm$^{-2}$).
In the considered current density interval ($i = 0.28$-$0.38$ A cm$^{-2}$), the current voltage curves for both CO concentrations exhibit a closely similar voltage slope. Hence, the current density increase from 0.28 A cm$^{-2}$ to 0.38 A cm$^{-2}$ most likely did not cause a higher anode polarisation for 50 mol% CO than for 10 mol% CO, which therefore might be excluded as reason for the observed stronger CO oxidation rate increase.
For this reason, one might conclude that a higher CO coverage of the anode catalyst surface, being a function of the CO gas concentration, caused the more pronounced increase of the CO oxidation rate at the higher CO concentration.

**Anode Effluent $H_2$/CO ratio**

As many electrochemical processes, the proceeding reactions within the EWGSR might be subject to transport limitations. Diffusion resistances can limit the maximal employable current density, as a current density overload leads under such conditions to critical electrode overvoltages which could damage the MEA components irreversible. Therefore, preferably the anode effluent should contain always a certain amount of the educt compounds $H_2$ and CO, which are at best utilised in a subsequent process.
Many chemical processes utilise syngas (CO and $H_2$ mixtures) for the synthesis of organic compounds [14, 18, 19, 144]. Here, the $H_2$/CO ratio is of crucial importance, depending upon the respective process. For instance, the process units of large scale processes such as ammonia synthesis, methanol synthesis or Fischer-Tropsch synthesis are designed to operate with hydrogen rich reformat gas streams with molar $H_2$/CO ratios of about 4.5, 2.1 and 2.0, respectively [144].
The CO oxidation rate dependence on the operation conditions of the EWGSR (as seen in figures 4.16-4.18) grants an option to control the anode effluent composition, while extracting simultaneously neat $H_2$ as the cathode effluent. The precise adjustment of the molar $H_2$/CO ratio in the anode effluent could be highly advantageous for an efficient and sustainable application of the EWGSR process in large scale processes.
Figure 4.19 displays the molar $H_2$/CO ratio in the anode effluent as a function of the applied current density for the anode feed gas CO concentrations of 10.0 mol%, 12.5 mol%, 25.0 mol% and 50.0 mol%. The anode feed gas contained furthermore 50 mol% $H_2$ and the measurements were conducted at 393 K or 403 K.
Focusing first on the operation at 393 K, the molar $H_2$/CO ratios were found to decrease for all investigated CO concentrations up to the current density of $i = 0.17$ A cm$^{-2}$. At this current, $H_2$/CO ratios of 3.65, 2.93, 1.53 and 0.85 were deter-

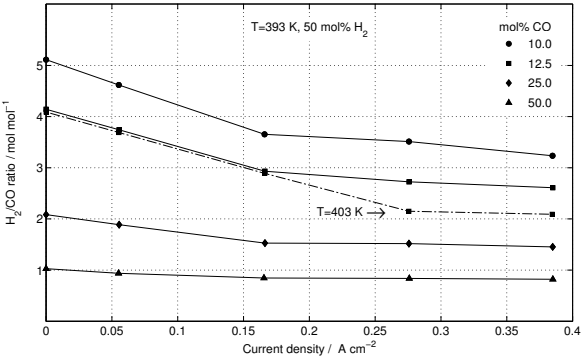


**Figure 4.19.:** Variation of the anode effluent $H_2/CO$ ratio in dependence upon anode feed gas CO concentration and current density, obtained at $T = 393\,K$ or $T = 403\,K$.

mined for the CO anode feed gas concentrations of 10.0 mol%, 12.5 mol%, 25.0 mol% and 50.0 mol%, respectively. At higher current densities the decrease of the molar $H_2/CO$ ratio, associated to the anode feed gas CO concentrations of 10.0 mol% and 12.5 mol%, is moderate, and the molar $H_2/CO$ ratio associated to 25.0 mol% CO and 50.0 mol% CO remains practically constant at $i > 0.17\ A\,cm^{-2}$.

This implies that for a higher CO content, the ratio of the $H_2$ oxidation to the CO oxidation is almost constant in this current range. The observed molar $H_2/CO$ ratio decrease in the low current interval ($i = 0$-$0.17\ A\,cm^{-2}$) is suggested to result from the consumption of hydrogen via $H_2$ oxidation, while no CO oxidation occurs. At $i > 0.17\ A\,cm^{-2}$, the EWGSR voltage exceeded 0.4 V, and the CO oxidation proceeded in parallel to the $H_2$ oxidation. This holds for the operation at 393 K.

Figure 4.19 contains also the obtained anode effluent molar $H_2/CO$ ratios of the experiment with 12.5 mol% CO at 403 K. As shown in figure 4.16, the CO oxidation was detected only at the current density of $i = 0.39\ A\,cm^{-2}$. This is reflected by the dependency of the $H_2/CO$ ratio upon the current density, as the mole ratio decreases linearly until $i = 0.28\ A\,cm^{-2}$ to a value of 2.15. At $i = 0.39\ A\,cm^{-2}$, only a minor further decrease of the molar $H_2/CO$ ratio to 2.09 was determined.

### CO Current Fraction

The interdependency of the electrochemical CO and $H_2$ oxidation influences the EWGSR voltage and the anode effluent molar $H_2/CO$ ratio.

In order to describe these changes in a coherent manner, the ratio of the current density, generated by CO oxidation ($i_{CO,ox}$), to the total current density ($i_{tot}$) was

defined as CO current fraction ($\beta_{CO}$) of the EWGSR process. The definition of $\beta_{CO}$ is described by equation 4.7.

$$\beta_{CO} = \frac{i_{CO,ox}}{i_{tot}} = \frac{G_{CO_2} \cdot z \cdot F}{i_{tot}} \tag{4.7}$$

Here, $G_{CO_2}$ represents the molar $CO_2$ effluent flow rate, $z$ stands for the number of exchanged electrons per generated $CO_2$ molecule, an $F$ is the Faraday constant. The dependency of $\beta_{CO}$ upon the applied current density and the CO feed gas concentration is displayed for two temperatures (393 K and 403 K) as a three-dimensional surface plot in figure 4.20. The numeric values of all labelled data points in figure 4.20 are summarised in Table 4.3 and the points are linearly connected.

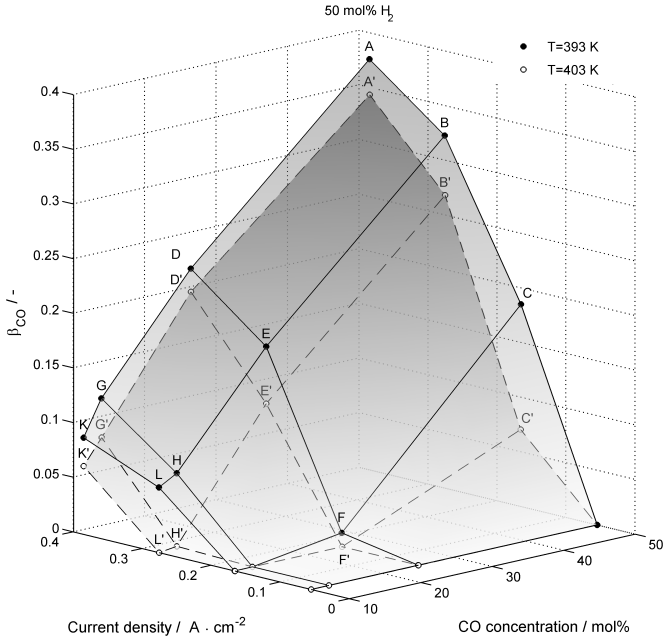


**Figure 4.20.:** The CO current fraction of the EWGSR process $\beta_{CO}$ as function of current density and anode CO feed gas concentration, obtained at T = 393 K and T = 403 K with 50 mol% $H_2$ (related to the dry anode feed stream). The surface areas and lines in-between the labelled data points originate from linear interpolation.

The influence of the operation temperature upon the CO current fraction at different CO concentrations is visible at best at a current density of 0.17 $A\,cm^{-2}$. Here,

$\beta_{CO}$ is zero for 10.0 and 12.5 mol% CO at both temperatures. A further increase of the CO concentration to 25.0 mol% initiated the CO oxidation at 393 K, resulting in $\beta_{CO} = 0.001$ (point F), whereas $\beta_{CO}$ remained zero at 403 K (point F'). At T = 393 K and 50.0 mol% CO (point C), the CO oxidation contributed 18.5% of the total current, whereas at 403 K (point C') only 7.0% of the total current were generated by CO oxidation.
It is clearly visible that the maximal CO current fractions of 0.376 and 0.343 were achieved at the highest CO concentration (50 mol%) and the highest current density (0.39 $A\,cm^{-2}$), at 393 K and 403 K, respectively. The contribution of the CO oxidation to the total current decreased along with the CO concentration and the current density for both temperatures.

The observed dependency of $\beta_{CO}$ upon the CO concentration can be evaluated by introducing the maximal possible faradaic current density ($i_{tot}^{max}$) into equation 4.7. The overall maximal current density $i_{tot}^{max}$ is now defined as the maximal current available from the complete conversion of CO along with the complete transfer of all anodic $H_2$ to the cathode.
Consequently, $\beta_{CO}^{i^{max}}$ is now theoretically calculated from the anode feed gas composition according to equation 4.8.

$$\beta_{CO}^{i^{max}} = \frac{i_{CO,ox}^{max}}{i_{tot}^{max}} = \frac{G_{CO} \cdot 2 \cdot F}{(G_{H_2} + G_{CO}) \cdot 2 \cdot F} \tag{4.8}$$

The values of $\beta_{CO}^{i^{max}}$ at all applied CO concentrations are listed in Table 4.3. The experimentally obtained $\beta_{CO}$ values did not exceed the $\beta_{CO}^{i^{max}}$ of the respective CO concentration.

However, CO current fractions larger than $\beta_{CO}^{i^{max}}$ could be theoretically possible with anode feed gases containing $H_2$ and CO, if the operation conditions lead to a preferred CO oxidation compared to the $H_2$ oxidation.
This case might appear for a EWGSR operation at temperatures significantly below 393 K, as this supports the preferential CO adsorption at the anode catalyst, and, thus, minimises the adsorption of $H_2$ onto the active catalyst surface sites. Furthermore, a low molar $H_2$/CO ratio in the anode feed gas is assumed to favour a preferred CO adsorption. The required overall current density highly depends upon the respective inlet $H_2$ and CO molar flow rates, whereas low current densities are assumed to be beneficial to achieve $\beta_{CO} > \beta_{CO}^{i^{max}}$.
During the experiments, the measured $\beta_{CO}$ was higher for 393 K than for 403 K at every current density and CO concentration. This supports the above suggested

| data point | $c_{CO,dry}$ / mol% | i / A cm$^{-2}$ | $\beta_{CO}^{393\,K}$ / - | $\beta_{CO}^{403\,K}$ / - | $\beta_{CO}^{i^{max}}$ / - |
|---|---|---|---|---|---|
| A | 50.0 | 0.39 | 0.376 | 0.343 | 0.50 |
| B | 50.0 | 0.28 | 0.322 | 0.268 | 0.50 |
| C | 50.0 | 0.17 | 0.185 | 0.070 | 0.50 |
| D | 25.0 | 0.39 | 0.221 | 0.120 | $0.3\bar{3}$ |
| E | 25.0 | 0.28 | 0.166 | 0.114 | $0.3\bar{3}$ |
| F | 25.0 | 0.17 | 0.001 | 0 | $0.3\bar{3}$ |
| G | 12.5 | 0.39 | 0.121 | 0.085 | 0.20 |
| H | 12.5 | 0.28 | 0.069 | 0.002 | 0.20 |
| K | 10.0 | 0.39 | 0.089 | 0.062 | $0.1\bar{6}$ |
| L | 10.0 | 0.28 | 0.059 | 0 | $0.1\bar{6}$ |

**Table 4.3.:** Summary of experimentally obtained and theoretically calculated CO current fractions, $\beta_{CO}^{393\,K}$,$\beta_{CO}^{403\,K}$ and $\beta_{CO}^{i^{max}}$, respectively, related to the respective CO concentrations and current densities (see figure 4.20).

possibility to reach $\beta_{CO} > \beta_{CO}^{i^{max}}$, as it demonstrates that lower temperatures shift the balance between CO oxidation and $H_2$ oxidation into the direction of CO oxidation.

As a summary, it may be concluded that the current fraction $\beta_{CO}$ obtained from CO oxidation is controllable via the current density, the feed gas composition or the operation temperature.

### Power Demand

The energy expenses of chemical processes are an important measure regarding the evaluation of operation costs and process sustainability. As the EWGSR is operated with electrical energy, the electrical power consumption is an important evaluation criterion.
Therefore, the molar energy consumption $\Phi_{H_2}$ is defined here as characteristic energetic parameter describing the ratio of the electrical power consumption per amount of generated cathodic hydrogen (see equation 4.9).

$$\Phi_{H_2} = \frac{U \cdot i}{G_{H_2,cath}} = \frac{P_{el}}{G_{H_2,cath}} \tag{4.9}$$

The molar energy consumption $\Phi_{H_2}$ as a function of the current density is shown in figure 4.21 for the operation with 10.0 and 50.0 mol% CO at 393 K and 403 K. Figure 4.21 displays clearly that the energy consumption of the EWGSR decreases if operated with low CO feed gas concentration.
For instance, at $i = 0.17$ A cm$^{-2}$ and 393 K, $\Phi_{H_2}$ was determined for the anode CO

feed gas concentration of 10.0 and 50.0 mol% to be 56.6 kJ mol$^{-1}$ and 98.5 kJ mol$^{-1}$, respectively. This energy consumption decrease due to lower CO concentrations is also visible at higher current densities. With $i = 0.39$ A cm$^{-2}$ at 393 K, $\Phi_{H_2}$ values of 109.9 kJ mol$^{-1}$ and 127.7 kJ mol$^{-1}$ were obtained for 10 and 50 mol% CO, respectively.

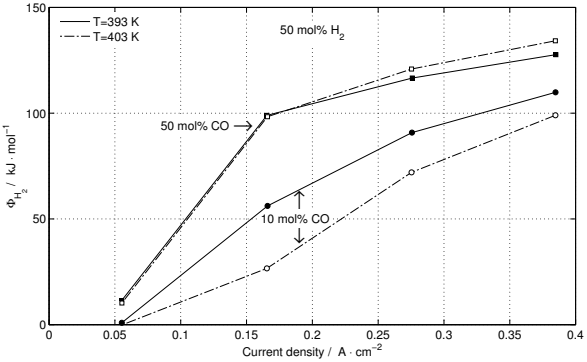


**Figure 4.21.:** The EWGSR energy consumption per mol cathodic $H_2$ as a function of the current density, obtained at T = 393 K or T = 403 K with 50 mol% $H_2$ and 10 mol% CO or 50 mol% CO (related to the dry anode feed stream).

The increase of the operation temperature to 403 K resulted at higher current densities in a reversed behaviour of $\Phi_{H_2}$. Due to the temperature increase of 10 K, $\Phi_{H_2}$ increased for 50.0 mol% CO by $\Delta\Phi_{H_2} = 4.3$ kJ mol$^{-1}$ and $\Delta\Phi_{H_2} = 6.6$ kJ mol$^{-1}$, at current densities of 0.28 A cm$^{-2}$ and 0.39 A cm$^{-2}$, respectively. In contrast, the same temperature increase resulted with 10.0 mol% CO in a decrease of $\Phi_{H_2}$ by $\Delta\Phi_{H_2} =$ -18.8 kJ mol$^{-1}$ and $\Delta\Phi_{H_2} =$ -10.9 kJ mol$^{-1}$, respectively.

The temperature dependence of $\Phi_{H_2}$ at 10.0 mol% CO might be explained by a reduction of the CO surface coverage due to the temperature increase [87, 142, 143]. A lower anode overvoltage directly lowers the electrical energy consumption of the EWGSR, as can be seen in figure 4.21.

On the other hand, the observed temperature dependence of $\Phi_{H_2}$ at 50.0 mol% CO does not follow this rule. The higher specific energy consumption at the higher temperature originates from higher voltages at the considered operation points. This type of temperature dependence of the EWGSR voltage was already observed in the $H_2$ free EWGSR study (chapter 4.2). In this previously discussed study the higher voltages at higher temperatures were suggested to result from the lower CO

surface coverage, which directly influence the anode reaction kinetics of the CO oxidation.

**Conclusions**

The results of the just presented EWGSR study with $H_2$ and CO containing feed gas can be summarised in the following points:

1. In the EWGSR process two driven anodic electrochemical reactions, being (i) the electrochemical $H_2$ oxidation and (ii) the electrochemical CO oxidation occur.
2. It was shown that the occurrence of the electrochemical CO oxidation depends strongly on the cell voltage. The influence of various operation parameters (e.g. temperature, CO and $H_2$ feed concentration, cathode purge flow rate) was investigated in detail.
3. It was clearly seen that the transition regime within the EWGSR polarisation curve and the CO oxidation shift along the current density axis in dependence on temperature, CO and $H_2$ feed concentration .
4. The EWGSR concept enables the precise adjustment of $H_2$/CO ratio in the anode effluent gas according to requirements of subsequent processes (e.g. methanol synthesis), by using the temperature and the current density as control parameters.
5. The ratio of the electrical current driving the CO oxidation to the total flowing electrical current was analysed. It was shown that low temperatures, high CO feed gas concentrations and high current densities increase the contribution of the CO oxidation to the EWGSRs total electrical current consumption.

# Chapter 5

# Exergy-based Comparison of the EWGSR to Alternative Processes

Within this chapter the EWGSR concept is evaluated with respect to other reformate based $H_2$ generation process routes. The development state of the EWGSR concept differs significantly from the established process routes. Therefore, a meaningful comparison requires the employment of a common reference measure which can be applied regardless of technical maturity. The concept of exergy was selected within this work to provide this required reference (see chapter 5.1). The comparative process evaluation of the EWGSR to state-of-the-art and novel $H_2$ generation processes aims to identify the concept's potential to evolve into a technically feasible and economically attractive alternative.
In the following, the applied process evaluation methodology is introduced (chapter 5.1) and applied to selected $H_2$ generation processes. Here, the pressure swing adsorption process (PSA, chapter 5.2.1) and the membrane separation process (MemSep, chapter 5.2.2) were selected to represent state-of-the-art $H_2$ generation routes. On the other hand, the cyclic water gas shift reactor (CWGSR, chapter 5.2.3) and the electrochemical water gas shift reactor (EWGSR, chapter 5.3) represent novel reformate based $H_2$ generation processes, which are still in the research and development state. The exergy analysis of the PSA, MemSep, and CWGSR processes was based on data available from literature, whereas the exergy analysis of the EWGSR was carried out with experimental data (chapter 4.3). The results of the exergy analysis are discussed and compared in chapter 5.4.

## 5.1 Exergy Analysis Methodology

Every comparative evaluation of technical processes requires a defined reference measure, which enables a reliable comparison between different technological approaches. Commonly, either an energy efficiency evaluation is carried out or cost per product factors are determined to elucidate the feasibility of a process in com-

parison to alternatives.

The selection of a suitable reference measure which is applicable for the comparison of the EWGSR process with established processes is not straightforward. The process delivers two product gas streams, neat $H_2$ at the cathode and a conditioned synthesis gas mixtures at the anode, which both can be utilised chemically or energetically. Neat hydrogen is an important chemical feed stock of various processes (e.g. ammonia synthesis, hydrogenations) [14, 144], as well as a promising future energy carrier [121, 131, 132]. Synthesis gas ($H_2$ + CO) is utilised to synthesise hydrocarbons and oxygenates (e.g. Fischer-Tropsch synthesis, methanol synthesis) [17–19], or used as fuel in e.g. molten carbonate fuel cells and solid oxide fuel cells [56, 58, 145].

The composition of the conditioned synthesis gas, the amount of generated neat $H_2$ and the energy demand of the EWGSR process highly depend upon the operation conditions, and hence, upon the overall process design in which the EWGSR might be integrated. Consequently, the definition of an overall reference measure, which refers to both energetic and product-related properties of the EWGSR, would be very specific and difficult to apply to other $H_2$ generating processes.

Therefore, the concept of exergy, originating from thermodynamics and being often applied in energy engineering, was selected as a tool to evaluate the feasibility of the EWGSR process in comparison to established neat $H_2$ generating process routes. The exergy of a substance or mixture expresses its work potential or the *quality of energy* with respect to a reference state. The circumstance, that the exergy concept captures the influence of a species concentration upon the total exergy of a mixture is advantageous for the evaluation of separation and purification processes.

In general, the exergy of a system comprises four contributions which are the potential, kinetic, physical, and chemical exergy. Systems without potential, kinetic and physical exergy are considered to be in the state of the defined environment, and systems which do not even exhibit chemical exergy are referred to be in dead state. Both the potential and kinetic exergy of a system, defined by its position and velocity within a fixed reference frame, respectively, have only minor relevance within the steady state operation of a process system. Therefore, these two exergy contributions were neglected within the here conducted exergy analysis. Hence, the total exergy of a species or mixture comprises of the physical and chemical exergy according to equation 5.1,

$$\epsilon_i = \epsilon_{i,phys} + \epsilon_{i,chem} \tag{5.1}$$

where $\epsilon_i$, $\epsilon_{i,phys}$ and $\epsilon_{i,chem}$ constitute the total exergy, the physical exergy, and the chemical exergy of the species or mixture i. A detailed presentation of the principles and application of the exergy analysis can be found in the literature [146–

148]. The calculation approach of the physical and chemical exergy is introduced in the chapters 5.1.1 and 5.1.2, along with illustrative examples in chapter 5.1.3. Furthermore, the exergy efficiency definition, as applied within this work, is given in chapter 5.1.4. Finally, numerical values of parameters (e.g. temperature, pressure, gas compositions, etc.) used within the executed exergy analysis are presented in chapter 5.1.5.

### 5.1.1. Physical Exergy

The physical exergy of a system represents the maximum obtainable work during the transition of the system from its initial state to a defined *environmental state*. The environmental state is constant and equal for every system included into the exergy analysis. It is usually defined by the real environmental conditions of the considered processes and described by the reference temperature $T^\circ$ and reference pressure $p^\circ$. Within this work the environmental state was defined to be $T^\circ = 298.15$ K and $p^\circ = 101325$ Pa.
In order to calculate the physical exergy of a system, the system borders are considered to be open for the transfer of energy and work, but impermeable for matter (closed system). Furthermore, all occurring transfer processes are considered to be ideally reversible and ideal gas conditions are assumed. An energy balance of the considered system leads to equation 5.2, which expresses the reversible work $w_{rev}$ performed by, or performed with, the system as a function of the transferred reversible heat $q_{rev}$ and the enthalpy change $\Delta h$ in the system. The second law of thermodynamics delivers the relation of the transferred reversible heat to the entropy change $\Delta s$ in the system as function of the temperature $T$ (equation 5.3).

$$w_{ref} = \Delta h - q_{rev} \tag{5.2}$$

$$q_{ref} = T \cdot \Delta s \tag{5.3}$$

$$\Delta\epsilon_{phys} = w_{ref} = \Delta h - T \cdot \Delta s \tag{5.4}$$

$$\epsilon_{phys,1} = (h_1 - h_0) - T^\circ \cdot (s_1 - s_0) \tag{5.5}$$

Consequently, the physical exergy of a system, being the maximal obtainable reversible work during the system equilibration with the environmental state, is obtained with equation 5.5. Here, $\epsilon_{phys,1}$, $h_1$ and $s_1$ refer to the physical exergy, the enthalpy and the entropy under initial state conditions, respectively, while $h_0$ and $s_0$ represent the enthalpy and entropy under environmental conditions.
The exergy analysis of a process requires usually the calculation of the exergy difference between two states aside the defined environmental state. This physical

exergy difference $\Delta\epsilon_{phys,12}$ between state one and state two is calculated according to equation 5.6.

$$\Delta\epsilon_{phys,12} = \epsilon_{phys,1} - \epsilon_{phys,2} = \Delta h|_{12} - T^{\circ} \cdot \Delta s|_{12}$$
$$\Delta\epsilon_{phys,12} = (h_1 - h_2) - T^{\circ} \cdot (s_1 - s_2) \tag{5.6}$$

Here, $\Delta h|_{12}$ and $\Delta s|_{12}$ represent the change of the enthalpy and entropy between state 1 and state 2, respectively. Please note that the enthalpy and entropy of the environmental state are eliminated by the subtraction, when calculating $\Delta\epsilon_{phys,12}$. The $H_2$ generation process routes (see chapter 5.2.1-5.2.3), as well as the EWGSR process proposed in this work, operate with gas mixtures. The enthalpy and entropy changes of gas mixtures can be obtained by calculating the specific change of the molar enthalpy, $\Delta\tilde{h}_{mix,12}(T)$, and the molar entropy, $\Delta\tilde{s}_{mix,12}(T,p)$, of the gas mixture. In the following, all mol specific quantities are identified with the symbol "˜". The enthalpy and entropy of ideal gas mixtures comprise of the entropy and enthalpy sum of all gas components, weighted by the mol fractions $x_i$, respectively. Consequently, the changes of molar enthalpy $\Delta\tilde{h}_{i,12}(T)$ and molar entropy $\Delta\tilde{s}_{i,12}(T)$ of each single gas component $i$ are used to calculate the change of the molar entropy and molar enthalpy of a considered gas mixture (equation 5.7 and 5.8).

$$\Delta\tilde{h}_{mix,12}(T) = \sum_i x_i \cdot \Delta\tilde{h}_{i,12}(T) \tag{5.7}$$

$$\Delta\tilde{s}_{mix,12}(T,p) = \sum_i x_i \cdot \Delta\tilde{s}_{i,12}(T,p) \tag{5.8}$$

The mole-fractions of gas mixtures are assumed to be constant during the change of the physical exergy. The calculation of $\Delta\tilde{h}_{i,12}(T)$ and $\Delta\tilde{s}_{i,12}(T)$ was carried out in this work with the help of empirical equations distributed by the *National Institute of Standards and Technology, USA* (NIST), and will be briefly presented in the following.

At first, the equations to calculate the change of the molar enthalpy $\Delta\tilde{h}_{mix,12}(T)$ between the states 1 and 2 are introduced. As given in equation 5.9, $\Delta\tilde{h}_{i,12}(T)$ is obtained by determining the enthalpy differences of the two states to the environmental state and a subsequent subtraction of both differences from each other. The enthalpy difference of a compound, due to a temperature different from $T^{\circ} = 298.15\,\mathrm{K}$, can be calculated with equation 5.10:

$$\Delta\tilde{h}_{i,12}(T) = \Delta\tilde{h}_{i,1}(T_1) - \Delta\tilde{h}_{i,2}(T_2) = (\tilde{h}_{i,T_1} - \tilde{h}_{i,298.15K}) - (\tilde{h}_{i,T_2} - \tilde{h}_{i,298.15K}) \tag{5.9}$$

$$\tilde{h}_T - \tilde{h}_{298.15\,K} = A \cdot t + B \cdot \frac{t^2}{2} + C \cdot \frac{t^3}{3} + D \cdot \frac{t^4}{4} - \frac{E}{t} + F - H, \tag{5.10}$$

where, $t$ is the temperature parameter ($t = {}^{T}/_{1000\,K}$). The coefficients $A - H$ were taken from the *NIST Chemistry Webbook*[149], and are called NIST coefficients within this work. The NIST coefficients are compound specific, differ in different temperature ranges, and are listed in table A.1(appendix chapter A) for the considered conditions in this work.

Unlike the enthalpy change of a species, which depends under ideal gas conditions upon the change of temperature only, entropy change is a function of temperature and pressure change. The differential species entropy $d\tilde{s}_i(T,p)$ is in equation 5.11 and originates from the second law of thermodynamics. Here, $\tilde{c}_{p,i}$ and $\tilde{v}_i$ represent the molar heat capacity and the molar volume of the species i, whereas $d\tilde{s}_i|_{p=const.}$ and $d\tilde{s}_i|_{p\neq const.}$ illustrate the proportions of $d\tilde{s}_i(T,p)$ which are unaffected and affected by pressure variation, respectively.

$$d\tilde{s}_i = \frac{\tilde{c}_{p,i}}{T}dT - \frac{\tilde{v}_i}{T}dp = d\tilde{s}_i|_{p=const.} - d\tilde{s}_i|_{p\neq const.} \tag{5.11}$$

$$\Delta\tilde{s}_i = \Delta\tilde{s}_i|_{p=const.} - \Delta\tilde{s}_i|_{p\neq const.} \tag{5.12}$$

$$\Delta\tilde{s}_i|_{p=const.} = \int_{0K}^{T} \frac{\tilde{c}_{p,i}}{T}dT = A\cdot ln(t) + B\cdot t + C\cdot\frac{t^2}{2} + D\cdot\frac{t^3}{3} - \frac{E}{2\cdot t^2} + G \tag{5.13}$$

$$\Delta\tilde{s}_i|_{p\neq const.} = \int_{p^\circ}^{p} \frac{\tilde{v}_i}{T}dp = R\cdot ln\left(\frac{p}{p^\circ}\right) \tag{5.14}$$

The total change of a species entropy $\Delta\tilde{s}_i$ is calculated from equation 5.12, whereas the determination of $\Delta\tilde{s}_i|_{p=const.}$ and $\Delta\tilde{s}_i|_{p\neq const.}$ is done via the equations 5.13 and 5.14. Here, equation 5.13 is supplied by [149], as well as the values of the NIST coefficients $A - G$ (see table A.1). It is valid for the standard pressure ($p^\circ = 101325$ Pa) and the temperature parameter $t = {}^{T}/_{1000\,K}$. Equation 5.14 was derived by applying the ideal gas law and contains the universal gas constant $R$.

### 5.1.2. Chemical Exergy

In accordance to the theory of physical exergy, chemical exergy denotes the maximum obtainable work during a state transition. In contrast to the physical exergy, the considered initial and end state of the transition necessary for the determination of the chemical exergy are well defined and do not depend upon process conditions. Both states depend upon the nature of the considered chemical compound or species.

The temperature and pressure of the initial state are defined to be similar to the environmental state conditions ($T^\circ = 298.15$ K and $p^\circ = 101325$ Pa) and equal for ev-

ery chemical compound. However, the initial state concentration of the considered compounds remains a variable. The end state of the chemical transition is called *ground state*, and is defined separately for every chemical element. This ground state definition is based upon the element's state in the natural environment and represents its most probable form of appearance within the natural environment. Furthermore, an element's ground state is mostly characterised by a high chemical stability of the respective element. For example, atmospheric $CO_2$ is the defined reference ground state of carbon, as it constitutes complete oxidised carbon (i.e. high chemical stability). Additionally, the ground state of an element involves the thermodynamic activity (activity coefficient times concentration measure) of the element under ground state conditions. For instance, the atmospheric concentration of $CO_2$ is considered to be the reference concentration within the ground state definition of $CO_2$, as atmospheric $CO_2$ is thermodynamically equilibrated with the environment. Consequently, a compound concentration deviating from its ground state value contributes to the total chemical exergy of the compound, as it represents a driving force for an equilibration process.
The molar chemical exergy of a single compound is a constant value and its calculation is well documented [146, 148]. The standard chemical exergies employed within this work are presented for all required compounds in table 5.1.

| compound i | | standard chem. exergy $\tilde{\epsilon}^{\circ}_{chem}$ / J mol$^{-1}$ |
|---|---|---|
| $CH_4$ | (g) | 836510 |
| CO | (g) | 275430 |
| $H_2$ | (g) | 238490 |
| $CO_2$ | (g) | 20140 |
| $H_2O$ | (g) | 11710 |
| $H_2O$ | (l) | 3120 |
| $N_2$ | (g) | 720 |

**Table 5.1.:** Standard chemical exergies $\tilde{\epsilon}^{\circ}_{chem}$ at $T^{\circ}$=298 K, $p^{\circ}$=101325 Pa, [146].

The chemical exergy of a mixture of compounds comprises of the standard chemical exergies of the present compounds $\tilde{\epsilon}^{\circ}_{i,chem}$, weighted by the respective concentration measure. Various gas mixtures were considered within this work and their respective chemical exergies were calculated according to equation 5.15.

$$\tilde{\epsilon}_{mix,chem} = \sum_i x_i \cdot \tilde{\epsilon}^{\circ}_{i,chem} + R \cdot T^{\circ} \cdot \sum_i x_i \cdot ln x_i \tag{5.15}$$

Here, the mole fractions $x_i$ of the compounds $i$ within the respective gas mixture were employed in the calculation of a gas mixture chemical exergy $\tilde{e}_{mix,chem}$, along with the universal gas constant $R$ and the environmental reference temperature $T^{\circ}$.

### 5.1.3. Implementation of the Exergy Concept

This section introduces the practical application of the exergy concept as conducted in this work. At first, the exergy balancing approach for a default separation unit is introduced, followed by heat exchanger balancing. Finally, the determination of the reaction heat based exergy is briefly introduced.

#### Balancing of a Separation Unit

The exergetic evaluation of the respective processes is carried out with respect to the generated pure $H_2$ stream (see chapter 5.1.4). Therefore, mass balances are applied to characterise the amount of produced neat $H_2$ stream (desired product). Besides the primary $H_2$ containing effluent stream, each separation process possesses a tail gas effluent stream (undesired product). The exergy within the tail gas is considered to be unusable as exergy source for subsequent process steps within a respective reference process chain. A more detailed discussion as to why the tail gas exergy was not considered (i.e. neglected) as usable exergy gain of the process can be found in chapter 5.1.4. The molar tail gas stream is indicated in the balance

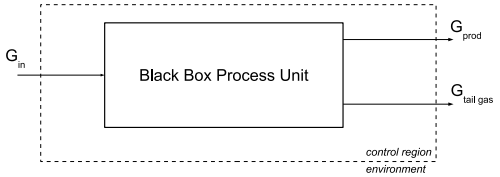


**Figure 5.1.:** Mass balance envelope of a default separation unit, with $G_{in}$ - molar inlet stream, $G_{prod}$ - desired product outlet stream, and $G_{tail\,gas}$ - tail gas outlet stream.

envelope schemes. Figure 5.1 shows a default separation process unit, including the exergy balance envelope and the molar effluent streams. Here, $G_{tail\,gas}$ represents the tail gas stream of the default separation unit.
The general steady state mass balance of the separation unit, shown in figure 5.1, can be expressed according to equation 5.16. Absolute numerical values of the indicated molar flow rates depend highly upon the scale of the respective separation unit. Therefore, the product to feed gas ratio $\chi$ (see equation 5.17) is often listed

within the literature to enable qualitative comparison between different sizes of separation units. The introduction of $\chi$ enables the determination of the product stream exergy with respect to the molar stream of employed educt gas.

$$\frac{dn}{dt} = 0 = G_{in} - G_{prod} - G_{tail\,gas} \tag{5.16}$$

$$\chi = \frac{G_{prod}}{G_{in}} \tag{5.17}$$

$$E_{prod} = \frac{G_{prod} \cdot (\tilde{\epsilon}^{prod}_{mix,chem} + \tilde{\epsilon}^{prod}_{phys})}{G_{in}} = \chi \cdot (\tilde{\epsilon}^{prod}_{mix,chem} + \tilde{\epsilon}^{prod}_{phys}) \tag{5.18}$$

This leads to the exergetic process parameter $E_{prod}$ with the unit $J/mol$, which describes the amount of exergy within the product with respect to the amount of employed educt gas (equation 5.18). In the case that the product gas comprises only $H_2$ and reference conditions are assumed, $\tilde{\epsilon}^{prod}_{mix,chem} = \tilde{\epsilon}^{\circ}_{H_2}$.

### Exergy Balance of a Standard Heat Exchanger

Figure 5.2 shows a default heat exchanger unit. The exergy exchange through a heat exchanger can be calculated based upon the physical exergies of the inlet and outlet streams, while assuming no material changes within the stream. The associated steady state exergy balance is presented in equation 5.19, where $G_{in}$, $G_{out}$, $\tilde{\epsilon}_{in}$, $\tilde{\epsilon}_{out}$, $\tilde{\epsilon}_q$, and $I$ represent the molar inlet stream, molar outlet stream, molar inlet exergy, molar outlet exergy, the transferred exergy via heat exchange, and the exergy transfer irreversibility losses, respectively.

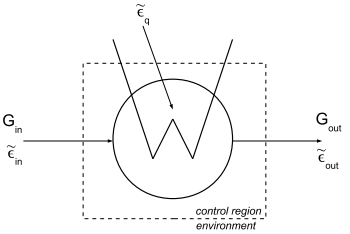


**Figure 5.2.:** Exergy balance envelope of a default heat exchanger, with $G_{in}$, $\tilde{\epsilon}_{in}$ - molar inlet stream and molar inlet exergy, $G_{out}$, $\tilde{\epsilon}_{in}$ - molar outlet stream and molar outlet exergy, and $\tilde{\epsilon}_q$ - molar exergy of transferred heat.

$$\frac{d\epsilon}{dt} = 0 = G_{in} \cdot \tilde{\epsilon}_{in} + G_{in} \cdot \tilde{\epsilon}_q - G_{out} \cdot \tilde{\epsilon}_{out} + I \quad \text{with} \quad G_{in} = G_{out},\ I = 0 \tag{5.19}$$

$$\tilde{\epsilon}_q = \tilde{\epsilon}_{out} - \tilde{\epsilon}_{in} \ \rightarrow \ \tilde{\epsilon}_q = \tilde{\epsilon}_{phys,out} - \tilde{\epsilon}_{phys,in} \quad \text{as} \quad \tilde{\epsilon}_{chem,in} = \tilde{\epsilon}_{chem,out} \tag{5.20}$$

The exergy irreversibility losses $I$ are assumed to be zero within this work, i.e. ideal reversible exergy transfer. This leads to equation 5.20, which defines the transferred heat exergy within a default heat exchanger. In the case that a heat exchanger is combined with a water separation (condensation unit), the recoverable heat exergy comprised of two components: (i) the fluid exergy transfer due to cooling to a temperature below the condensation temperature, and (ii) the fluid exergy transfer due to the release of the condensation enthalpy. The latter refers to the water content of the considered fluid.

**Exergy from Reaction Enthalpy Release**

The exergy content of heat $q$ depends upon the temperature level at which the considered heat is released. It is determined with the help of the Carnot efficiency, which describes the upper efficiency boundary of a thermodynamical cyclic process (e.g. Carnot cycle) converting heat into work. The Carnot efficiency depends upon the temperature of the heat transfer $T_q$ and the temperature of the material or environment assigned to uptake the heat. Within the framework of exergy, the latter temperature is the earlier introduced environmental temperature $T^\circ$. Consequently, the exergy of a given heat can be calculated according to equation 5.21.

$$\tilde{\epsilon}_q = \tilde{q} \cdot \eta_{Carnot} = \tilde{q} \cdot (1 - \frac{T^\circ}{T_q}) \tag{5.21}$$

$$\tilde{\epsilon}_{\Delta_R \tilde{h}} = \Delta_R \tilde{h} \cdot \eta_{Carnot} = \Delta_R \tilde{h} \cdot (1 - \frac{T^\circ}{T_R}) \tag{5.22}$$

Equation 5.21 can be applied to released reaction enthalpy within chemical reactors as shown in equation 5.22. Here, $\tilde{\epsilon}_{\Delta_R \tilde{h}}$ represents the exergy of the reaction enthalpy and the molar reaction enthalpy $\Delta_R \tilde{h}$ and the reaction temperature $T_R$ constitute the given heat $q$ and the heat transfer temperature $T_q$, respectively. The exergy related to the reaction enthalpy can be considered within the exergy analysis as option to replace necessary exergy inputs for fluid heating and thus lowers the overall process exergy demands.

### 5.1.4. Exergy Efficiency

In general, the efficiency of a process is defined as the ratio of the desired process gain to the necessary process effort and is often used to evaluate and compare pro-

cesses. Many different efficiency definitions, e. g. based upon energetic or economic process parameter, might be applied for process evaluation. An economic process assessment requires process data like operation costs, product market value or process build up costs. These information are hardly available for specific processes as a complete reliable data set, let alone for a group of processes. On the contrary, the exergy efficiency determination of a process requires energetic and material flow data, which are available via experiments or literature. An energetic process assessment based upon the exergy efficiency permits conclusions as to whether a process is energetically feasible and it enables conclusions about the energetic cost distributions, which influence the economic process assessment.

A sound efficiency definition requires the selection of a desired product, which is similar (i.e. comparable) for all included processes. In this work heat $H_2$ constitutes this desired product, whereas the side products vary depending upon the respective process characteristics. In principle, side products (e.g. tail gas of a separation unit) might represent a valuable energetic or material resource for subsequent processes. However, their actual value depends upon their actual utilisation within the overall process, which depends on the energetic and material integration level of the respective process.

As the energetic and material integration level is diverse for different process installations and respective data is rare; the here conducted theoretical process assessment employs the exergy efficiency definition, which relates the exergy of the generated neat $H_2$ (shared desired product) $E_{H_2,prod}$ (equation 5.24) to the educt-work exergy efforts $E_{ed.+w}$ (equation 5.25) and the net heat exergy efforts $E_{q,net}$ (equation 5.26). Here, $E_{ed.+w}$ is the sum of the educt exergy content and the required technical work. The definition of the exergy efficiency is given in equation 5.23.

$$\eta_{H_2} = \frac{E_{H_2,prod}}{E_{ed.+w} + E_q} \xrightarrow{\text{heat integr.}} \begin{array}{l} E_{q,net} < 0 \Rightarrow \eta^1_{H_2} = \dfrac{E_{H_2,prod}}{E_{ed.+w}} \\ E_{q,net} > 0 \Rightarrow \eta^2_{H_2} = \dfrac{E_{H_2,prod}}{E_{ed.+w} + E_{q,net}} \end{array} \tag{5.23}$$

In order to account for a possible heat integration which utilises generated heat within the process, the net heat exergy $E_{q,net}$ of the process can be calculated (equation 5.26) and incorporated into the exergy efficiency definition. If $E_{q,net} \leq 0$ (i.e. excess of process heat exergy) no heat exergy was added to exergy process efforts, whereas positive $E_{q,net}$ values (i.e. additional demand of process heat exergy) were added to the exergy efforts instead of $E_q$ (see equation 5.23). The respective status of $E_{q,net}$ is represented in the exergy efficiency symbol $\eta_{H_2}$ by adding 1 or 2 as superscript, indicating a surplus or a need of heat exergy in the overall process, respectively.

The experimental investigations of the EWGSR operation (chapter 4.2, 4.3) allowed for the calculation of the total exergy efficiency $\eta_{tot}$, which considers both reactor effluent streams ($H_2$ stream and tail gas) as desired process products (see equation 5.42, chapter 5.3). The total exergy efficiency definition does not account for heat integration. It is used within this work to rate the summarised energetic value of all process products and will be employed in the comparative process assessment (chapter 5.4) similar to the generally known energy efficiency.
Similar to $E_{H_2,prod}$ (equation 5.24), the exergy demand contributions $E_{ed.+w}$ and $E_{q,net}$ are defined with respect to the molar educt inlet stream $G_{in}$. The reformate gas inlet stream ($H_2$, CO containing gas mixture) constitutes this molar educt stream ($G_{in(reformate)} = G_{in}$) for all considered processes.

$$E_{H_2,prod} = (\tilde{\epsilon}^{\circ}_{H_2} + \tilde{\epsilon}_{H_2,phys}) \cdot \frac{G_{H_2,prod}}{G_{in(reformate)}} \quad ,$$
$$\text{if } T = T^{\circ} \quad \text{and} \quad p = p^{\circ} \quad \Rightarrow \quad E_{H_2,prod} = \tilde{\epsilon}^{\circ}_{H_2} \cdot \frac{G_{H_2,prod}}{G_{in(reformate)}} \tag{5.24}$$

$$E_{ed.+w} = \sum_i \tilde{\epsilon}_i \cdot \frac{G_{i,in}}{G_{in(reformate)}} + \sum_k \tilde{w}_{comp} \cdot \frac{G_k}{G_{in(reformate)}} + \frac{P_{el}}{G_{in(reformate)}} \tag{5.25}$$

$$E_{q,net} = \sum_n \frac{G_n}{G_{in(reformate)}} \cdot \tilde{\epsilon}_{q,n} + \frac{\Delta G^{WGSR}_{CO}}{G_{in(reformate)}} \cdot \tilde{\epsilon}_{\Delta_R \tilde{h}} \tag{5.26}$$

Consequently, $E_{ed.+w}$ represents the ratio of the educt-work exergy effort to the reformate inlet stream and $E_{q,net}$ is defined as the ratio of the net heat exergy of the process to the reformate inlet stream (equation 5.25 and 5.26). Within these equations, $i, k, n$ are the running variables for the considered species, compression- and heat exchange units, respectively. The above definitions ensure a consistent determination of the exergy efficiency, as $E_{H_2}$ is related to the molar reformate inlet stream (as discussed together with the separation unit balancing, chapter 5.1).
All process efforts, except of fluid heating, are summarised within $E_{ed.+w}$, which includes the necessary technical work for compression $\tilde{w}_{comp}$ and additional electrical power demand $P_{el}$. Within equation 5.26, $G_n$, $G_{in(reformate)}$ and $\Delta G^{WGSR}_{CO}$ represent the molar fluid flow through heat exchanger $n$, the molar reformate gas inlet flow rate of the process and the amount of consumed CO within the water gas shift reactor in $\mathrm{mol\,s^{-1}}$, respectively.

### 5.1.5. Parameters used for Exergy Analysis

This section briefly introduces process conditions and parameters, which were the basis for the conducted exergy analyses of $H_2$ generation processes. All parameters originate from literature and are listed for the PSA process, the MemSep process, and the CWGSR process, being discussed in the chapter 5.2.1, 5.2.2, and 5.2.3, respectively. The employed conditions and parameters of the EWGSR exergy analysis are listed in chapter 5.3.

| species mole fraction | inlet gas composition A | B | C |
|---|---|---|---|
| $x_{H_2}$ | 0.52 | 0.42 | 0.51 |
| $x_{CO}$ | 0.11 | 0.18 | 0.44 |
| $x_{CO_2}$ | 0.05 | 0.11 | 0.02 |
| $x_{H_2O}$ | 0.28 | 0.29 | 0.03 |
| $x_{CH_4}$ | 0.04 | 0 | 0 |
| $x_{N_2}$ | 0 | 0 | 0 |

**Table 5.2.:** Reformat gas compositions: A - steam reforming of natural gas, [14]; B - biomass gasification optimised for PSA process, [122]; biomass gasification optimised for CWGSR process, [122].

Table 5.2 presents three different reformate gas compositions. Composition A represents a common gas composition, obtainable from methane steam reforming, which is not explicitly optimised for a specific downstream purification method. In contrast to composition A, composition B and C are optimised compositions for subsequent $H_2$ purification processes and originate from a rigorous biomass gasification process model by Heidebrecht et al. [122]. That work proposed gas compositions B and C to be optimal for the utilisation in a PSA process and CWGSR process, respectively.

| operation parameter | HT-WGSR | operation conditions PSA | MemSep. | CWGSR |
|---|---|---|---|---|
| T / K | 723 | 298 | 723 | 1073 |
| p / Pa | $20{\cdot}10^5$ | $16{\cdot}10^5$ | prod. tail<br>$1.01{\cdot}10^5$ \| $6{\cdot}10^5$ | $1.01{\cdot}10^5$ |

**Table 5.3.:** Employed reactor operation conditions: HT-WGSR - high temperature water gas shift reactor, [14]; PSA - pressure swing adsorption unit,[14]; MemSep - membrane separation unit,[150]; CWGSR - cyclic water gas shift reactor, [122].

The HT-WGSR unit within the analysed PSA and MemSep process increases the $H_2$ yield via the water gas shift reaction. The operation conditions of the HT-WGSR unit, as well as of the PSA unit, the MemSep unit, and the CWGSR unit, are listed in table 5.3, as used in the exergy analysis. The employed reactor effluent compositions are summarised in table 5.4. Here, for the PSA and MemSep process only the compositions of the $H_2$ containing effluents are listed.

| species mole fraction | outlet gas composition | | | | | |
|---|---|---|---|---|---|---|
| | HT-WGSR wet | HT-WGSR dry | PSA | MemSep. | CWGSR product | CWGSR tail |
| $x_{H_2}$ | 0.58 | 0.75 | 0.9990 | 1 | 0.57 | 0.17 |
| $x_{CO}$ | 0.04 | 0.05 | 0 | 0 | 0 | 0.13 |
| $x_{CO_2}$ | 0.12 | 0.15 | 0 | 0 | 0 | 0.32 |
| $x_{H_2O}$ | 0.22 | 0 | 0 | 0 | 0.43 | 0.37 |
| $x_{CH_4}$ | 0.04 | 0.05 | 0.0001 | 0 | 0 | 0.01 |
| $x_{N_2}$ | 0 | 0 | 0.0009 | 0 | 0 | 0 |

**Table 5.4.:** Product gas compositions: HT-WGSR - high temperature water gas shift reactor, [14]; PSA - pressure swing adsorption unit,[14]; MemSep - membrane separation unit, [150]; CWGSR - cyclic water gas shift reactor, [122].

## 5.2 Exergy Analysis of Alternative Processes

This chapter discusses the conducted exergy analysis of $H_2$ generation processes, being alternatives to the EWGSR concept. Each process is introduced with the help of the applied process flow scheme and process conditions. Furthermore, process specific equations and made assumptions are discussed. The results of the analysis are summarised and discussed in combination with the EWGSR exergy analysis results in chapter 5.4.

### 5.2.1. Pressure Swing Adsorption Process

The pressure swing adsorption (PSA) technology represents the state-of-the-art to separate large amounts of $H_2$ from gas mixtures. Plant capacities of 100000 $m^3 \cdot h^{-1}$ $H_2$ are technically feasible and realised [14]. The separation principle is based upon the different adsorption characteristics of species in dependence upon the respective substrate. The PSA often utilises active carbon and 5A zeolite as adsorption agents, where highly volatile substances with a low polarity (e.g. $H_2$) show low adsorption affinities compared to polar species like $H_2O$, CO, $CO_2$, or hydrocarbons [14, 38]. A PSA process consists of minimal four adsorption columns which are operated in a cyclic manner by switching between the adsorption regime and the regeneration regime.

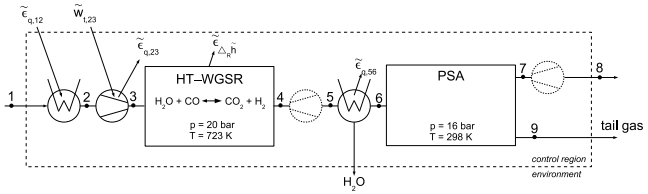


**Figure 5.3.:** Exergy balance envelope of the PSA process; 1 - educt inlet, 8 - final product outlet, $\tilde{e}_{q,12}$ - exergy of heat transfer, $\tilde{w}_{t,23}$ - technical compression work, $\tilde{e}_{q,23}$ - exergy of heat transfer, $\tilde{e}_{\Delta_R h}$ - exergy of reaction enthalpy, $\tilde{e}_{q,56}$ - exergy of heat transfer. The dotted expansion units are neglected within the exergy analysis.

Figure 5.3 shows the process flow scheme which was selected to describe a PSA-based $H_2$ plant. All considered exergy efforts are indicated, as well as numbered intermediate process stages required for the exergy analysis. The calculations were carried out for the feed compositions A and B (table 5.2). Composition C was excluded as it is optimised for the CWGSR process. The exergy of the molar flux

entering the process at stage 1 was calculated using equations 5.1, 5.5 and 5.15. At stage 1 the temperature and pressure were defined to be similar to the environmental conditions ($T^\circ = 298.15$ K, $p^\circ = 101325$ Pa, chapter 5.1.1). Table 5.5 summarises the assumed temperature and pressure conditions at all labelled process stages in figure 5.3. These values constitute an approximation of the real conditions. Necessary fluid decompression steps within the process, as indicated with dotted unit symbols in figure 5.3, were neglected within the performed exergy analysis.

| operation parameter | process stage number 1, 8 | 2 | 3 | 4 | 5 | 6 | 7 |
|---|---|---|---|---|---|---|---|
| T / K | 298 | 723 | 723 | 723 | 723 | 298 | 298 |
| p / Pa | $1.01{\cdot}10^5$ | $1.01{\cdot}10^5$ | $20{\cdot}10^5$ | $20{\cdot}10^5$ | $16{\cdot}10^5$ | $16{\cdot}10^5$ | $16{\cdot}10^5$ |

**Table 5.5.:** Fluid conditions at intermediate stages of the PSA process scheme.

The molar exergy of heat transfer $\tilde{\epsilon}_{q,12}$, required to increase the fluid temperature from $T_1$ to $T_2$ was determined for feed compositions A and B to be 20.17 kJ mol$^{-1}$ and 20.27 kJ mol$^{-1}$, respectively (equation 5.20). The technical work $\tilde{w}_{t,23}$, required to compress the fluid from ambient pressure to the pressure of the HT-WGSR unit, was calculated with equation 5.27, assuming an isothermal compression of the fluid. The subscripts 2 and 3 indicate the process stage assigned to the respective temperature and pressure variable. The isothermic compression work, determined to be $\tilde{w}_{t,23} = 17.93$ kJ mol$^{-1}$, is released as heat energy during the compression (ideal cooling) and considered within the analysis as $\tilde{\epsilon}_{q,23}$ according to equation 5.28.

$$\tilde{w}_{t,23} = R \cdot T_2 \cdot ln\left(\frac{p_2}{p_1}\right), \quad \text{with } T_2 = T_3 \tag{5.27}$$

$$\tilde{\epsilon}_{q,23} = -\tilde{w}_{t,23} \cdot \left(1 - \frac{T^\circ}{T_2}\right) \tag{5.28}$$

The reaction enthalpy of the water gas shift reaction at 723 K was determined to be $\Delta_R \tilde{h}^{723\,K}_{wgsr}$ = -40.47 kJ mol$^{-1}$. By considering the gas composition at the HT-WGSR inlet and outlet (table 5.2 and 5.4), the molar exergy of the reaction enthalpy $\tilde{\epsilon}_{\Delta_R \tilde{h}}$ was determined for the gas composition A and B to be -1.57 kJ mol$^{-1}$ and -3.21 kJ mol$^{-1}$, respectively. Gas composition B results, due to its higher CO content, in a higher molar exergy of the reaction enthalpy.

The temperature of the HT-WGSR effluent is with 723 K significantly higher than the operation temperature of the subsequent PSA unit (298 K). Furthermore, it contains a significant amount of $H_2O$. The cooling of the gas stream down to the PSA temperature, as well as the $H_2O$ removal, was assumed to take place in a com-

bined heat exchange/condensation unit. Here, the wet and dry effluent gas mixture of the HT-WGSR (see table 5.4) was considered to constitute the inlet (stage 5) and outlet (stage 6) composition, respectively. The respective molar exergy of heat transfer, resulting from the fluid cooling and $H_2O$ condensation, was calculated to be $\tilde{\epsilon}_{q,56} = -16.84\,\mathrm{kJ\,mol^{-1}}$.

The product to feed ratio parameter $\chi_{65}^{PSA}$ was applied to describe the reduction of the process fluid due to the $H_2O$ separation between stage 5 and 6 (equation 5.29). Under ideal gas conditions, volume flow rate data valid for standard conditions ($p = 101325$ Pa, $T = 273$ K) [14] can be used to determine $\chi_{65}^{PSA}$ as indicated in equation 5.29. Here, the process inlet fluid flow rate (stage 1) is considered to be equal to the fluid flow rate at stage 5, due to the equimolar conversion within the HT-WGSR. Alternatively, $\chi_{65}^{PSA}$ can be determined from the species mole fractions of the wet HT-WGSR effluent (table 5.4), which leads to the similar value.

$$\chi_{65}^{PSA} = \frac{G_6}{G_5}, \quad \text{if} \quad G_1 = G_5 \;\Rightarrow\; \chi_{65}^{PSA} = \frac{G_6}{G_1} = \frac{8180}{10450} = 0.78 \tag{5.29}$$

$$\chi_{76}^{PSA} = \frac{G_7}{G_6} = \frac{45}{100} = 0.45 \tag{5.30}$$

The separation of $H_2$ within the PSA unit (see figure 5.3) was described by the product to feed ratio $\chi_{76}^{PSA}$, which is defined by equation 5.30. Similar to $\chi_{65}^{PSA}$, volume flow rate data valid for standard conditions was employed to calculate the PSA product to feed ratio $\chi_{76}^{PSA}$. Here, the used volume flow rates differ in magnitude from the values employed to determine $\chi_{65}^{PSA}$, as both data sets refer to different $H_2$ plants [14].

$$\begin{aligned}
\eta_{\tilde{e},H_2}^{(1)} &= \frac{\tilde{\epsilon}_{H_2}^{\circ} \cdot \frac{G_{H_2,prod}}{G_{in(reformate)}}}{\tilde{\epsilon}_{in} \cdot \frac{G_1}{G_{in(reformate)}} + \tilde{w}_{t,12} \cdot \frac{G_1}{G_{in(reformate)}}}, \quad \text{if } G_{in(reformate)} = G_1 \\
\eta_{\tilde{e},H_2}^{(1)} &= \frac{\tilde{\epsilon}_{H_2}^{\circ} \cdot x_{H_2,7} \cdot \frac{G_7}{G_6} \cdot \frac{G_6}{G_1}}{\tilde{\epsilon}_{in} + \tilde{w}_{t,12}} = \frac{\tilde{\epsilon}_{H_2}^{\circ} \cdot x_{H_2,out} \cdot \chi_{76}^{PSA} \cdot \chi_{65}^{PSA}}{\tilde{\epsilon}_{in} + \tilde{w}_{t,12}}
\end{aligned} \tag{5.31}$$

The exergy efficiency $\eta_{H_2}$ of the PSA-based $H_2$ production process (figure 5.3), was determined based upon the approach introduced in chapter 5.1.4. Following equation 5.23, the ratio of the net heat exergy to the molar inlet stream of the process was determined with equation 5.26 to be $E_{q,net} = -8.78\,\mathrm{kJ\,mol^{-1}}$ and $E_{q,net} = -10.23\,\mathrm{kJ\,mol^{-1}}$ for gas compositions A and B, respectively. When ideal heat integration is assumed, the PSA process possesses clearly a surplus of heat exergy and no additional heat exergy input is required. According to equation 5.23, this led to the PSA process exergy efficiency $\eta_{H_2}^{(1)}$ (equation 5.31).

The obtained exergy efficiency value of the PSA-based $H_2$ plant is listed in table 5.10 and compared in chapter 5.4 with the other process routes.

### 5.2.2. Membrane Separation Process

The membrane separation is an efficient and economical method to separate gaseous compounds from each other. Its most common application is the separation of $N_2$ from air [150]. However, it is also successfully applied as purification method to generate neat $H_2$ from $H_2$ containing gas mixtures [151]. The process employs $H_2$ selective thin membranes and a pressure gradient as driving force of the separation [150]. The process temperature depends upon the applied membrane material. Polymer membranes are operated at about 523 K [151], whereas the more common Pd based membranes operate at about 773 K [151–153]. Current membrane separation processes achieve $H_2$ recovery degrees of 70% to 95% for feed gases containing $H_2$ in the range of 70% to 99%, respectively [152, 154].

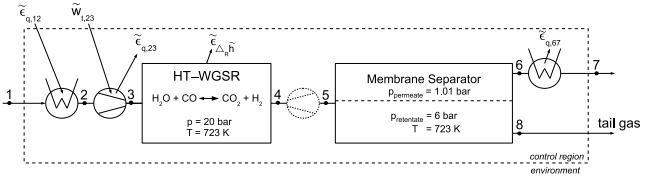


**Figure 5.4.:** Exergy balance envelope of the MemSep process; 1 - educt inlet, 8 - final product outlet, $\tilde{\epsilon}_{q,12}$ - exergy of heat transfer, $\tilde{w}_{t,23}$ - technical compression work, $\tilde{\epsilon}_{q,23}$ - exergy of heat transfer, $\tilde{\epsilon}_{\Delta_R h}$ - exergy of reaction enthalpy, $\tilde{\epsilon}_{q,67}$ - exergy of heat transfer. The dotted expansion units are neglected within the exergy analysis.

Figure 5.4 shows the considered arrangement of process units to describe a $H_2$ plant with a membrane separation (MemSep) unit. All considered exergy streams are indicated, as well as numbered intermediate process stages required for the exergy analysis. The calculations were carried out for the feed compositions A and B (table 5.2, composition C was excluded as it is optimised for the CWGSR process). Based upon the equations 5.1, 5.5 and 5.15, the exergy of the molar flux entering the process at stage 1 was calculated. Temperature and pressure at stage 1 were defined to be similar to the environmental conditions ($T^\circ = 298.15$ K, $p^\circ = 101325$ Pa, chapter 5.1.1).

Table 5.6 summarises the assumed temperature and pressure conditions at all labelled process stages (see figure 5.4). These values represent an approximation of the real conditions. The necessary fluid decompression step (stage 4 to stage 5),

along with the involved temperature decrease, was neglected within the exergy analysis.

| operation parameter | process stage number 1, 7 | 2 | 3 | 4 | 5 | 6 |
|---|---|---|---|---|---|---|
| T / K | 298 | 723 | 723 | 723 | 723 | 723 |
| p / Pa | $1.01{\cdot}10^5$ | $1.01{\cdot}10^5$ | $20{\cdot}10^5$ | $20{\cdot}10^5$ | $6{\cdot}10^5$ | $1.01{\cdot}10^5$ |

**Table 5.6.:** Fluid conditions at intermediate stages of the MemSep process scheme.

The molar exergy of heat transfer $\tilde{\epsilon}_{q,12}$, required to increase the fluid temperature from $T_1$ to $T_2$ was determined for feed compositions A and B to be 20.17 $\mathrm{kJ\,mol^{-1}}$ and 20.27 $\mathrm{kJ\,mol^{-1}}$, respectively (equation 5.20). The technical work $\tilde{w}_{t,23}$, required to compress the fluid from ambient pressure to the pressure of the HT-WGSR unit, was calculated with equation 5.27, assuming an isothermal compression of the fluid. The subscripts 2 and 3 indicate the process stage assigned to the respective temperature and pressure variable. The compression work, determined to be $\tilde{w}_{t,23} = 17.93$ $\mathrm{kJ\,mol^{-1}}$, is released as heat energy during the compression (ideal cooling) and considered within the analysis as $\tilde{\epsilon}_{q,23}$ according to equation 5.28. The calculations regarding the process stages 1 to 3 are similar to the PSA process.
The temperature of the HT-WGSR effluent is with 723 K similar to the assumed operation temperature of the subsequent MemSep unit. The operation of a MemSep unit is commonly characterised by the product related recovery index (RI). Here, RI is defined as the ratio of $H_2$ within the product stream $G_{H_2,product}$ to the $H_2$ in the feed stream $G_{H_2,feed}$ (see equation 5.32).

$$RI = \frac{G_{H_2,product}}{G_{H_2,feed}} = \frac{x_{H_2,6} \cdot G_6}{x_{H_2,5} \cdot G_5} \tag{5.32}$$

The $H_2$ recovery index of the MemSep unit was approximated based upon the results of Brunetti et al. [152]. Here, RI was determined experimentally for the $H_2$ concentrations of 44 mol% and 80 mol% to be RI = 0.6 and RI = 0.9, respectively. The employed outlet concentration of the HT-WGSR unit within this work is 58 mol% (wet outlet stream, table 5.4). The respective RI value was estimated with the help of a linear interpolation approach, using the experimental data of Brunetti et al, which resulted in equation 5.33:

$$RI(x_{H_2,in}) = 0.83 \cdot x_{H_2,in} + 0.23. \tag{5.33}$$

Considering the MemSep unit product stream, the molar exergy of heat transfer achievable between the stages 6 and 7 was determined to be $\tilde{\epsilon}_{q,67} = -1.98\ \mathrm{kJ\,mol^{-1}}$ (equation 5.20).
The resulting exergy efficiency $\eta_{H_2}$ of the MemSep unit employing $H_2$ plant (see figure 5.4) was calculated as shown in chapter 5.1.4. According to equation 5.23, the ratio of the net heat exergy to the molar inlet stream of the MemSep process was determined with equation 5.26 to be $E_{q,net} = 6.07\ \mathrm{kJ\,mol^{-1}}$ and $4.45\ \mathrm{kJ\,mol^{-1}}$ for gas compositions A and B, respectively. Consequently, following equation 5.23, external heat exergy input was considered in the determination of the MemSep process exergy efficiency $\eta^{(2)}_{H_2}$ (equation 5.34). Here, the MemSep process differs from the PSA process, for which a surplus of heat exergy was determined. This difference results from the missing $H_2O$ condensation unit in the MemSep process.

$$
\begin{aligned}
\eta^{(2)}_{\tilde{\epsilon},H_2} &= \frac{\tilde{\epsilon}^{\circ}_{H_2} \cdot \frac{G_{H_2,prod}}{G_{in(reformate)}}}{\tilde{\epsilon}_{in} \cdot \frac{G_1}{G_{in(reformate)}} + \tilde{w}_{t,12} \cdot \frac{G_1}{G_{in(reformate)}} + E_{q,net} \cdot \frac{G_{in(reformate)}}{G_{in(reformate)}}}, \\
&\text{if} \quad G_{in(reformate)} = G_1 = G_5 \quad \curvearrowright \\
\eta^{(2)}_{\tilde{\epsilon},H_2} &= \frac{\tilde{\epsilon}^{\circ}_{H_2} \cdot x_{H_2,6} \cdot \frac{G_6}{G_5}}{\tilde{\epsilon}_{in} + \tilde{w}_{t,12} + E_{q,net}}, \qquad \text{with} \quad \frac{G_6}{G_5} = RI \cdot \frac{x_{H_2,5}}{x_{H_2,6}} \quad \curvearrowright \\
\eta^{(2)}_{\tilde{\epsilon},H_2} &= \frac{\tilde{\epsilon}^{\circ}_{H_2} \cdot x_{H_2,5} \cdot RI}{\tilde{\epsilon}_{in} + \tilde{w}_{t,12} + E_{q,net}}
\end{aligned}
\tag{5.34}
$$

The determined exergy efficiency value of the MemSep $H_2$ plant is listed in table 5.10 and discussed in a comparative manner in chapter 5.4, along with all selected process routes.

### 5.2.3. Cyclic Water Gas Shift Reactor

The cyclic water gas shift reactor (CWGSR) is a novel reactor concept which is based on a fixed multi-bed system and represents a further development stage of the classical steam iron process [155]. Hydrogen and CO-rich reformate gas is utilised as educt to generate neat $H_2$ via reduction and re-oxidation cycles of iron oxide based materials. The net reaction is the water gas shift reaction. Due to its cyclic alternating operation, the generated $H_2$ is separated directly from the other gaseous reaction products within the reactor unit. The CWGSR operation conditions are listed in table 5.3 and further information are available within literature [126, 127, 156].

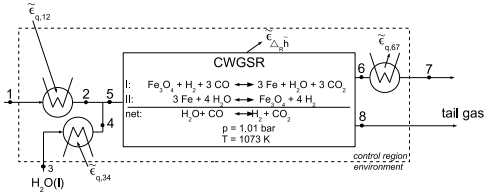


**Figure 5.5.:** Exergy balance envelope of the CWGSR process; 1 - reformate gas inlet, 3 - liquid water inlet, 8 - final product outlet, $\tilde{\epsilon}_{q,12}$ - exergy of heat transfer, $\tilde{\epsilon}_{q,34}$ - exergy of heat transfer ($H_2O$ steam generation), $\tilde{\epsilon}_{\Delta_R h}$ - exergy of reaction enthalpy, $\tilde{\epsilon}_{q,67}$ - exergy of heat transfer.

A $H_2$ plant, based on the CWGSR concept, is shown in figure 5.5. All considered exergy efforts are indicated, as well as numbered intermediate process stages required for the exergy analysis. The calculations were carried out for feed composition C (see table 5.2), which represents an optimised feed composition for the CWGSR process [122]. Based upon equations 5.1, 5.5 and 5.15, the exergy of the molar flux entering the process at stage 1 was calculated. Temperature and pressure at stages 1 and 3 were defined to be similar to the environmental conditions ($T^\circ = 298.15$ K, $p^\circ = 101325$ Pa, chapter 5.1.1). The educt mixture at stage 1 was considered to be in gaseous state, whereas at stage 3 liquid water was assumed.
Table 5.7 summarises the assumed temperature and pressure conditions at the labelled process stages (see figure 5.5). These values represent an approximation of the real conditions.

| operation parameters | process stage number 1, 7 | 2 | 3 | 4 | 5 | 6 |
|---|---|---|---|---|---|---|
| T / K | 298 | 1073 | 298 | 1073 | 1073 | 1073 |
| p / Pa | $1.01{\cdot}10^5$ | $1.01{\cdot}10^5$ | $1.01{\cdot}10^5$ | $1.01{\cdot}10^5$ | $1.01{\cdot}10^5$ | $1.01{\cdot}10^5$ |

**Table 5.7.:** Fluid conditions at intermediate stages of the CWGSR process scheme.

The required heat transfer exergy at stage 1-2 was determined to be $\tilde{\epsilon}_{q,12} = 12.52$ kJ mol$^{-1}$. The selected CWGSR process arrangement contains a second process feed stream: the addition of liquid $H_2O$. As introduced earlier, all process exergy efforts included into the process exergy efficiency calculation relate to the molar reformate feed stream (stage 1). Therefore, the exergy of heat transfer for the $H_2O$ stream production (stage 3-4) $\tilde{\epsilon}_{q,34}$ was first calculated (equation 5.35), and subsequently converted into the desired "exergy effort per mol reformatee feed gas" formulation

($\tilde{\epsilon}_{q,34}$) according to equation 5.36.

$$\tilde{\epsilon}_{q,34} = \tilde{\epsilon}_{phys,4} - \tilde{\epsilon}_{phys,3} \tag{5.35}$$

$$\tilde{\epsilon}_{q,34} = \tilde{\epsilon}_{q,34} \cdot \chi_{31}^{CWGSR}, \quad \text{with} \quad \chi_{31}^{CWGSR} = \frac{G_{3(H_2O)}}{G_1} \tag{5.36}$$

The numerical value of the water feed to reformate gas feed ratio $\chi_{31}^{CWGSR} = 1.1335$ was received from results of the model-based CWGSR operation optimisation published by Heidebrecht et al. [122].

The molar exergy of reaction enthalpy $\tilde{\epsilon}_{\Delta_R h}$, obtainable from the chemical reaction within the CWGSR, was calculated with the help of the reaction enthalpy of the water gas shift reaction at 1073 K ($\Delta_R \tilde{h}_{wgsr}^{1073\,K} = $-36.88 kJ mol$^{-1}$). Using equation 5.22, the $CO_2$ concentration of the CWGSR tail gas (table 5.4) and the assumption of equimolar reaction conditions during the reduction and re-oxidation phase during the CWGSR operation, $\tilde{\epsilon}_{\Delta_R h}$ was determined to be -8.59 kJ mol$^{-1}$, according to equation 5.37.

$$\tilde{\epsilon}_{\Delta_R h} = \Delta_R \tilde{h}_{wgsr}^{1073\,K} \cdot (1 - \frac{T^\circ}{T_{CWGSR}}) \cdot x_{CO_2,8} \cdot \frac{G_8}{G_1}, \quad \text{where} \quad G_8 = G_1 \tag{5.37}$$

Equation 5.37 assumes the equality of $G_8 = G_1$, which can be deduced from the equimolar reaction conditions and the cyclic operation regime of the reactor, as described in detail by Heidebrecht et al. [126, 127, 156].

The exergy efficiency $\eta_{H_2}$ of the CWGSR process (see figure 5.5) was determined according to chapter 5.1.4. The net heat exergy, with respect to the molar inlet stream $G_1$ (reformate gas), of the CWGSR process was calculated to be $E_{q,net} = 40.23$ kJ mol$^{-1}$ for gas composition C (equation 5.26). This significant net heat exergy demand of the CWGSR process originates mainly from the required educt temperature increase up to 1073 K. Consequently, the CWGSR exergy efficiency $\eta_{H_2}^{(2)}$ was

obtained according to equation 5.38.

$$
\begin{aligned}
\eta^{(2)}_{\tilde{e},H_2} &= \frac{\tilde{e}^{\circ}_{H_2} \cdot \frac{G_{H_2,prod}}{G_{in(reformate)}}}{\tilde{e}_{in,1} \cdot \frac{G_1}{G_{in(reformate)}} + \tilde{e}^{\circ}_{H_2O} \cdot \frac{G_{3(H_2O)}}{G_{in(reformate)}} + E_{q,net} \cdot \frac{G_{in(reformate)}}{G_{in(reformate)}}}, \\
\text{with} \quad & G_{in(reformate)} = G_1, \quad G_5 = G_1 + G_{3(H_2O)}, \quad G_7 = G_6, \\
& \chi^{CWGSR}_{65} = \frac{G_6}{G_5} \quad \curvearrowright \\
\eta^{(2)}_{\tilde{e},H_2} &= \frac{\tilde{e}^{\circ}_{H_2} \cdot x_{H_2,6} \cdot \chi^{CWGSR}_{65} \cdot (1 + \chi^{CWGSR}_{31})}{\tilde{e}_{in,1} + \tilde{e}^{\circ}_{H_2O} \cdot \chi^{CWGSR}_{31} + E_{q,net}}
\end{aligned}
\tag{5.38}
$$

The product stream to feed stream ratio $\chi^{CWGSR}_{65}$ of the CWGSR relates the $H_2$ containing effluent stream to the sum of both CWGSR educt streams. Its numerical value $\chi^{CWGSR}_{65}$= 0.5313 was also received from results of the model-based CWGSR operation optimisation published by Heidebrecht et al. [122]. A detailed derivation of equation 5.38 is presented within the Appendix B of this work.
The obtained exergy efficiency of the CWGSR process is listed in table 5.10 and evaluated in chapter 5.4, along with all selected process routes.

## 5.3 Exergy Analysis of the EWGSR Process

This section addresses the exergy analysis of the EWGSR process. In contrast to the PSA, MemSep, and CWGSR processes, the EWGSR exergy analysis was conducted using experimental data, being collected in the framework of the EWGSR investigations of this work. Unlike the above introduced definition of the exergy efficiency (see equation 5.23), the exergy efficiency of the EWGSR was determined without considering possible exergy gains from intermediate process heat sources (e.g. fluid cooling, reaction heat, etc.), as heat integration was not implemented into the experiment (see chapter 3). The process scheme of the considered EWGSR process is shown in figure 5.6. All included exergy efforts are indicated, as well as numbered intermediate process stages required for the exergy analysis.

Based upon figure 5.6, the exergy efficiency of the EWGSR $\eta^{\exp}_{H_2}$ was defined as the ratio of the exergy of the product $H_2$, $E_{H_2,prod}$ (stage 3, equation 5.40), to the exergy effort $E_{ed} + E_{q,12} + P_{el}$ (equation 5.39). Here, $E_{ed}$ is the sum of the chemical exergy and physical exergy content of the educts at stage 1 (equation 5.41). The exergy demands for the feed gas heat-up and $H_2O$ evaporation are summarised in $\tilde{e}_{q,12}$, which is multiplied with the molar inlet stream to determine $E_{q,12}$. All feed gas components and effluent components were considered to be in gaseous state at the

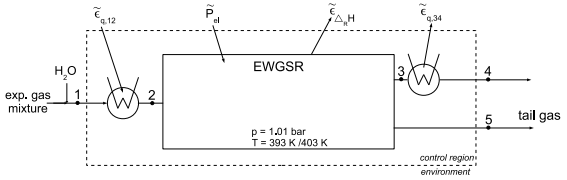


**Figure 5.6.:** Exergy balance envelope of the EWGSR process; 1 - reformate gas inlet, 2 - reactor inlet, 3 - reactor product outlet, 4 - $H_2$ product gas outlet, 5 - tail gas outlet, $P_{el}$ - electrical power input $\tilde{\epsilon}_{q,12}$ - exergy of heat transfer, $\tilde{\epsilon}_{q,34}$ - exergy of heat transfer, $\tilde{\epsilon}_{\Delta_R h}$ - exergy of reaction enthalpy.

| operation parameters | process stage number 1 | 2 | 3 | 4 | 5 |
|---|---|---|---|---|---|
| T / K | 298 | 393/403 | 393/403 | 298 | 298 |
| p / Pa | $1.01{\cdot}10^5$ | $1.01{\cdot}10^5$ | $1.01{\cdot}10^5$ | $1.01{\cdot}10^5$ | $1.01{\cdot}10^5$ |

**Table 5.8.:** Fluid conditions at intermediate stages of the EWGSR process scheme.

EWGSR inlet (stage 2). The electrical power demand $P_{el}$ of the EWGSR process is considered as exergy effort (equation 5.39).

$$\eta_{H_2}^{\exp} = \frac{E_{H_2,prod}}{E_{ed} + (G_{feed} \cdot \tilde{\epsilon}_{q,12}) + P_{el}} \quad \text{with} \tag{5.39}$$

$$E_{H_2,prod} = \tilde{\epsilon}^{\circ}_{H_2} \cdot G_{H_2,prod} \tag{5.40}$$

$$E_{ed} = \sum_i \left( (\tilde{\epsilon}^{\circ}_i + \tilde{\epsilon}_{i,phys}(T^{\circ}, p^{\circ})) \cdot G_{i,in} \right) \tag{5.41}$$

$$\eta_{tot}^{\exp} = \frac{E_{H_2,prod} + E_{tail}}{E_{ed} + P_{el}} \quad \text{with} \tag{5.42}$$

$$E_{tail} = \sum_i \left( \tilde{\epsilon}^{\circ}_i \cdot G_{i,tail} \right) \tag{5.43}$$

It was noted above, that the tail gas of a separation unit can contain a significant amount of usable exergy. A sustainable operation of the EWGSR within an overall process most likely necessitates the utilisation of the tail gas exergy. Therefore, the total exergy efficiency of the EWGSR process $\eta_{tot}$ is introduced. In contrast to $\eta_{H_2}^{\exp}$, the total exergy efficiency $\eta_{tot}^{\exp}$ considers also the tail gas exergy content $E_{tail}$ under

reference conditions (stage 4) as process gain (see equation 5.42). Consequently, $\eta_{tot}^{exp}$ reaches significantly higher values than $\eta_{H_2}^{exp}$, but does not include any information about the utilisation degree of the tail gas exergy content. Therefore, $\eta_{tot}^{exp}$ represents rather the upper boundary of the achievable total exergy efficiency under the applied conditions, than being a realistic value of the EWGSR application in an overall technical process. Hence, $\eta_{H_2}$ is better suited for process comparison purposes, as it is related to the desired process product $H_2$, only.
In chapter 5.3, the exergy efficiency results for the EWGSR operation with CO and $H_2$ containing anode feed gas are presented. These results were partly published by Oettel et al. [125].
Experimentally obtained exergy efficiencies of the EWGSR are listed in table 5.10 for selected operation conditions. The exergy efficiencies of all considered process variants are discussed in chapter 5.4.

## Operation with CO and $H_2$ Containing Anode Feed Gas

The exergy efficiency $\eta_{H_2}^{exp}$ of the EWGSR, operated with CO and $H_2$ containing feed gas (see table 4.2, chapter 3.3), was determined for steady state operation conditions. Within figure 5.7, all $\eta_{H_2}^{exp}$ values are summarised, which were calculated for the EWGSR operation at 393 K and $i > 0$ A cm$^{-2}$ with an anode feed gas $H_2$ content of 50 mol%. The respective $\eta_{H_2}^{exp}$ values, obtained at 403 K, were omitted in the diagram as they were found to be almost identical to the values obtained at 393 K. The temperature dependent change of the specific energy consumption $\Phi_{H_2}$ (see figure 4.21, chapter 4.3) was found to be not large enough to influence $\eta_{H_2}^{exp}$ significantly. The numerical values of the exergy efficiencies marked with letters in figure 5.7 are summarised in table 5.9.

Figure 5.7 displays $\eta_{H_2}^{exp}$ as a function of the applied current density and the CO feed gas concentration. It is clearly visible that $\eta_{H_2}^{exp}$ increases along the current density axis, but decreases along the CO feed gas concentration axis. For instance, at $i = 0.06$ A cm$^{-2}$ the exergy efficiency decreases from 0.063 at 10 mol% CO (point R) to 0.039 at 50 mol% CO (point D). These values constitute the lower end of the obtained $\eta_{H_2}^{exp}$, whereas the maximal values are found at $i = 0.39$ A cm$^{-2}$. Here, the overall $\eta_{H_2}^{exp}$ maximum was determined to be 0.368 at 10 mol% CO (point O), and $\eta_{H_2}^{exp} = 0.244$ (point A) was calculated at the same current density for 50 mol% CO. The low efficiency at high CO concentrations results from two reasons: (i) a higher CO feed gas concentration leads at given electric currents to a higher voltage, and thus to a higher electrical energy demand of the EWGSR (see figure 4.14a), and (ii) at constant electrical currents higher CO feed gas concentrations results in a larger amount of CO within the anode effluent, not being used as reduction agent

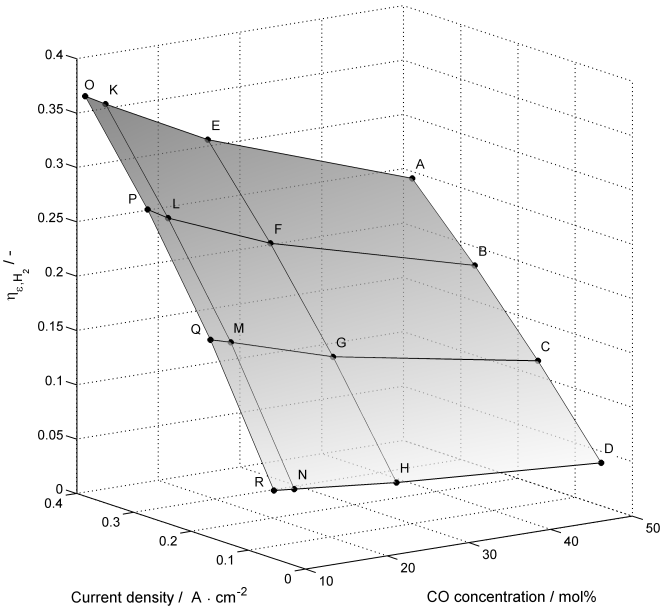


**Figure 5.7.:** The EWGSR exergy efficiency $\eta_{H_2}^{\exp}$ as function of current density and anode CO feed gas concentration, obtained at T = 393 K with 50 mol% $H_2$ (related to the dry anode feed stream). The surface areas and lines in-between the labelled data points originate from linear interpolation.

for the $H_2$ generating electrochemical WGSR.

The anode effluent contains still a significant amount of exergy. In a technical application of the EWGSR concept, the anode effluent exergy content ($H_2$,CO) should be utilised further in consecutive processes as synthesis educt gas or at least in terms of its heating value (see chapter 4.3). If the complete exergy of the anode effluent is included into the exergy efficiency of the EWGSR process as benefit, a total exergy efficiency of $\eta_{tot}^{\exp} = 0.665$ was calculated for the operation at the maximal value of $\eta_{H_2}^{\exp} = 0.368$ (at $i = 0.39$ A cm$^{-2}$, 10 mol% CO).

The highest $\eta_{H_2}^{\exp}$ values were obtained at 10.0 mol% CO and 12.5 mol% CO, which are close to the CO concentration of reformate gas generated from methane steam reforming (≈12.5 mol% CO) [144].

| data point | $\eta_{\epsilon,H_2}$ / - | $c_{CO,dry}$ / mol% | $i$ / A cm$^{-2}$ |
|---|---|---|---|
| A | 0.244 | 50.0 | 0.39 |
| B | 0.182 | 50.0 | 0.28 |
| C | 0.114 | 50.0 | 0.17 |
| D | 0.039 | 50.0 | 0.06 |
| E | 0.310 | 25.0 | 0.39 |
| F | 0.233 | 25.0 | 0.28 |
| G | 0.148 | 25.0 | 0.17 |
| H | 0.052 | 25.0 | 0.06 |
| K | 0.358 | 12.5 | 0.39 |
| L | 0.272 | 12.5 | 0.28 |
| M | 0.177 | 12.5 | 0.17 |
| N | 0.061 | 12.5 | 0.06 |
| O | 0.368 | 10.0 | 0.39 |
| P | 0.283 | 10.0 | 0.28 |
| Q | 0.182 | 10.0 | 0.17 |
| R | 0.063 | 50.0 | 0.06 |

**Table 5.9.:** Summary of experimentally attained hydrogen exergy efficiencies $\eta_{H_2}^{\exp}$, related to the respective CO concentrations and current densities (see figure 5.7).

The feed gas utilisation degree is defined as the ratio between the $H_2$ generation rate $G_{H_2,out}$ and the maximal possible $H_2$ generation rate $G_{H_2,out}^{max}$ (see equation 5.44).

$$Z_{feed} = \frac{G_{H_2,out}}{G_{H_2,out}^{max}} = \frac{I}{2 \cdot F \cdot (G_{H_2,in} + G_{CO,in})} = \frac{I}{I_{max}} \tag{5.44}$$

At low CO concentrations, $\eta_{H_2}^{\exp}$ was higher due to a higher feed gas utilisation degree $Z_{feed}$. The $H_2$ generation rate is proportional to the operation current $I$ and $G_{H_2,out}^{max}$ is defined by the molar feed flow rates of CO ($G_{CO,in}$) and $H_2$ ($G_{H_2,in}$). A lower CO concentration leads under the considered experimental conditions, constant total inlet flow rate and constant inlet $H_2$ concentration, to a lower $G_{H_2,out}^{max}$. As the applied current values were constant during the experiments, $Z_{feed}$ was maximal for the CO feed gas concentration of 10 mol%. With this CO concentration, $Z_{feed} = 0.58$ and $\eta_{H_2}^{\exp} = 0.368$ were achieved at $i = 0.39$ A cm$^{-2}$. In contrast, at 50 mol% CO and $i = 0.39$ A cm$^{-2}$ only a feed gas utilisation of $Z_{feed} = 0.35$ was achieved, which resulted in the lower exergy efficiency of $\eta_{H_2}^{\exp} = 0.244$.
Consequently, $\eta_{H_2}^{\exp}$ values of 0.37 or larger are generally possible at high feed gas utilisation degrees. The achievement of a feed gas utilisation degree $Z_{feed} = 1$ is practically not possible, because mass transport limitations at the anode will pro-

hibit total $H_2$ and CO utilisation within the EWGSR process. Therefore, high feed gas utilisation degrees and operation conditions, which are only marginally or not at all influenced by mass transport limitations, are required to reach high EWGSR exergy efficiency values. Consequently, the optimisation of the EWGSR components (e.g. flow field, gas diffusion layer, catalyst layer, etc.) in terms of mass transport would be beneficial to improve the EWGSR potential to reach high $\eta_{H_2}^{\exp}$ values. Furthermore, a reduction of $H_2O$, added to the dry feed gas, would lower the required heat exergy efforts. As shown in table 4.2, the experiments were carried out with a surplus of $H_2O$ within the anode inlet stream, always exceeding the stoichiometric requirements of the proceeding electrochemical CO oxidation. A reduction of the $H_2O$ content, without significant changes of the cell voltage, would increase the efficiency of the process even further.

## 5.4 Comparison of Investigated $H_2$ Generation Processes

This chapter aims to compare the EWGSR process to alternative reformate based $H_2$ generation processes with regards to the exergy efficiency, related to the generated neat $H_2$. Theoretical exergy efficiencies were calculated in the chapters 5.2.1-5.2.3 for the PSA, MemSep and CWGSR processes using literature data. The exergy efficiency of the EWGSR was determined based on experimental data in chapter 5.3.
Table 5.10 summarises the calculated theoretical exergy efficiencies along with experimentally obtained exergy efficiency values of the EWGSR. Please note that only the highest $\eta_{H_2}^{\exp}$ value, obtained with feed gas utilisation degrees of 0.58 (equation 5.44) for the operation with $H_2$ containing feed gas (10.0 mol% CO, 50.0 mol% $H_2$) is listed here.

First, the exergy efficiencies of the selected EWGSR alternative processes are discussed. As can be seen from table 5.10, both the PSA and the MemSep exergy efficiency show a significant increase, when the inlet feed composition is changed from A to B (refer to table 5.2 for gas composition details). This difference of $\eta_{H_2}^{(1)}$ can be assigned in both cases to a difference in the overall molar exergy $\tilde{\epsilon}_{mix,in}^{\circ}$ of the feed compositions A and B. Composition A exhibits a $\tilde{\epsilon}_{mix,in}^{\circ}$-value of 186.34 $\mathrm{kJ\,mol^{-1}}$, whereas composition B possesses a $\tilde{\epsilon}_{mix,in}^{\circ}$ value of 152.24 $\mathrm{kJ\,mol^{-1}}$. The lower $\tilde{\epsilon}_{mix,in}^{\circ}$ value of composition B originates mainly from the difference of its $H_2$ and CO fractions, as these species possess high chemical exergies (table 5.1).
Furthermore, table 5.10 shows that for both gas compositions the PSA exergy effi-

| inlet | exergy efficiencies PSA | MemSep | CWGSR | EWGSR | |
|---|---|---|---|---|---|
| gas comp. | $\eta_{H_2}^{(1)}$ | $\eta_{H_2}^{(2)}$ | $\eta_{H_2}^{(2)}$ | $\eta_{H_2}^{(exp)}$ | $\eta_{tot}^{(exp)}$ |
| A | 0.411 | 0.493 | - | - | - |
| B | 0.477 | 0.574 | - | - | - |
| C | - | - | 0.536 | - | - |
| Exp($CO$,$H_2$) | - | - | - | 0.368 | 0.665 |

**Table 5.10.:** Exergy efficiencies of theoretically evaluated $H_2$ generating processes: pressure swing adsorption (PSA), membrane separation (MemSep), cyclic water gas shift reactor (CWGSR), and the experimentally investigated EWGSR (10 mol%CO, 50 mol%$H_2$, $Z_{feed}$ = 0.58).

ciency is significantly lower than of the MemSep process. This difference is assumed to result from a lower $H_2$ separation performance of the PSA process. The $H_2$ separation performance can be defined as the amount of separated $H_2$ to the total amount of available $H_2$. This parameter was defined for the MemSep process as recovery index RI (equation 5.32), and was estimated to be about RI = 0.72 for the employed feed composition (equation 5.33). The $H_2$ separation performance of the PSA process can be determined with the help of its product-to-feed ratio $\chi_{76}^{PSA} = 0.45$ and the dry HT-WGSR outlet gas $H_2$ content ($x_{H_2} = 0.75$, table 5.4). This leads to a $H_2$ separation performance of 0.6, which is significantly lower than 0.72, the $H_2$ separation performance (i.e. recovery index) of the MemSep process. Thus, the PSA process supplies, with respect to parameters used in this work, a lower amount of pure $H_2$ from the given feed gas than the MemSep process. This directly leads to a lower $\eta_{H_2}^{(1)}$ value of the PSA process.
The exergy efficiency of the CWGSR process is placed with 0.536 in-between the PSA and MemSep process. The CWGSR process efficiency is mainly dominated by the high process temperatures. The employed inlet feed composition C of the CWGSR process contains however a high amount of CO, if compared to composition A and B (table 5.4). This prohibits a direct comparison to the PSA and MemSep process, as composition C is no typical reformate composition. Generally, the CWGSR can reach similar exergy efficiencies as the established processes, if operated under optimised conditions.

The highest exergy efficiency $\eta_{H_2}^{(exp)} = 0.368$ of the EWGSR was determined at a feed gas utilisation of $Z_{feed} = 0.58$ for the operation with 10.0 mol% CO and 50.0 mol% $H_2$ in the dry feed gas. This efficiency value is about 0.04 lower than the calculated PSA exergy efficiency using feed gas A.

In order to estimate the EWGSR exergy efficiency at feed gas utilisation degrees exceeding the experimental conditions ($Z_{feed} > 0.58$), the obtained experimental results were extrapolated to $Z_{feed} = 0.9$. This feed gas utilisation degree was selected as a target maximal value of a technically well developed and optimised EWGSR. Figure 5.8 shows the exergy efficiency extrapolation, as a continuation of the experimentally determined values, in the range of $0.58 < Z_{feed} \leq 0.9$. The extrapolation does not include effects triggered by educt gas composition changes (e.g. educt starvation, etc.) within the catalyst layer, which might appear especially close to the outlet of the reactor at high feed gas utilisation degrees. These effects might cause a strong increase of the anode overvoltage (i.e. concentration overvoltage), which increases the electrical power demand and, consequently, results in a sharp decrease of the exergy efficiency.

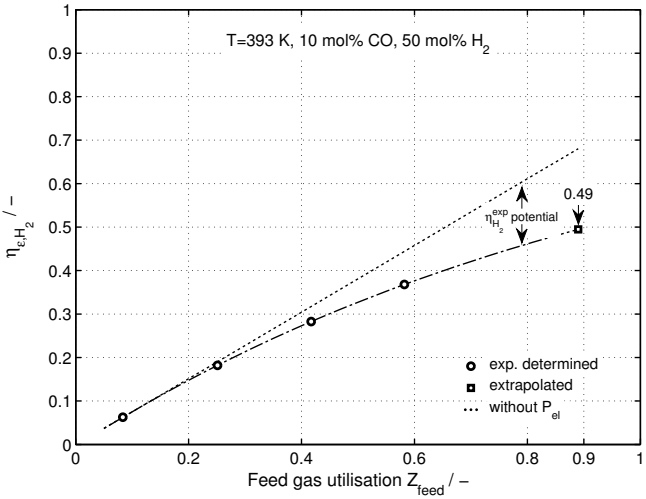


**Figure 5.8.:** Hydrogen exergy efficiency as a function of the feed gas utilisation at 393 K, and 10% CO + 50% $H_2$ within the feed gas.

As shown, at $Z_{feed} = 0.9$ an exergy efficiency of $\eta_{\varepsilon,H_2} = 0.49$ was estimated. This value is higher than the calculated PSA exergy efficiencies and similar to the MemSep exergy calculated for feed composition A (see table 5.10).
Figure 5.8 shows also a dotted line of $\eta_{H_2}^{(exp)}$ vs. $Z_{feed}$ for the theoretical case that no electrical power $P_{el}$ is required for the EWGSR operation ($U(i) = 0, \forall\, i$). The difference between the dotted line and the extrapolated experimental data represents the maximal improvement potential of $\eta_{H_2}^{(exp)}$ with respect to the electrical power consumption.

Obviously, $P_{el}$ will never be zero, but it can be minimised by the reducing the ohmic losses within the reactor, by reducing the reaction overvoltage (i.e. application of more active catalysts), and by improving the mass transport properties within the reactor. Besides the minimisation of $P_{el}$, $\eta_{H_2}^{\exp}$ can be improved by the optimisation of the molar $H_2O$ to CO ratio at the reactor inlet. During the displayed experiment, the molar $H_2O$/CO feed gas ratio was 7.54 (see table 4.2). The majority of the gaseous $H_2O$ exited the reactor without participating in the reaction. Therefore, a significant efficiency increase might be achievable by reducing the amount of $H_2O$ added to the feed stream, i.e by reducing the heat exergy demand of the process. This would result in an increase of the slope of both plotted $\eta_{H_2}^{(exp)}$ curves (with and without $P_{el}$ consideration) in figure 5.8, and thus to higher efficiencies at similar feed gas utilisation degrees. Consequently, an optimisation of the EWGSR operation regarding feed gas utilisation, $H_2O$/CO inlet ratio, and heat integration seems to be promising with regards to a significant efficiency increase.

The comparison of the theoretic exergy calculation results in table 5.10 with the results presented in figure 5.8 identifies a significant potential of the EWGSR to operate in the similar efficiency range as established processes. But, besides efficiency the durability of a process is another important aspect which needs to be addressed in future studies for a complete feasibility evaluation of the here proposed EWGSR concept.

# Chapter 6

# Conclusions

The here presented work was dedicated to the development and investigation of a novel electrochemical membrane reactor (EMR) for the processing of $CO/H_2$ gas mixtures. During autonomous operation, the EMR operated as high temperature PEM type fuel cell (HT-PEMFC). Here, the influence of the CO feed gas concentration upon its steady state performance was investigated. Furthermore, the load change characteristics of the electrical power generating reactor were studied in dependence upon the feed gas and anode catalyst composition.
Under driven operation, the EMR generated pure $H_2$ from reformat type feed gas. This was realised by a dual reaction regime, where $H_2$ was separated from the feed gas, as well as "freshly" generated in the electrical power driven electrochemical water gas shift reactor (EWGSR). The feasibility of the EWGSR concept was investigated and the interdependencies between both the electrochemical CO and $H_2$ oxidation were studied. Finally, the concept was compared to alternative processes, using an exergy efficiency parameter.

The developed EMR exhibited in both investigated operation regimes, i.e. HT-PEMFC and EWGSR, an improvement potential compared to state-of-the-art approaches. The application of a PtRu instead of Pt as anode catalyst significantly improved its CO tolerance in HT-PEMFC mode. Furthermore, the HT-PEMFC equipped with an anodic PtRu catalyst showed an improved current step response of its voltage signal, e.g. lower overshoots.
The EWGSR operation was shown to be feasible and controllable via the applied electrical current and the operation temperature. The current efficiency of the EWGSR process was found to be about 100%, as the $H_2$ evolution rate at the cathode obeyed Faraday's law. Lower temperatures were identified to be beneficial to increase the CO turnover within the reactor. Additionally, it was shown that the required electrical power input during the operation of the EWGSR with CO and $H_2O$ containing feed gas ($H_2$ free) decreases with decreasing temperatures. The increased CO adsorption on the anode catalyst Pt at lower temperatures is most likely responsible for this rather non-intuitive dependency. With CO and

$H_2$ containing feed gas, temperature, inlet concentrations, and current significantly influence the balance between the electrochemical WGSR and the electrochemical $H_2$ oxidation reaction. Furthermore, the $H_2$/CO ratio in the anode effluent gas, an important parameter for subsequent downstream processes, was found to depend upon the EWGSR temperature and the electrical current. This opens up the possibility to operate the EWGSR not only as pure $H_2$ generator, but also as controllable synthesis gas conditioning unit, which simultaneously generates a neat $H_2$ stream. Such a combined gas separation/conditioning unit might be of interest for integrated chemical processes where pure $H_2$, as well as synthesis gas with a defined $H_2$/CO ratio, is required.
Exergy analysis of selected reformat based $H_2$ generation routes was used to provide a basis for the evaluation of the EWGSR concept in comparison to state-of-the-art processes. Here, literature based exergy efficiencies of the process examples and the experimentally determined exergy efficiency of the EWGSR were discussed. It was shown that the EWGSR operation conditions need to be selected carefully in order to achieve similar efficiencies as the selected state-of-the-art process examples. Nevertheless, the analysis revealed optimisation directions and promising improvement potentials of the EWGSR operation. The results indicate that a reduction of the $H_2O$/CO ratio in the reactor feed gas ($H_2O/CO \rightarrow 1$) and a reduction of the operation temperature (i.e. support of CO adsorption) might substantially improve the EWGSR process. For the latter, it might be beneficial to investigate the utilisation of alternatives to $H_3PO_4$ doped polybenzimidazole as proton conducting membrane material. These alternative materials should enable an operation temperature range between 363 K and 383 K. This will lead to a significant increase of the CO turnover during the EWGSR operation with $H_2$/CO containing feed gases and, consequently, enable a higher feed gas utilisation degrees of the overall process.
Next-to experimental activities, the development of mathematical models for the simulation of selected processes within the EWGSR, of the EWGSR as a whole or as part of an integrated chemical process, is a promising continuation option of the here presented work. A model, which addresses the observed operation parameter dependency of the electrochemical CO oxidation, will increase the understanding of the processes at the anode of the EWGSR. This will be most likely beneficial for the required optimisation of the EWGSR operation (e.g. $H_2O/CO$ ratio, temperature, etc.). A model which describes the EWGSR as a reactor could be used to expand upon the efficiency considerations of this work at high feed gas utilisation degrees and might be the basis of a integrated chemical process model where the EWGSR is only one reactor within a chain of process units.

The here presented project and its results can be positioned into the long line of the continuous research projects within the highly interdisciplinary field of process

and energy engineering. As in all research fields, every project which finds answers generates simultaneously new challenges. Newly raised challenges of the here presented HT-PEMFC /EWGSR project address topics like reactor and process design, material optimisation, reactor durability and also economic feasibility. The handling of these challenges will decide about the chances of the HT-PEMFC and EWGSR to contribute to the ambitious goals which were discussed at the very beginning of this thesis.

# Appendix

# Appendix A

# NIST Coefficients

The following table summarises coefficients, supplied from the National Institute of Standards and Technology [149]. This data was used within the calculation of enthalpy and entropy according to the equations 5.10 and 5.13, respectively.

| Coefficient | $H_2$ | CO | $CO_2$ | $H_2O$ | $CH_4$ | $N_2$ |
|---|---|---|---|---|---|---|
| A | 33.066178 | 25.56759 | 24.99735 | -203.6060 | -0703029 | 28.98641 |
| B | -11.363417 | 6.096130 | 55.18696 | 1523.290 | 108.4773 | 1.853978 |
| C | 11.432816 | 4.054656 | -33.69137 | -3196.413 | -42.52157 | -9.647459 |
| D | -2.772874 | -2.671301 | 7.948387 | 2474.455 | 5.862788 | 16.63537 |
| E | -0.158558 | 0.131021 | -0.136638 | 3.855326 | 0.678565 | 0.000117 |
| F | -9.980797 | -118.0089 | -403.6075 | -256.5478 | -76.84376 | -8.671914 |
| G | 172.707974 | 227.3665 | 228.2431 | -488.7163 | 158.7163 | 226.4168 |
| H | 0.0 | -110.5271 | -393.5224 | -285.8304 | -74.87310 | 0.0 |
| $T_{valid}$, [K] | 298…1000 | 298…1300 | 298…1200 | 298…500 | 298…1300 | 100…500 |
| | | | | | | |
| A | 18.563083 | | | 30.09200 | | 19.50583 |
| B | 12.257357 | | | 6.832514 | | 19.88705 |
| C | -2.859786 | | | 6.793435 | | -8.598535 |
| D | 0.268238 | | | -2.534480 | | 1.369784 |
| E | 1.977990 | | | 0.082139 | | 0.527601 |
| F | -1.147438 | | | -250.8810 | | -4.935202 |
| G | 156.288133 | | | 223.3967 | | 212.3900 |
| H | 0.0 | | | -241.8264 | | 0.0 |
| $T_{valid}$, [K] | 1000…2500 | | | 500…1700 | | 500…2000 |

**Table A.1.:** NIST coefficients of the considered substances

# Appendix B

# CWGSR $H_2$ Exergy Efficiency

In the following, the derivation of the CWGSR hydrogen exergy efficiency ($\eta_{\tilde{e},H_2}$) is presented. The used variables and indication numbers refer to the CWGSR process scheme shown in figure 5.5. Please note, that all exergy efficiency derivations within this work employ molar flow rates which are related to the reformate feed gas stream (i.e.$G_1$) of the reactor.

$$\eta^2_{\tilde{e},H_2} = \frac{\tilde{\epsilon}^\circ_{H_2} \cdot \frac{G_{H_2,prod}}{G_{in(refomat)}}}{\tilde{\epsilon}_{in,1} \cdot \frac{G_1}{G_{in(refomat)}} + \tilde{\epsilon}^\circ_{H_2O} \cdot \frac{G_{3(H_2O)}}{G_{in(refomat)}} + E_{q,netto} \cdot \frac{G_{in(refomat)}}{G_{in(refomat)}}} \tag{B.1}$$

$$\eta^2_{\tilde{e},H_2} = \frac{\tilde{\epsilon}^\circ_{H_2} \cdot x_{H_2,6} \cdot \frac{G_6}{G_1}}{\tilde{\epsilon}_{in,1} \cdot \frac{G_1}{G_1} + \tilde{\epsilon}^\circ_{H_2O} \cdot \frac{G_{3(H_2O)}}{G_1} + E_{q,netto} \cdot \frac{G_1}{G_1}} \tag{B.2}$$

$$\eta^2_{\tilde{e},H_2} = \frac{\tilde{\epsilon}^\circ_{H_2} \cdot x_{H_2,6} \cdot \frac{G_6}{G_5} \cdot \frac{G_5}{G_1}}{\tilde{\epsilon}_{in,1} + \tilde{\epsilon}^\circ_{H_2O} \cdot X^{CWGSR}_{31} + E_{q,netto}} \tag{B.3}$$

$$\eta^2_{\tilde{e},H_2} = \frac{\tilde{\epsilon}^\circ_{H_2} \cdot x_{H_2,6} \cdot X^{CWGSR}_{65} \cdot \frac{G_5}{G_{3(H_2O)}} \cdot \frac{G_{3(H_2O)}}{G_1}}{\tilde{\epsilon}_{in,1} + \tilde{\epsilon}^\circ_{H_2O} \cdot X^{CWGSR}_{31} + E_{q,netto}} \tag{B.4}$$

$$\eta^2_{\tilde{e},H_2} = \frac{\tilde{\epsilon}^\circ_{H_2} \cdot x_{H_2,6} \cdot X^{CWGSR}_{65} \cdot (\frac{G_1+G_{3(H_2O)}}{G_{3(H_2O)}} \cdot X^{CWGSR}_{31})}{\tilde{\epsilon}_{in,1} + \tilde{\epsilon}^\circ_{H_2O} \cdot X^{CWGSR}_{31} + E_{q,netto}} \tag{B.5}$$

$$\eta^2_{\tilde{e},H_2} = \frac{\tilde{\epsilon}^\circ_{H_2} \cdot x_{H_2,6} \cdot X^{CWGSR}_{65} \cdot ((\frac{G_1}{G_{3(H_2O)}} + 1) \cdot X^{CWGSR}_{31})}{\tilde{\epsilon}_{in,1} + \tilde{\epsilon}^\circ_{H_2O} \cdot X^{CWGSR}_{31} + E_{q,netto}} \tag{B.6}$$

$$\eta^2_{\tilde{e},H_2} = \frac{\tilde{\epsilon}^\circ_{H_2} \cdot x_{H_2,6} \cdot X^{CWGSR}_{65} \cdot ((\frac{1}{X^{CWGSR}_{31}} + 1) \cdot X^{CWGSR}_{31})}{\tilde{\epsilon}_{in,1} + \tilde{\epsilon}^\circ_{H_2O} \cdot X^{CWGSR}_{31} + E_{q,netto}} \tag{B.7}$$

$$\eta^2_{\tilde{e},H_2} = \frac{\tilde{\epsilon}^\circ_{H_2} \cdot x_{H_2,6} \cdot X^{CWGSR}_{65} (1 + X^{CWGSR}_{31})}{\tilde{\epsilon}_{in,1} + \tilde{\epsilon}^\circ_{H_2O} \cdot X^{CWGSR}_{31} + E_{q,netto}} \tag{B.8}$$

# Appendix C

# Determination of the Water Addition Rate

The dew point temperature $T_{dew}$ in the anode feed stream of the EWGSR (i.e. $G_{in,EWGSR}$) was continuously measured after the tempered bubbler flask cascade. Assuming the applicability of the ideal gas law and a negligible pressure difference between the gas ($T_{dew}$ measurement) and the ambient pressure, equation 3.7 is derived in the following. It was used for the calculation of the added $H_2O$ flow rate ($G_{H_2O}$) to the EWGSR anode feed gas.

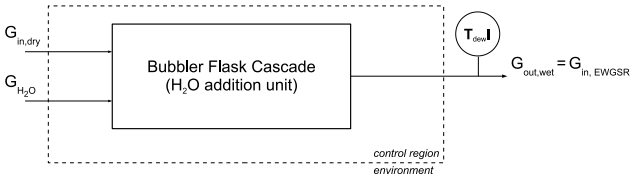


**Figure C.1.:** The mass balance boundaries of the bubbler flask cascade with indicated inlet and outlet streams.

The basis is a mass balance which encloses the applied bubbler flask cascade as shown in figure C.1. Equation C.1 represents the steady state mass balance of the bubbler flask cascade and equation C.2 is a simple expression of the partial pressure relations within $G_{out,wet}$. The combination of both equations leads to the expression of the $H_2O$ addition rate ($G_{H_2O}$).

$$G_{in,dry} + G_{H_2O} = G_{out,wet} \tag{C.1}$$

$$\frac{G_{H_2O}}{G_{out,wet}} = \frac{p_{H_2O}}{p_{gas}} \tag{C.2}$$

$$G_{H_2O} = \frac{p_{H_2O}}{p_{gas} - p_{,H_2O}} \cdot G_{in,dry} \tag{C.3}$$

The Antoine equation (equation C.4) allows for the calculation of the water vapour saturation pressure $p_{s,H_2O}$ at the temperature T. If the gas temperature is equal to the gas dew point temperature ($T = T_{dew}$), the calculated water vapour saturation

pressure is equal to the partial water vapour pressure within the gas ($p_{H_2O} = p_{s,H_2O}$). Thus, using the dew point temperature of a gas within the Antoine equation (equation C.4), rearranged to $p_{s,H_2O}$, leads to the partial water vapour pressure within the gas at the gas temperature T, under the conditions $T > T_{dew}$ and $V_{gas} \neq$ const..

$$log_{10}[p_{s,H_2O}(T).10^{-5}] = 4,65430 - \frac{1435,264}{T + (-64,848)} \tag{C.4}$$

Consequently, the water vapour pressure within the wet bubbler cascade outlet stream $G_{out,wet}$ was calculated with the measured gas dew point temperature and the Antoine equation. This leads in combination with equation C.3 to the final equation for the determination of the water addition rate by using the dew point temperature of $G_{out,wet}$ and the set dry feed gas rate $G_{in,dry}$ (equation C.5 or 3.7). Within this work, the Antonie equation parameter of Stull were applied [157].

$$G_{H_2O} = \frac{p_{H_2O}(T_{dew})}{p_{gas} - p_{H_2O}(T_{dew})} \cdot G_{in,dry} \tag{C.5}$$

# Appendix D

# Experimental Preparation Methods

Details about the practical preparation methods, employed in this work, are documented in the following. At first, the preparation of the gas diffusion electrode (GDE) is adressed, followed by the acid doping of the applied poly(2,5-benzimidazole) (ABPBI) polymer. Finally, description of the membrane electrode assembly preparation, as well its installation into the reactor flow field plates, is provided.

## D.1 Gas Diffusion Electrode Preparation

The here described preparation method of the gas diffusion electrodes (GDE) is conducted prior to the preparation of the membrane electrode assembly (MEA). The GDE is prepared by applying the catalyst ink with an air brush method on top of the micro-porous layer of a carbon cloth gas diffusion layer sheet. The catalyst composition, as well as the catalyst loading used in this work, are listed in table 3.1.

**Required Materials**

- carbon cloth material & catalyst powder (e.g. Pt on carbon)
- $H_3PO_4$ solution (e.g. 6 M) PTFE solution
- dimethylacetamid (DMAC, be aware carcinogenic!!)
- ultra sonic bath
- glass flask & pipettes
- air brush gun with compressor
- temperature controlled heating table ($T_{max}$>443 K), incl. air removal on its surface via vacuum pump
- carbon cloth fixture frame and spay template, fitting to the vacuum-heating table
- precision balance & oven ($T_{max}$)>453 K)

- fume hood and gas mask equipped with organic component filter
- 1 x scalpel knife
- 2 x medium Petri dish (for $H_3PO_4$ bath)
- DMAC resistant gloves

**Preparation Steps**

- Prepare the catalyst ink according to the anticipated metal and PTFE loadings: a) weighing of the respective catalyst powder amount within the glass flask, b) addition of the carrier liquid DMAC, c) addition of the respective amount of PTFE solution.
- Dissipate the catalyst particles within the carrier liquid by placing the catalyst ink in an closed glass flask into an ultra sonic bath for 2 hours.
- Place the carbon cloth material into the carbon cloth fixture frame, followed by placing the frame onto the heating table.
- Set the heating table temperature to 445 K, which allows for the evaporation of the used catalyst carrier liquid DMAC. Do not breath in the DMAC fumes! Wear a gas mask equipped with the respective filter!
- Apply the catalyst ink on the GDL surface using the air brush gun. Use the glass pipettes to refill the air brush ink compartment with the catalyst ink. The applied catalyst surface loading can be determined after complete evaporation of the carrier liquid. Here, use the precision balance and the catalyst to PTFE weight ratio within the applied catalyst ink to determine the surface loading.
- Keep the finished catalyst layer coated carbon cloth enclosed by the fixture frame and sinter the catalyst layer for 2 hours at 453 K.
- Remove the prepared GDE from the frame fixture and cut it into the required size with the scalpel knife.
- Fill one medium size Petri dish with the prepared $H_3PO_4$ solution, place the GDE with the catalyst layer facing down into the acid solution and place the second Petri Dish as a cover on top. The GDE within the acid bath is placed, along with the HT-PEM (see appendix D.2), for 24 h at 353 K into the oven.
- Remove the GDE from the acid solution and put it, with the catalyst layer facing up, together with the HT-PEM, for 6h at 393 K into the oven.
- After the drying step, the GDE can be used for the MEA preparation (see appendix D.3).

## D.2 High Temperature Proton Conducting Membrane Preparation

The here described preparation method of the high temperature proton conducting membrane (HT-PEM) is conducted prior to the preparation of the membrane electrode assembly (MEA). The base, acid free, polymer used for the preparation of the HT-PEM was poly(2,5-benzimidazole) (ABPBI). The polymer was purchased as membrane sheets from FumaTech.

**Required Materials**

- ABPBI membrane material
- $H_3PO_4$ solution (e.g. 12 M)
- PTFE foil roll (thickness 0.25 mm)
- 1 x scalpel knife
- 1 x large Petri dish (for $H_3PO_4$ bath)
- 2 x medium Petri dish
- 1 x glass plate for cutting with smooth surface
- membrane cutting shape template
- gloves & oven ($T_{max}$>453 K)

**Preparation Steps**

- Pre-size the ABPBI Membrane with the scalpel knife and the cutting shape template. Be aware, the cut lines must be free of any cracks, uneven surfaces, edges, etc.! Otherwise the acid doped membrane will start to rip from these points. The membrane will expand during the acid uptake and needs to be cut into the required dimensions after the acid doping with the help of the shape template.
- Place the pre-sized membrane in-between two PTFE foils (larger than the membrane piece).
- Fill the large Petri dish with $H_3PO_4$ acid of the respective concentration (HT-PEMFC: 13 M , EWGSR: 12 M). Please refer to Fig. 3.5 to select the respective acid concentration based upon the anticipated acid doping level.
- Place the package "PTFE - ABPBI - PTFE" into the acid solution. Please ensure a complete wetting of the membrane with $H_3PO_4$. Place the medium size Petri dish on top of the package "PTFE - ABPBI - PTFE", to avoid any rolling of the ABPBI membrane. Close the large Petri dish with the appropriate glass cover.
- The membrane remains now for the anticipated time under the anticipated temperature within the $H_3PO_4$ solution (see Fig. 3.5). For the HT-PEMFC and EWGSR

application, the membrane was doped for 24 h at 353 K to achieve a doping level of 4.6 $^{mol}/_{mol}$ and 4.0 $^{mol}/_{mol}$, respectively.

- Subsequent the doping step, remove the package "PTFE - ABPBI - PTFE" from the $H_3PO_4$ solution bath and remaining $H_3PO_4$ solution is removed from the surface of the package.
- After the acid removal, dry the package "PTFE - ABPBI - PTFE" for 6h at 393 K to lower the $H_2O$ content within the membrane.
- Subsequent to the drying, remove the membrane carefully from the PTFE package and placed on the priorly cleaned glass plate (be aware, the membrane tends to roll). If necessary, apply some $H_3PO_4$ on the glass surface to realise good adhesion of the membrane on the glass plate (use gloves!).
- The flat membrane can now be dimensioned with the shape template and the scalpel knife.
- Once the acid doped membrane is cut into the required dimensions, it can be used for the MEA preparation (see appendix D.3).

## D.3 Membrane Electrode Assembly Preparation

The here described preparation method of the membrane electrode assembly combines the acid doped HT-PEM (see appendix D.2) with the GDE (see appendix D.1). The total, 2 days were required for the preparation the MEA's used in this work, including the preparation of the HT-PEM and the GDE. The ready prepared MEA, enclosed in the two graphite flow field plates, was installed within the reactor without additional delays.

**Required Materials**

- prepared & dimensioned $H_3PO_4$ doped ABPBI Membrane
- prepared & dimensioned $H_3PO_4$ doped GDEs for anode and cathode
- PTFE based MEA frame structure, incl. inner (2 pieces) & outer frame (2 pieces)
- plastic tweezers
- 2 x graphite flow field plates, fitting to the MEA frame structure
- 1 x PTFE foil (0.25 mm thick)

**Preparation Steps**

- Place the acid doped HT-PEM within the larger piece of the inner frame structure. Close the frame on top of the HT-PEM using the smaller part of the inner frame structure, which encloses the HT-PEM in-between the larger and the smaller piece of the inner frame structure.
- Place the GDE with the tweezers upon the exposed HT-PEM, which is held by the inner frame structure. If cut properly, the GDE covers the complete remaining inner surface of the HT-PEM, which is not covered by the inner frame structure.
- Position one part of the outer frame structure on top of the GDE, which keeps the GDE in the right position.
- Place the PTFE foil on top of the assembly and use it as a fixation, while turning the assembly and, subsequently, placing it on one of the prepared graphite flow field plates. Here, the side, where the outer frame structure is already positioned, faces down to the flow field plate. The shape of the outer frame structure should align with the shape of the flow field plate.
- Place the second GDE upon the now exposed surface of the HT-PEM (opposite side than the first GDE) and, subsequently, place the second part of the outer frame structure on top of the GDE. Here, the shape of the outer frame aligns with the shape of the inner frame.
- Finally, place the second flow field plate upon the ready assembled MEA. The complete assembly (flow field plate - MEA in frame structure - flow field plate)

is, subsequently, enclosed by the respective current collectors and steel plates to form the single cell reactor.

# Declaration

This dissertation contains material that has previously been published elsewhere. The following list gives the details.

1. C.Oettel, L. Rihko-Struckmann, and K. Sundmacher. Improved CO tolerance with PtRu anode catalysts in ABPBI based high temperature proton exchange membrane fuel cells. *J. Fuel Cell Sci. Tech., 9(3),2012.*
2. C.Oettel, L. Rihko-Struckmann, and K. Sundmacher. Combined generation and separation of hydrogen in an electrochemical water gas shift reactor (EWGSR). *Int. J. Hydrog. Energy, 37(8):6635-6645,2012.*
3. C.Oettel, L. Rihko-Struckmann, and K. Sundmacher. Characterisation of the electrochemical water gas shift reactor (EWGSR) operated with hydrogen and carbon monoxide rich feed gas. *Int. J. Hydrog. Energy, 37(16):11759-11771,2012.*

# Bibliography


[1] W. S. Broecker. Climatic change - are we on brink of a pronounced global warming. *Science*, 189(4201):460–463, 1975.

[2] T. M. L. Wigley, P. D. Jones, and P. M. Kelly. Global warming ? *Nature*, 291(5813):285–285, 1981.

[3] R. E. Dickinson and R. J. Cicerone. Future global warming from atmospheric trace gases. *Nature*, 319(6049):109–115, 1986.

[4] United Nations Framework Convention on Climate Change. Report of the conference of the parties on its sixteenth session, held in cancun from 29 november to 10 december 2010. Technical report, 2011.

[5] S. Shafiee and E. Topal. When will fossil fuel reserves be diminished? *Energy Policy*, 37(1):181–189, 2009.

[6] Federal Government of Germany. The path to the energy of the future - reliable, affordable and environmentally sound ; the fundamental energy transition strategy of the federal government of germany, 2011.

[7] J. D. Holladay, J. Hu, D. L. King, and Y. Wang. An overview of hydrogen production technologies. *Catal. Today*, 139(4):244–260, 2009.

[8] J. Turner, G. Sverdrup, M. K. Mann, P. C. Maness, B. Kroposki, M. Ghirardi, R. J. Evans, and D. Blake. Renewable hydrogen production. *Int. J. Energy Res.*, 32(5):379–407, 2008.

[9] Y. Kalinci, A. Hepbasli, and I. Dincer. Biomass-based hydrogen production: A review and analysis. *Int. J.Hydrog. Energy*, 34(21):8799–8817, 2009.

[10] J. R. Rostrup-Nielsen and T. Rostrup-Nielsen. Large-scale hydrogen production. *Cattech*, 6(4):150–159, 2002.

[11] B. Johnston, M. C. Mayo, and A. Khare. Hydrogen: the energy source for the 21st century. *Technovation*, 25(6):569–585, 2005.

[12] N. V. Gnanapragasam, B. V. Reddy, and M. A. Rosen. Hydrogen production from coal gasification for effective downstream $CO_2$ capture. *Int. J. Hydrog. Energy*, 35(10):4933–4943, 2010.

[13] European Commission. *EUR 23123 — HyWays – the European Hydrogen Roadmap*. Office for Official Publications of the European Communities, Luxembourg, 2008.

[14] M. Bohnet and F. Ullmann. *Hydrocarbons to Indole*, volume 17 of *Ullmann's Encyclopedia of Industrial Chemistry*. Wiley-VCH, 6 edition, 2003.

[15] C. H. Bartholomew and R. J. Farrauto. *Fundamentals of Industrial Catalytic Processes*. John Wiley & Sons, Inc., Hoboken, NJ, USA, 2006.

[16] M. E. Dry. The Fischer-Tropsch process: 1950-2000. *Catal. Today*, 71(3-4):227–241, 2002.

[17] K. Aasberg-Petersen, T. S. Christensen, I. Dybkjaer, J. Sehested, M. Ostberg, R. M. Coertzen, M. J. Keyser, and A. P. Steynberg. Synthesis gas production for FT synthesis. *Fischer-Tropsch Technology*, 152:258–405, 2004.

[18] M. Stelmachowski and L. Nowicki. Fuel from the synthesis gas - the role of process engineering. *Appl. Energy*, 74(1-2):85–93, 2003.

[19] I. Wender. Reactions of synthesis gas. *Fuel Process. Technol.*, 48(3):189–297, 1996.

[20] J. R. Rostrup Nielsen. Production of synthesis gas. *Catal. Today*, 18(4):305–324, 1993.

[21] M. Ni, D. Y. C. Leung, M. K. H. Leung, and K. Sumathy. An overview of hydrogen production from biomass. *Fuel Process. Technol.*, 87(5):461–472, 2006.

[22] A. Ursua, L. M. Gandia, and P. Sanchis. Hydrogen production from water electrolysis: Current status and future trends. *Proc. IEEE*, 100(2):410–426, 2012.

[23] K. Zeng and D. K. Zhang. Recent progress in alkaline water electrolysis for hydrogen production and applications. *Prog. Energy Combust. Sci.*, 36(3):307–326, 2010.

[24] S. A. Grigoriev, V. I. Porembsky, and V. N. Fateev. Pure hydrogen production by PEM electrolysis for hydrogen energy. *Int. J. Hydrog. Energy*, 31(2):171–175, 2006.

[25] M. Ni, M. K. H. Leung, and D. Y. C. Leung. Technological development of hydrogen production by solid oxide electrolyzer cell (*soec*). *Int. J. Hydrog. Energy*, 33(9):2337–2354, 2008.

[26] T. Kodama and N. Gokon. Thermochemical cycles for high-temperature solar hydrogen production. *Chem. Rev.*, 107(10):4048–4077, 2007. Kodama, Tatsuya Gokon, Nobuyuki.

[27] M. A. Rosen. Advances in hydrogen production by thermochemical water decomposition: A review. *Energy*, 35(2):1068–1076, 2010.

[28] A. Steinfeld. Solar thermochemical production of hydrogen - a review. *Sol. Energy*, 78(5):603–615, 2005.

[29] R. Kothari, D. Buddhi, and R. L. Sawhney. Comparison of environmental and economic aspects of various hydrogen production methods. *Renew. Sust. Energ. Rev.*, 12(2):553–563, 2008.

[30] E. D. Park, D. Lee, and H. C. Lee. Recent progress in selective CO removal in a $H_2$-rich stream. *Catal. Today*, 139(4):280–290, 2009.

[31] T. Giroux, S. Hwang, Y. Liu, W. Ruettinger, and L. Shore. Monolithic structures as alternatives to particulate catalysts for the reforming of hydrocarbons for hydrogen generation. *Appl. Catal. B-Environ.*, 56(1-2):95–110, 2005.

[32] D. S. Newsome. The Water-Gas Shift Reaction. *Catal. Rev.-Sci. Eng.*, 21(2):275–318, 1980.

[33] D. C. Grenoble, M. M. Estadt, and D. F. Ollis. The Chemistry and Catalysis of the Water Gas Shift Reaction. 1. The Kinetics over supported Metal-Catalysts. *J. Catal.*, 67(1):90–102, 1981.

[34] D. Mendes, A. Mendes, L. M. Madeira, A. Iulianelli, J. M. Sousa, and A. Basile. The water-gas shift reaction: from conventional catalytic systems to pd-based membrane reactors - a review. *Asia-Pac. J. Chem. Eng.*, 5(1):111–137, 2010.

[35] J. N. Armor. The multiple roles for catalysis in the production of $H_2$. *Appl. Catal. A-Gen.*, 176(2):159–176, 1999. Armor, JN.

[36] D. L. Trimm. Minimisation of carbon monoxide in a hydrogen stream for fuel cell application. *Appl. Catal. A-Gen.*, 296(1):1–11, 2005.

[37] R. Farrauto, S. Hwang, L. Shore, W. Ruettinger, J. Lampert, T. Giroux, Y. Liu, and O. Ilinich. New material needs for hydrocarbon fuel processing: Generating hydrogen for the PEM fuel cell. *Ann. Rev. Mater. Res.*, 33:1–27, 2003.

[38] S. Sircar and T. C. Golden. Purification of hydrogen by pressure swing adsorption. *Sep. Sci. Technol.*, 35(5):667–687, 2000.

[39] A. H. Malek and S. Farooq. Hydrogen purification from refinery fuel gas by pressure swing adsorption. *AICHE J.*, 44(9):1985–1992, 1998.

[40] W. J. Koros and G. K. Fleming. Membrane-based gas separation. *J. Membr. Sci.*, 83(1):1–80, 1993.

[41] S. Adhikari and S. Fernando. Hydrogen membrane separation techniques. *Ind. Eng. Chem. Res.*, 45(3):875–881, 2006.

[42] T. M. Nenoff, R. J. Spontak, and C. M. Aberg. Membranes for hydrogen purification: An important step toward a hydrogen-based economy. *MRS Bull.*, 31(10):735–741, 2006.

[43] L. Chalakov, L. K. Rihko-Struckmann, B. Munder, H. Rau, and K. Sundmacher. Reaction induced current generation by butane oxidation in high temperature electrochemical membrane reactor. *Chem. Eng. J.*, 131(1-3):15–22, 2007.

[44] B. Munder, Y. M. Ye, L. Rihko-Struckmann, and K. Sundmacher. Solid electrolyte membrane reactor for controlled partial oxidation of hydrocarbons: Model and experimental validation. *Catal. Today*, 104(2-4):138–148, 2005.

[45] G. J. Yusem and P. N. Pintauro. The electrocatalytic hydrogenation of soybean oil. *J. Am. Oil Chem. Soc.*, 69(5):399–404, 1992.

[46] W. D. An, J. K. Hong, P. N. Pintauro, K. Warner, and W. Neff. The electrochemical hydrogenation of edible oils in a solid polymer electrolyte reactor. I. Reactor design and operation. *J. Am. Oil Chem. Soc.*, 75(8):917–925, 1998.

[47] D. L. Stojic, M. P. Marceta, S. P. Sovilj, and S. S. Miljanic. Hydrogen generation from water electrolysis - possibilities of energy saving. *J. Power Sources*, 118(1-2):315–319, 2003.

[48] S. R. Narayanan, B. Haines, J. Soler, and T. I. Valdez. Electrochemical conversion of carbon dioxide to formate in alkaline polymer electrolyte membrane cells. *J. Electrochem. Soc.*, 158(2):A167–A173, 2011.

[49] A. Brisse, J. Schefold, and M. Zahid. High temperature water electrolysis in solid oxide cells. *Int. J. Hydrogen Energ.*, 33(20):5375–5382, 2008.

[50] J. R. Varcoe and R. C. T. Slade. Prospects for alkaline anion-exchange membranes in low temperature fuel cells. *Fuel Cells*, 5(2):187–200, 2005.

[51] G. F. McLean, T. Niet, S. Prince-Richard, and N. Djilali. An assessment of alkaline fuel cell technology. *Int. J. Hydrog. Energy*, 27(5):507–526, 2002.

[52] G. Merle, M. Wessling, and K. Nijmeijer. Anion exchange membranes for alkaline fuel cells: A review. *J. Membr. Sci.*, 377(1-2):1–35, 2011.

[53] J. L. Zhang, Z. Xie, J. J. Zhang, Y. H. Tanga, C. J. Song, T. Navessin, Z. Q. Shi, D. T. Song, H. J. Wang, D. P. Wilkinson, Z. S. Liu, and S. Holdcroft. High temperature PEM fuel cells. *J. Power Sources*, 160(2):872–891, 2006.

[54] W. T. Grubb and L. W. Niedrach. Batteries with solid ion-exchange membrane electrolytes. 2. Low-temperature hydrogen-oxygen fuel cells. *J. Electrochem. Soc.*, 107(2):131–135, 1960.

[55] V. Mehta and J. S. Cooper. Review and analysis of PEM fuel cell design and manufacturing. *J. Power Sources*, 114(1):32–53, 2003.

[56] R. M. Ormerod. Solid oxide fuel cells. *Chem. Soc. Rev.*, 32(1):17–28, 2003.

[57] N. Q. Minh. Ceramic fuel-cells. *J. Am. Ceram. Soc.*, 76(3):563–588, 1993.

[58] N. Q. Minh. Solid oxide fuel cell technology-features and applications. *Solid State Ionics*, 174(1-4):271–277, 2004. Minh, NQ SI.

[59] K. Sundmacher, L. K. Rihko-Struckmann, and V. Galvita. Solid electrolyte membrane reactors: Status and trends. *Catal. Today*, 104(2-4):185–199, 2005.

[60] M. Stoukides. Solid-electrolyte membrane reactors: Current experience and future outlook. *Catal. Rev.-Sci. Eng.*, 42(1-2):1–70, 2000.

[61] K. Juttner, U. Galla, and H. Schmieder. Electrochemical approaches to environmental problems in the process industry. *Electrochim. Acta*, 45(15-16):2575–2594, 2000.

[62] C. Oettel, L. Rihko-Struckmann, and K. Sundmacher. Improved CO tolerance with PtRu anode catalysts in ABPBI based high temperature proton exchange membrane fuel cells. *J. Fuel Cell Sci. Tech.*, 9(3), 2012.

[63] C. Oettel, L. Rihko-Struckmann, and K. Sundmacher. Combined generation and separation of hydrogen in an electrochemical water gas shift reactor (EWGSR). *Int. J. Hydrog. Energy*, 37(8):6635–6645, 2012.

[64] S. Gottesfeld and J. Pafford. A new approach to the problem of carbon-monoxide poisoning in fuel-cells operating at low-temperatures. *J. Electrochem. Soc.*, 135(10):2651–2652, 1988.

[65] H. F. Oetjen, V. M. Schmidt, U. Stimming, and F. Trila. Performance data of a proton exchange membrane fuel cell using $H_2$/CO as fuel gas. *J. Electrochem. Soc.*, 143(12):3838–3842, 1996.

[66] S. J. Lee, S. Mukerjee, E. A. Ticianelli, and J. McBreen. Electrocatalysis of CO tolerance in hydrogen oxidation reaction in PEM fuel cells. *Electrochim. Acta*, 44(19):3283–3293, 1999.

[67] P. Stonehart and P. N. Ross. Commonality of surface processes in electrocatalysis and gas-phase heterogeneous catalysis. *Catal. Rev.-Sci. Eng.*, 12(1):1–35, 1975.

[68] H. Igarashi, T. Fujino, and M. Watanabe. Hydrogen electrooxidation on platinum catalysts in the presence of trace crbon-monoxide. *J. Electroanal. Chem.*, 391(1-2):119–123, 1995.

[69] J. X. Zhang and R. Datta. Sustained potential oscillations in proton exchange membrane fuel cells with PtRu as anode catalyst. *J. Electrochem. Soc.*, 149(11):A1423–A1431, 2002.

[70] L. W. Niedrach, D. W. McKee, J. Paynter, and I. F. Danzig. Electrocatalysts for hydrogen/carbon monoxide fuel cell anodes. I. Platinum-Ruthenium system. *Electrochem. Technol.*, 5(7-8):318–&, 1967.

[71] H. A. Gasteiger, N. Markovic, P. N. Ross, and E. J. Cairns. CO electrooxiation on well-characterized Pt-Ru alloys. *J. Phys. Chem.*, 98(2):617–625, 1994.

[72] H. A. Gasteiger, N. M. Markovic, and P. N. Ross. $H_2$ and CO electrooxidation on well-characterized Pt, Ru, and Pt-Ru .1. rotating-disk electrode studies of the pure gases including temperature effects. *J. Phys. Chem.*, 99(20):8290–8301, 1995.

[73] H. A. Gasteiger, N. M. Markovic, and P. N. Ross. $H_2$ and CO electrooxidation on well-characterized Pt, Ru, and Pt-Ru. 2. rotating disk electrode studies

of CO/$H_2$ mixtures at 62-degrees-C. *J. Phys. Chem.*, 99(45):16757–16767, 1995.

[74] B. N. Grgur, N. M. Markovic, and P. N. Ross. Electrooxidation of $H_2$, CO and $H_2$/CO mixtures on a well-characterized Pt-Re bulk alloy electrode and comparison with other Pt binary alloys. *Electrochim. Acta*, 43(24):3631–3635, 1998.

[75] B. N. Grgur, N. M. Markovic, and P. N. Ross. The electro-oxidation of $H_2$ and $H_2$/CO mixtures on carbon-supported PtxMoy alloy catalysts. *J. Electrochem. Soc.*, 146(5):1613–1619, 1999.

[76] P. C. H. Mitchell, P. Wolohan, D. Thompsett, and S. J. Cooper. Experimental and theoretical studies of fuel cell catalysts: Density functional theory calculations of $H_2$ dissociation and CO chemisorption on fuel cell metal dimers. *J. Mol. Catal. A-Chem.*, 119(1-3):223–233, 1997.

[77] E. Christoffersen, P. Liu, A. Ruban, H. L. Skriver, and J. K. Norskov. Anode materials for low-temperature fuel cells: A density functional theory study. *J. Catal.*, 199(1):123–131, 2001.

[78] Y. Y. Tong, H. S. Kim, P. K. Babu, P. Waszczuk, A. Wieckowski, and E. Oldfield. An NMR investigation of CO tolerance in a Pt/Ru fuel cell catalyst. *J. Am. Chem. Soc.*, 124(3):468–473, 2002.

[79] S. Malhotra and R. Datta. Membrane-supported nonvolatile acidic electrolytes allow higher temperature operation of proton-exchange membrane fuel cells. *J. Electrochem. Soc.*, 144(2):L23–L26, 1997.

[80] T. A. Zawodzinski, C. Karuppaiah, F. Uribe, and S. Gottesfeld. *Aspects of CO tolerance in polymer electrolyte fuel cells: Some experimental findings*, volume 97 of *Electrochemical Society Series*, pages 139–146. 1997.

[81] J. D. Kim, Y. I. Park, K. Kobayashi, M. Nagai, and M. Kunimatsu. Characterization of CO tolerance of PEMFC by ac impedance spectroscopy. *Solid State Ionics*, 140(3-4):313–325, 2001.

[82] C. Yang, P. Costamagna, S. Srinivasan, J. Benziger, and A. B. Bocarsly. Approaches and technical challenges to high temperature operation of proton exchange membrane fuel cells. *J. Power Sources*, 103(1):1–9, 2001.

[83] Y. C. Si, R. C. Jiang, J. C. Lin, H. R. Kunz, and J. M. Fenton. CO tolerance of carbon-supported platinum-ruthenium catalyst at elevated temperature and atmospheric pressure in a PEM fuel cell. *J. Electrochem. Soc.*, 151(11):A1820–A1824, 2004.

[84] R. C. Jiang, H. R. Kunz, and J. M. Fenton. Influence of temperature and relative humidity on performance and CO tolerance of PEM fuel cells with nafion (r)-teflon (r)-zr(hpo4)(2). *Electrochim. Acta*, 51(26):5596–5605, 2006.

[85] L. Y. Sung, B. J. Hwang, K. L. Hsueh, and F. H. Tsau. Effects of anode air bleeding on the performance of CO-poisoned proton-exchange membrane fuel cells. *J. Power Sources*, 195(6):1630–1639, 2010.

[86] F. Sapountzi, M. N. Tsampas, and C. G. Vayenas. Electrocatalysis and electrochemical promotion of CO oxidation in PEM fuel cells: the role of oxygen crossover. *Top. Catal.*, 44(3):461–468, 2007.

[87] H. P. Dhar, L. G. Christner, and A. K. Kush. Nature of CO adsorption during $H_2$ oxidation in relation to modeling for CO poisoning of a fuel-cell anode. *J. Electrochem. Soc.*, 134(12):3021–3026, 1987.

[88] Q. F. Li, R. H. He, J. O. Jensen, and N. J. Bjerrum. Approaches and recent development of polymer electrolyte membranes for fuel cells operating above 100 degrees C. *Chem. Mat.*, 15(26):4896–4915, 2003.

[89] J. S. Wainright, J. T. Wang, D. Weng, R. F. Savinell, and M. Litt. Acid-doped polybenzimidazoles - a new polymer electrolyte. *J. Electrochem. Soc.*, 142(7):L121–L123, 1995.

[90] R. Savinell, E. Yeager, D. Tryk, U. Landau, J. Wainright, D. Weng, K. Lux, M. Litt, and C. Rogers. A polymer electrolyte for operation at temperatures up to 200-degrees-C. *J. Electrochem. Soc.*, 141(4):L46–L48, 1994.

[91] Q. F. Li, R. H. He, J. A. Gao, J. O. Jensen, and N. J. Bjerrum. The CO poisoning effect in PEMFCs operational at temperatures up to 200 degrees C. *J. Electrochem. Soc.*, 150(12):A1599–A1605, 2003.

[92] C. L. Gardner and M. Ternan. Electrochemical separation of hydrogen from reformate using PEM fuel cell technology. *J. Power Sources*, 171(2):835–841, 2007.

[93] H. K. Lee, H. Y. Choi, K. H. Choi, J. H. Park, and T. H. Lee. Hydrogen separation using electrochemical method. *J. Power Sources*, 132(1-2):92–98, 2004.

[94] K. A. Perry, G. A. Eisman, and B. C. Benicewicz. Electrochemical hydrogen pumping using a high-temperature polybenzimidazole (PBI) membrane. *J. Power Sources*, 177(2):478–484, 2008.

[95] H. Matsumoto, Y. Iida, and H. Iwahara. Current efficiency of electrochemical hydrogen pumping using a high-temperature proton conductor $SrCe_{0.95}Yb_{0.05}O_{3-\alpha}$. *Solid State Ionics*, 127(3-4):345–349, 2000.

[96] H. Muroyama, T. Matsui, R. Kikuchi, and K. Eguchi. Electrochemical hydrogen production from carbon monoxide and steam with a cell employing $CsH_2PO_4/SiP_2O_7$ composite electrolyte. *J. Electrochem. Soc.*, 156(12):B1389–B1393, 2009.

[97] J. X. Zhang and R. Datta. Electrochemical preferential oxidation of CO in reformate. *J. Electrochem. Soc.*, 152(6):A1180–A1187, 2005.

[98] R. Hanke-Rauschenbach, C. Weinzierl, M. Krasnyk, L. Rihko-Struckmann, H. Lu, and K. Sundmacher. Operating behavior and scale-up of an ECPrOx unit for CO removal from reformate for PEM fuel cell application. *J. Electrochem. Soc.*, 156(10):B1267–B1275, 2009.

[99] R. Hanke-Rauschenbach, S. Kirsch, R. Kelling, C. Weinzierl, and K. Sundmacher. Oscillations and pattern formation in a PEM fuel cell with Pt/Ruanode exposed to $H_2$/CO mixtures. *J. Electrochem. Soc.*, 157(11):B1521–B1528, 2010.

[100] P. Heidebrecht, R. Hanke-Rauschenbach, A. Jorke, and K. Sundmacher. On the design of cascades of ECPrOx reactors for deep CO removal from reformate gas. *Chem. Eng. Sci.*, 67(1):34–43, 2012.

[101] Y. L. Ma, J. S. Wainright, M. H. Litt, and R. F. Savinell. Conductivity of PBI membranes for high-temperature polymer electrolyte fuel cells. *J. Electrochem. Soc.*, 151(1):A8–A16, 2004.

[102] Q. F. Li, J. O. Jensen, R. F. Savinell, and N. J. Bjerrum. High temperature proton exchange membranes based on polybenzimidazoles for fuel cells. *Prog. Polym. Sci.*, 34(5):449–477, 2009.

[103] J. Cho, J. Blackwell, S. N. Chvalun, M. Litt, and Y. Wang. Structure of a poly(2,5-benzimidazole)/phosphoric acid complex. *J. Polym. Sci. Pt. B-Polym. Phys.*, 42(13):2576–2585, 2004.

[104] J. A. Asensio, S. Borro, and P. Gomez-Romero. Polymer electrolyte fuel cells based on phosphoric acid-impregnated poly(2,5-benzimidazole) membranes. *J. Electrochem. Soc.*, 151(2):A304–A310, 2004.

[105] J. A. Asensio and P. Gomez-Romero. Recent developments on proton conducting poly(2,5-benzimidazole) (ABPBI) membranes for high temperature polymer electrolyte membrane fuel cells. *Fuel Cells*, 5(3):336–343, 2005.

[106] R. H. He, Q. F. Li, A. Bach, J. O. Jensen, and N. J. Bjerrum. Physicochemical properties of phosphoric acid doped polybenzimidazole membranes for fuel cells. *J Mem. Sci.*, 277(1-2):38–45, 2006.

[107] R. H. He, Q. F. Li, G. Xiao, and N. J. Bjerrum. Proton conductivity of phosphoric acid doped polybenzimidazole and its composites with inorganic proton conductors. *J. Mem. Sci.*, 226(1-2):169–184, 2003.

[108] Q. Li, R. He, J. O. Jensen, and N. J. Bjerrum. PBI-based polymer membranes for high temperature fuel cells - preparation, characterization and fuel cell demonstration. *Fuel Cells*, 4(3):147–159, 2004.

[109] J. Lobato, P. Canizares, M. A. Rodrigo, and J. J. Linares. PBI-based polymer electrolyte membranes fuel cells - temperature effects on cell performance and catalyst stability. *Electrochim. Acta*, 52(12):3910–3920, 2007.

[110] J. Lobato, P. Canizares, M. A. Rodrigo, J. J. Linares, and J. A. Aguilar. Improved polybenzimidazole films for $H_3PO_4$-doped pbi-based high temperature PEMFC. *J Mem. Sci.*, 306(1-2):47–55, 2007.

[111] Y. Oono, A. Sounai, and M. Hori. Influence of the phosphoric acid-doping level in a polybenzimidazole membrane on the cell performance of high-temperature proton exchange membrane fuel cells. *J. Power Sources*, 189(2):943–949, 2009.

[112] L. X. Xiao, H. F. Zhang, E. Scanlon, L. S. Ramanathan, E. W. Choe, D. Rogers, T. Apple, and B. C. Benicewicz. High-temperature polybenzimidazole fuel cell membranes via a sol-gel process. *Chem. Mat.*, 17(21):5328–5333, 2005.

[113] J. A. Asensio, S. Borros, and P. Gomez-Romero. Proton-conducting membranes based on poly(2,5-benzimidazole) (ABPBI) and phosphoric acid prepared by direct acid casting. *J. Membr. Sci.*, 241(1):89–93, 2004.

[114] R. Bouchet, S. Miller, M. Duclot, and J. L. Souquet. A thermodynamic approach to proton conductivity in acid-doped polybenzimidazole. *Solid State Ionics*, 145(1-4):69–78, 2001.

[115] R. Bouchet and E. Siebert. Proton conduction in acid doped polybenzimidazole. *Solid State Ionics*, 118(3-4):287–299, 1999.

[116] Q. F. Li, H. A. Hjuler, and N. J. Bjerrum. Phosphoric acid doped polybenzimidazole membranes: Physiochemical characterization and fuel cell applications. *J. Appl. Electrochem.*, 31(7):773–779, 2001.

[117] J. L. Zhang, Y. H. Tang, C. J. Song, and J. J. Zhang. Polybenzimidazole-membrane-based PEM fuel cell in the temperature range of 120-200 degrees C. *J. Power Sources*, 172(1):163–171, 2007.

[118] D. A. Stevens and J. R. Dahn. Thermal degradation of the support in carbon-supported platinum electrocatalysts for PEM fuel cells. *Carbon*, 43(1):179–188, 2005.

[119] J. A. Asensio, E. M. Sanchez, and P. Gomez-Romero. Proton-conducting membranes based on benzimidazole polymers for high-temperature pem fuel cells. a chemical quest. *Chem. Soc. Rev.*, 39(8):3210–3239, 2010.

[120] E. Wiberg, A.F. Holleman, and N. Wiberg. *Lehrbuch der anorganischen Chemie*. Walter de Gruyter: Berlin, NewYork, Berlin, 2007.

[121] K. Sundmacher. Fuel cell engineering: Toward the design of efficient electrochemical power plants. *Ind. Eng. Chem. Res.*, 49(21):10159–10182, 2010.

[122] P. Heidebrecht, B. Hartono, C. Hertel, and K. Sundmacher. Biomass-based fuel cell power plants: Evaluation of novel reactors and process designs. *Ind. Eng. Chem. Res.*, 49(21):10859–10875, 2010.

[123] A. D. Modestov, M. R. Tarasevich, V. Y. Filimonov, and E. S. Davydova. CO tolerance and CO oxidation at Pt and Pt-Ru anode catalysts in fuel cell with polybenzimidazole-$H_3PO_4$ membrane. *Electrochim. Acta*, 55(20):6073–6080, 2010.

[124] A. D. Modestov, M. R. Tarasevich, and A. Y. Leykin. CO electrooxidation study on Pt and Pt-Ru in $H_3PO_4$ using MEA with PBI-$H_3PO_4$ membrane. *J. Power Sources*, 196(6):2994–3002, 2011.

[125] C. Oettel, L. Rihko-Struckmann, and K. Sundmacher. Characterisation of the electrochemical water gas shift reactor (EWGSR) operated with hydrogen and carbon monoxide rich feed gas. *Int. J. Hydrog. Energy*, 37(16):11759–11771, 2012.

[126] P. Heidebrecht, C. Hertel, and K. Sundmacher. Conceptual analysis of a cyclic water gas shift reactor. *Int. J. Chem. React. Eng.*, 6, 2008.

[127] P. Heidebrecht and K. Sundmacher. Thermodynamic analysis of a cyclic water gas-shift reactor (CWGSR) for hydrogen production. *Chem. Eng. Sci.*, 64(23):5057–5065, 2009.

[128] M. Watanabe and S. Motoo. Electrocatalysis by ad-atoms. 3. Enhancement of oxidation of carbon-monoxide on platinum by ruthenium ad-atoms. *J. Electroanal. Chem.*, 60(3):275–283, 1975.

[129] T. E. Springer, T. Rockward, T. A. Zawodzinski, and S. Gottesfeld. Model for polymer electrolyte fuel cell operation on reformate feed - effects of CO, $H_2$ dilution, and high fuel utilization. *J. Electrochem. Soc.*, 148(1):A11–A23, 2001.

[130] L. G. S. Pereira, V. A. Paganin, and E. A. Ticianelli. Investigation of the CO tolerance mechanism at several Pt-based bimetallic anode electrocatalysts in a PEM fuel cell. *Electrochim. Acta*, 54(7):1992–1998, 2009.

[131] G. Marban and T. Vales-Solis. Towards the hydrogen economy? *Int. J. Hydrog. Energy*, 32(12):1625–1637, 2007.

[132] M. Ball and M. Wietschel. The future of hydrogen - opportunities and challenges. *Int. J. Hydrog. Energy*, 34(2):615–627, 2009.

[133] M. Krausa and W. Vielstich. Study of the electrocatalytic influence of Pt/Ru and Ru on the oxidation of residues of small organic molecules. *J. Electroanal. Chem.*, 379(1-2):307–314, 1994.

[134] N. M. Markovic and P. N. Ross. Surface science studies of model fuel cell electrocatalysts. *Surf. Sci. Rep.*, 45(4-6):121–229, 2002.

[135] J. X. Zhang and R. Datta. Online monitoring of anode outlet CO concentration in PEM fuel cells. *Electrochem. Solid State Lett.*, 6(1):A5–A8, 2003.

[136] K. Ogata. *Modern Control Engineering*. Prentice Hall, 3rd ed. edition, 1997.

[137] M. K. Daletou, J. K. Kallitsis, G. Voyiatzis, and S. G. Neophytides. The interaction of water vapors with $H_3PO_4$ imbibed electrolyte based on PBI/polysulfone copolymer blends. *J. Membr. Sci.*, 326(1):76–83, 2009.

[138] A. Guerrero-Ruiz, A. Sepulveda-Escribano, and I. Rodriguez-Ramos. Carbon monoxide hydrogenation over carbon supported cobalt or ruthenium catalysts. promoting effects of magnesium, vanadium and cerium oxides. *Appl. Catal. A-Gen*, 120(1):71–83, 1994.

[139] P. P. Lopes and E. A. Ticianelli. The CO tolerance pathways on the Pt-Ru electrocatalytic system. *J. Electroanal. Chem.*, 644(2):110–116, 2010.

[140] H. Miura and R. D. Gonzalez. Methanation studies over well-characterized silica-supported Pt-Ru bimetallic clusters. *J. Catal.*, 74(2):216–224, 1982.

[141] J. J. Baschuk and X. G. Li. Modelling CO poisoning and $O_2$ bleeding in a PEM fuel cell anode. *Int. J. Energy Res.*, 27(12):1095–1116, 2003.

[142] A. Pitois, J. C. Davies, A. Pilenga, A. Pfrang, and G. Tsotridis. Kinetic study of CO desorption from PtRu/C PEM fuel cell anodes: Temperature dependence and associated microstructural transformations. *J. Catal.*, 265(2):199–208, 2009.

[143] J. C. Davies and G. Tsotridis. Temperature-dependent kinetic study of CO desorption from Pt PEM fuel cell anodes. *J. Phys. Chem. C*, 112(9):3392–3397, 2008.

[144] C.H. Bartholomew and R.J. Farrauto. *Fundamentals of Industrial Catalytic Processes*. Wiley-Interscience, 2nd edition, 2005.

[145] K. Sundmacher, A. Kienle, H.J. Pesch, J.F. Berndt, and G. Huppmann. *Molten Carbonate Fuel Cells: Modeling, Analysis, Simulation, and Control*. Wiley-VCH, 2007.

[146] T. J. Kotas. *The Exergy Method of Thermal Plant Analysis*. Malabar, Florida, US, Krieger Publishing Company, 2nd edition, 1995.

[147] J. Szargut, D.R. Morris, and F.R. Steward. *Exergy analysis of thermal, chemical, and metallurgical processes*. Hemisphere, University of Michigan, 1988.

[148] J. Dewulf, H. Van Langenhove, B. Muys, S. Bruers, B. R. Bakshi, G. F. Grubb, D. M. Paulus, and E. Sciubba. Exergy: Its potential and limitations in environmental science and technology. *Environ. Sci. Technol.*, 42(7):2221–2232, 2008.

[149] NIST Chemistry Webbook, URL: http://webbook.nist.gov, National Institute of Standards and Technology, USA, 2012.

[150] R.W. Baker. *Membrane technology and applications*. Wiley VHC, 2004.

[151] I.D. Wilson, E.R. Adlard, M. Cooke, and C.F. Poole. *Encyclopedia of separation science*. Academic, 2000.

[152] A. Brunetti, G. Barbieri, and E. Drioli. A PEMFC and $H_2$ membrane purification integrated plant. *Chem. Eng. Process.*, 47(7):1081–1089, 2008.

[153] G. Barbieri, A. Brunetti, A. Caravella, and E. Drioli. Pd-based membrane reactors for one-stage process of water gas shift. *RSC Adv.*, 1(4):651–661, 2011.

[154] J. A. Ritter and A. D. Ebner. State-of-the-art adsorption and membrane separation processes for hydrogen production in the chemical and petrochemical industries. *Sep. Sci. Technol.*, 42(6):1123–1193, 2007.

[155] V. Hacker, R. Fankhauser, G. Faleschini, H. Fuchs, K. Friedrich, M. Muhr, and K. Kordesch. Hydrogen production by steam-iron process. *J. Power Sources*, 86(1-2):531–535, 2000.

[156] C. Hertel, P. Heidebrecht, and K. Sundmacher. Experimental quantification and modelling of reaction zones in a cyclic watergas shift reactor. *Int. J. Hydrog. Energy*, 37(3):2195–2203, 2012.

[157] D.R. Stull. Vapour pressure of pure substances organic compounds. *Ind. Eng. Chem.*, 39(-):517–540, 1947.